

Electronic Thesis and Dissertation Repository

7-20-2022 1:00 PM

Electrochemical Deposition of Calcium Phosphate-Based Coatings onto Porous Ti using Organic Phosphorus Sources

Clement Lee, *The University of Western Ontario*

Supervisor: Liu, Lijia, *The University of Western Ontario*

A thesis submitted in partial fulfillment of the requirements for the Master of Science degree in Chemistry

© Clement Lee 2022

Follow this and additional works at: <https://ir.lib.uwo.ca/etd>

 Part of the [Biomedical and Dental Materials Commons](#)

Recommended Citation

Lee, Clement, "Electrochemical Deposition of Calcium Phosphate-Based Coatings onto Porous Ti using Organic Phosphorus Sources" (2022). *Electronic Thesis and Dissertation Repository*. 8670.
<https://ir.lib.uwo.ca/etd/8670>

This Dissertation/Thesis is brought to you for free and open access by Scholarship@Western. It has been accepted for inclusion in Electronic Thesis and Dissertation Repository by an authorized administrator of Scholarship@Western. For more information, please contact wlsadmin@uwo.ca.

Abstract

The study and commercialization of calcium phosphate (Ca-P) coatings have occurred for several decades. However, this has typically involved the use of hydroxyapatite. This thesis presents the synthesis of different Ca-P-based coatings that have not been studied. Anodic oxidation was employed to create a porous Ti substrate, while pulsed electrochemical deposition was used to deposit the coating onto the Ti. The first coating synthesized was a calcium phosphoserine (Ca-pSer) complex, which contained two different morphologies: a flower-like structure at low deposition time and a unique cubic morphology at higher deposition times. Next, an amorphous calcium phosphate coating was synthesized and stabilized using ATP. A biocompatibility test revealed that the ACP coating had high cell proliferation. Lastly, differing concentrations of zinc were introduced to the Ca-pSer system. Microspheres were formed at 5 mol% Zn, whereas using 10 mol% Zn, it was suspected that Zn replaces Ca in the Ca-pSer complex.

Keywords

Calcium phosphate coating, calcium phosphoserine coating, amorphous calcium phosphate coating, Zn-doped calcium phosphoserine, electrochemical deposition

Summary for Lay Audience

Currently in modern biomaterial research, there is much interest surrounding the use of titanium (Ti) and Ti-based materials as metallic implants for orthopedic and dental applications. Ti has proven to be an excellent candidate to fulfill this role as it is non-toxic and contains desirable mechanical properties, allowing it to support the weight of the human body in a safe manner. Despite these properties, osseointegration has proven to be a challenge due to the metallic nature of Ti. Due to what's known as the foreign body response, the immune system may reject the implant, causing it to become encapsulated by unwanted fibrous tissue. To overcome this obstacle, the substrate surface must be modified. Specifically, by depositing a thin layer of calcium phosphate (Ca-P) onto the substrate surface, not only would the immune system recognize this foreign material, but it would also improve the chemical bonding between the implant and bone.

There is currently an increasing demand for metallic implants to support, replace and enhance pre-existing biological structures. However, the deposition of Ca-P (hydroxyapatite) onto implant surfaces has already been studied extensively and has even been commercialized for several decades. In this thesis, an electrochemical method was employed to synthesize different Ca-P coatings, using non-traditional chemical precursors. The aim of this project is to explore the use of various Ca-Ps in the form of a bioactive coating which may lead to improved biological advantages and unique biomedical applications.

Co-Authorship Statement

The work described in this thesis is contributed by the author, under the supervision of Dr. Lijia Liu.

All chapters in this thesis were written by the author and edited by Dr. Liu.

Dr. Todd Simpson and Tim Goldhawk at the Nanofabrication Facility, UWO assisted in the characterization and training in scanning electron microscopy (SEM) imaging and energy dispersive x-ray (EDX) analysis which were used in Chapters 3, 4 and 5. Aneta Borecki at the X-ray Facility, UWO aided in the X-ray Diffraction (XRD) measurements in Chapters 3, 4 and 5. Yasmeen Shamiya under the supervision of Dr. Arghya Paul performed the *in vitro* biocompatibility studies in Chapter 4. Dr. Lo-Yueh Chang, beamline scientist at the TLS (Taiwan Light Source) 16A1 measured the Ca and P K-edge XANES in Chapter 3. Dr. Mohsen Shakouri, beamline scientist at the Soft X-ray Microcharacterization Beamline (SXRMB, Canadian Light Source) measured the Ca and P K-edge XANES in Chapter 4.

Acknowledgements

First, I would like to express my gratitude to my supervisor, Dr. Lijia Liu. Her patience and teachings helped transition me from an inexperienced undergraduate student, into who I am today. I loved working in our research group, both as a graduate student under her guidance and as a mentor for our newer members. I have learned a lot in the past two years, and I look forward to continuing my following years of graduate studies with her.

Next, I would like to thank the many scientists who have helped characterize and/or train me in characterization techniques throughout my thesis: Dr. Lucia Zuin, Dr. Mohsen Shakouri and Dr. Roman Chernikov at the CLS, Dr. Tianpin Wu and Dr. George Sterbinsky at the APS, Dr. Lo-Yueh Chang at the NSRRC, Dr. Todd Simpson and Tim Goldhawk at the Nanofabrication Facility (UWO), Aneta Borecki at the X-ray Facility (UWO), Dr. Zhiqiang Wang for teaching me how to organize synchrotron experiments and Yasmeen Shamiya for the cell culture testing.

I am also really grateful to my labmates: Xincheng (Leon) Li, Wai Tung (Ellie) Shiu, Yihong (Melody) Liu, Sylvia Li and Siena Idoine. You made the group environment really fun and made my master's experience much more enjoyable. Ellie and Melody: I look forward to continuing my graduate study and having even more fun (and stress) with you.

Lastly, I want to thank all my close friends for their support throughout my graduate studies: Anson, Ellie, Melody, Kirsty, Jeff, Haley, Kyle, MacLean, Khalid and Ryan. Special thanks to my mothers, Mansha and Zahra for always being there for me and always believing in me; none of this would be possible without you. Finally, I want to express my appreciation to my girlfriend, Grace for your continuous love and support.

Table of Contents

Abstract	ii
Summary for Lay Audience	iii
Co-Authorship Statement	iv
Acknowledgements.....	v
Table of Contents.....	vi
List of Tables	ix
List of Figures.....	x
List of Abbreviations.....	xiii
Chapter 1	1
1 Introduction.....	1
1.1 Titanium Usage in Modern Orthopedic Implants	1
1.2 Advantages and Challenges of Calcium Phosphate Coating Synthesis	1
1.3 Coating Formation via Electrochemical Deposition	4
1.4 Synchrotron Radiation.....	8
1.5 X-ray Absorption Spectroscopy.....	12
1.6 Project Objective and Thesis Outline	15
1.7 References.....	16
Chapter 2	19
2 Experimental.....	19
2.1 Anodic Oxidation to Fabricate a Porous Ti Surface.....	19
2.2 ECD to Deposit Ca-P Coating	20
2.3 Synchrotron Facilities.....	21
2.3.1 Canadian Light Source (CLS).....	21
2.3.2 National Synchrotron Radiation Research Center (NSRRC).....	22
2.4 Beamlines.....	22
2.4.1 Soft X-Ray Microcharacterization Beamline (SXRMB).....	22
2.4.2 TLS16A1	23
2.5 Other Characterization Methods	23
2.5.1 Scanning Electron Microscopy Imaging.....	23
2.5.2 Energy Dispersive X-Ray Analysis.....	26

2.5.3 Fourier Transform Infrared Spectroscopy.....	27
2.5.4 X-ray Diffraction	28
2.6 References.....	30
Chapter 3	32
3 Phosphoserine as an Organic Phosphorus Source for Calcium Phosphoserine Coating	32
3.1 Introduction.....	32
3.2 Experimental Methods.....	34
3.2.1 Materials.....	34
3.2.2. Ca-pSer Coating Electrolyte Synthesis	34
3.3 Results and Discussion	35
3.3.1 Visual Observation	35
3.3.2 Morphology Characterization by SEM.....	36
3.3.3 Elemental Analysis	39
3.3.4 X-Ray Diffraction.....	41
3.3.5 FT-IR Spectroscopy.....	43
3.3.6 XANES	45
3.4 Conclusion	48
3.5 References.....	49
Chapter 4	50
4 Adenosine Triphosphate as a Phosphorus Source for ACP Coating Synthesis	50
4.1 Introduction.....	50
4.2 Experimental Methods.....	52
4.2.1 Materials.....	52
4.2.2 ACP Electrolyte Synthesis	52
4.2.3 MTS Assay.....	52
4.3 Results and Discussion	54
4.3.1 SEM-EDX Analysis.....	54
4.3.2 FT-IR Spectroscopy.....	56
4.3.3 Ca and P K-Edge XANES.....	57
4.3.4 Stability Test.....	59
4.3.5 Biocompatibility Test	64
4.4 Conclusion	66
4.5 References.....	67
Chapter 5	69

5 Zinc-doped Calcium Phosphoserine Coating	69
5.1 Introduction.....	69
5.2 Experimental Methods.....	71
5.2.1 Materials.....	71
5.2.2 Zn-doped Ca-pSer Electrolyte Synthesis	71
5.3 Results and Discussion	72
5.3.1 SEM-EDX Analysis.....	72
5.3.2 X-ray Diffraction	75
5.3.3 FT-IR Spectroscopy	76
5.4 Conclusion	78
5.5 References.....	79
Chapter 6	81
6 Summary and Future Work	81
6.1 Summary.....	81
6.2 Future Work	83
6.3 References.....	85
Curriculum Vitae	86

List of Tables

Table 1-1: Characteristics and Molar Ratio of Bioactive Ca-P Phases.....	2
Table 1-2: Advantages and Limitations of Common Techniques used for Implant Coating Fabrication	5
Table 3-1: Synthesis parameters and the notations of the samples investigated in this study	35
Table 3-2: Elemental composition (atomic %) and Ca/P ratio of inorganic, pSer and submerged samples	40
Table 4-1: Synthesis parameters used in ATP study	52
Table 4-3: Synthesis parameters used in stability test.....	59
Table 5-1: Synthesis parameters and the notations of the samples investigated in this study	71
Table 5-2: Elemental composition (atomic %) of the pSer and Zn-doped pSer samples	74

List of Figures

Figure 1-1: Movement and Deposition of Ions during ECD	6
Figure 1-2: General Schematic of Synchrotron Facility. Major components include 1) Linear Accelerator (LINAC), 2) Booster Ring, 3) Storage Ring 4) Magnet, 5) Optics Hutch, 6) Experimental Hutch, 7) Endstation and 8) Radio Frequency Cavity	9
Figure 1-3 a) Spatial and b) spectral distribution of bending magnets, wigglers and undulators	10
Figure 1-4: Grating monochromator schematic	11
Figure 1-5: A) Double-crystal Monochromator Schematic and B) Bragg Angle Illustration	12
Figure 1-6: XANES and EXAFS Region of Ca K-Edge of HAp	13
Figure 2-1: Anodic Oxidation Setup	20
Figure 2-2: Pulsed ECD Parameters	21
Figure 2-3: Beamlines and their Correspondent Photon Energies at the CLS	22
Figure 2-4: Schematic of the SXRMB Beamline	23
Figure 2-5: SEM instrument schematic	24
Figure 2-6: Electron signals generated from incident electron beam	25
Figure 2-7: X-ray Emittance using External Energy Source	26
Figure 2-8: FTIR Spectrometer Schematic Diagram	28
Figure 2-9: Bragg Angle Illustration	29
Figure 3-1: Chemical structure of pSer	33
Figure 3-2: Photographs of Ti substrates at various treatment stage. (A) Anodized Ti substrate, (B) Anodized Ti substrate after electrochemically depositing inorganic Ca-P (Sample I-180), (C) Anodized Ti substrate after being submerged in inorganic Ca-P electrolyte for 24 hours (Sub-24h)	36
Figure 3-3: SEM imaging of Ti substrates at various treatment stage. (A) Anodized Ti substrate, (B) Anodized Ti substrate after electrochemically depositing inorganic Ca-P (Sample I-180) , (C) Anodized Ti substrate after being submerged in inorganic Ca-P electrolyte for 24 hours (Sub-24h)	37
Figure 3-4: SEM Imaging of Ca-P coatings formed using inorganic phosphorus precursor. (A) I-30, (B) I-60, (C) I-180	38
Figure 3-5: SEM Imaging of Ca-P coatings formed using pSer as phosphorus precursor. (A) pSer-30, (B) pSer-60, (C) pSer-180	39

Figure 3-6: XRD of I-60 in comparison with reference Ca-Ps and porous Ti substrate.....	41
Figure 3-7: XRD of pSer samples at different deposition times	42
Figure 3-8: FT-IR spectrum of I-60.....	43
Figure 3-9: FT-IR spectra of inorganic and Ca-pSer coatings	44
Figure 3-10: Ca K-Edge of inorganic samples to reference Ca-Ps.....	45
Figure 3-11: Ca K-Edge of pSer samples and ACP reference	46
Figure 3-12: P K-Edge of pSer samples and pSer reference	47
Figure 4-1: SEM imaging of ACP electrodeposited onto porous Ti. (a) 0 min (ATP-0), (b) 15 min (ATP-15), (c) 30 min (ATP-30), and (d) 1 hour (ATP-60) deposition time	54
Figure 4-2: EDX analysis of the distinct morphologies in ATP-30.....	55
Figure 4-3: FT-IR spectra of ATP-30, Reference ACP and Na ₂ ATP.....	56
Figure 4-4: Ca K-edge XANES of ACP coatings. (a) comparison of different deposition times, (b) comparison to reference Ca-Ps.....	57
Figure 4-5: The P K-edge XANES of ATP-30, reference ACP and Na ₂ ATP	58
Figure 4-6: SEM images of submerged samples (lower magnification). (a) ATP-30, (b) Water-1, (c) Water-3, (d) Water-7.....	60
Figure 4-7: SEM images of stability test samples. (a) ATP-30, (b) Water-1, (c) Water-3, (d) Water-7.....	61
Figure 4-8: XRD spectrum of submerged samples, ATP-30 and I-60.....	62
Figure 4-9: FT-IR spectra of submerged samples and ATP-30.....	63
Figure 4-10: Cell activity measured using MTS assay (MC3T3) for blank, I-60, ATP-0 and ATP-30 at different co-culture times	64
Figure 4-11: Calcein Images of substrates at 72-hour co-culture time. (a) Blank, (b) I-60, (c) ATP-0, (d) ATP-30	65
Figure 5-1: SEM imaging of coatings formed at 30-minute deposition time. Lower magnification: (a) pSer-30, (b) 5Zn-30 (c) 10Zn-30, higher magnification: (d) pSer-30, (e) 5Zn-30 (f) 10Zn-30.....	72
Figure 5-2: SEM imaging of coatings formed at 3 hours deposition time. (a) pSer-180, (b) 5Zn-180 (c) 10Zn-180	73
Figure 5-3: Elemental Composition of Coating Morphologies	74
Figure 5-4: XRD spectrum of pSer and Zn-doped pSer samples	76

Figure 5-5: FT-IR spectra of Zn-doped Ca-pSer samples77

List of Abbreviations

ACP	Amorphous Calcium Phosphate
ADP	Adenosine Diphosphate
AMP	Adenosine Monophosphate
ATP	Adenosine Triphosphate
APS	Advanced Photon Source
Ca-P(s)	Calcium Phosphate(s)
CLS	Canadian Light Source
DCPD	Dicalcium Phosphate Dihydrate
ECD	Electrochemical Deposition
EDX	Energy Dispersive X-ray
EXAFS	Extended X-ray Absorption Fine Structure
FT-IR	Fourier Transform – Infrared
HAp	Hydroxyapatite
NSRRC	National Synchrotron Radiation Research Center
NT(s)	Nanotube(s)
SEM	Scanning Electron Microscopy
SR	Synchrotron Radiation
SXRMB	Soft X-ray Microcharacterization Beamline
TLS	Taiwan Light Source
XANES	X-ray Absorption Near Edge Structure
XAS	X-ray Absorption Spectroscopy
XRD	X-ray Diffraction

Chapter 1

1 Introduction

1.1 Titanium Usage in Modern Orthopedic Implants

In modern biomaterial research, there is currently much attention surrounding the use of Ti and Ti-based alloys for orthopedic implant applications to support pre-existing biological structures. Due to their low toxicity and desirable mechanical properties, Ti metals serve as excellent candidates to fulfill this role, as they are classified as biologically inert materials. It is well known that aside from compatible bioactivity, materials used as bioimplants must also exhibit suitable mechanical strength to support the weight of the human body. Due to this reason, Ti and its alloys have great credibility as they have high tensile strength, high fatigue strength and a compatible modulus of elasticity to bone.¹ Despite its ideal mechanical properties, osseointegration has proven to be an obstacle due to the metallic nature of Ti. As a result of foreign body response, the Ti implant can become encapsulated by unwanted fibrous tissue, resulting in lengthened healing time.^{2,3} One suggested approach to promote the osteoconductivity of the metallic implant is to modify the substrate surface with a biocompatible coating. In particular, the deposition of a thin calcium phosphate (Ca-P) layer on the substrate will improve the osseointegration of the implant. The synthesized Ca-P coating would not only allow the body to recognize the foreign implant material but will also promote bone growth by improving the chemical bonding between the implant and bone.⁴

1.2 Advantages and Challenges of Calcium Phosphate Coating Synthesis

Ca-Ps are the major inorganic component of bone tissues which allows for superior osseointegration properties relative to Ti. They also have high biocompatibility, exhibiting similar chemical composition to natural bone. There are various phases of Ca-Ps that can be deposited onto the substrate surface depending on the types of reactants used, synthesis procedure and deposition conditions. Table 1-1 shows some common bioactive Ca-P phases and how they differ based on chemical structure, Ca/P ratio and stability in biological environments.⁵ Among these, hydroxyapatite (HAp) is often desired as it is thermodynamically more stable and is the main component of hard tissue.⁴ The similarity in crystallography and chemical composition to human bones provides the material with higher osseointegration potential, making it a great coating

candidate of choice for orthopedic metallic implants. However, there are some cases in which other Ca-P phases are more desirable. For example, instead of using traditional inorganic phosphorus salts which induce the formation of HAp, the use of adenosine triphosphate (ATP) disodium salt can result in the synthesis of amorphous calcium phosphate (ACP). With the use of phosphate-containing biomolecules, the morphology and function may vary, due to different Ca-P material being synthesized. Using this particular synthesis method, the Ca-P can act as a promising drug delivery carrier for the treatment of tumors and trauma.⁶ As a result, other Ca-Ps are also desired due to different advantages associated with each phase.⁷

Table 1-1: Characteristics and Molar Ratio of Bioactive Ca-P Phases

Compound name (chemical formula, abbreviation)	Ca/P Molar Ratio	pH range where it is most stable (solubility/g L⁻¹ at 25°C)	Characteristics
Dicalcium Phosphate dihydrate (CaHPO ₄ · 2H ₂ O, DCPD)	1.0	pH 2-6; (~0.088)	Higher solubility, higher supplement for Ca ²⁺ and PO ₄ ³⁻
Octacalcium Phosphate (Ca ₈ (HPO ₄) ₂ (PO ₄) ₄ · 5H ₂ O, OCP)	1.33	pH 5.5-7.0; (~0.0081)	Intermediate phase of HAp, most stable Ca-P in physiological pH
Amorphous Calcium Phosphate (Ca _x H _y (PO ₄) _z · nH ₂ O n = 3-4.5; 15-20% H ₂ O, ACP)	1.2-2.2	pH 5-12; (dependent on pH)	Transient phase of other Ca-Ps, releases Ca ²⁺ and PO ₄ ³⁻ in acidic environments
Hydroxyapatite (Ca ₁₀ (PO ₄) ₆ (OH) ₂ , HAp)	1.67	pH 9.5-12; (~0.00003)	Most thermodynamically stable, slow dissolution rates <i>in vivo</i>

In the 1920s, ideas based on Ca-P biomaterials were introduced for fracture treatment, following the logic that damaged hard tissue may be replaced and repaired by compounds with similar chemical resemblance.⁸ However, Ca-P ceramics are brittle and have low tensile strength (6-10 MPa), lacking the mechanical strength desired in a bioimplant.⁹ Decades later, biomedical research has suggested the use of Ca-P for thin coatings on metallic implants, in hopes of promoting osteoconductivity.^{10,11} The weakness in durability is significantly lessened after successful integration with the Ti implant, where Ca-Ps is deposited as a thin coating on the Ti implant surface. As a result, the mechanical strength and toughness of Ti is combined with the bioactive properties of Ca-P. This process allows for potential growth of bone-like material to form on the substrate surface, improving the osseointegration of the metallic implant. The long-term success rate of coated implants is dependent on various coating properties such as thickness, porosity, phases, crystallinity, and implant surface roughness.⁵ Implementation of ceramic Ca-P coatings onto a substrate surface would not only allow for prolonged service lifetime, but it would also suppress the toxic ions released when Ti alloys are used as the implant (e.g., Al³⁺ and V⁵⁺ are slowly released from Ti6Al-4V alloy under prolonged immersion in aqueous media).⁹

Synthetic Ca-Ps are commonly used in biomaterial research and application due to their excellent biocompatibility and similar chemical composition to natural bone.¹² Among the many bioactive Ca-P species, HAp has been studied and applied the most extensively due to its favourable surface chemistry and high thermodynamic stability in physiological environments. These desirable properties allow for synthetic HAp to be used in a wide spectrum of bioimplant applications including orthopedics and orthodontics.⁹ However, there has been a steady gain of interest in other Ca-P phases such as ACP due to various unique biological applications. In recent studies, it was reported that in the form of nanoparticles and composites, synthetic ACP can be used for enhanced bioactivity, promotion of bone-tendon healing and drug delivery through the use of different organic phosphorus precursors.¹³⁻¹⁵ Additionally, due to its inferior stability, the reactivity of ACP can be exploited to prepare coatings with enhanced adhesion. In previous studies, it was found that the inclusion of ACP can ensure improved adhesion between the coating and implant, which can also increase the longevity of the prosthesis.¹⁶ Overtime, ACP has proven to be an excellent candidate for implant coatings. Despite the advantages associated with ACP, there is an overall lack of usage involving ACP due to difficulties stabilizing the material.

In comparison to crystalline HAp, ACP has higher bioactivity with improved biodegradability and osteoblast adhesion.¹⁶ However, one major obstacle concerning the use of ACP is its instability and tendency to convert into various crystalline Ca-P phases (HAp, DCPD, etc.) causing challenges for storage and industrial use. In aqueous environments, its stability is governed by a variety of factors such as pH, ionic strength, and temperature.¹⁷ Without some method of stabilization, metastable ACP will readily convert into other undesired Ca-P species through the process of dissolution, nucleation, and crystal growth. It was previously hypothesized by Blumenthal *et al*, that the inclusion of ATP inhibits the crystallization from ACP to HAp, due to ACP poisoning heterogeneous nucleation sites and/or binding to HAp nuclei to prevent further crystal growth.¹⁸ As a result, the particular use of ATP for ACP synthesis has sparked interest as it can not only provide PO_4^{3-} through its hydrolysis, but residual ATP can also function as a stabilizer.

1.3 Coating Formation via Electrochemical Deposition

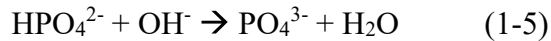
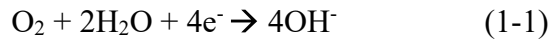
Ca-P coatings have been synthesized using other deposition technique such as plasma spraying^{19,20}, sputtering deposition²¹, sol-gel process²² and electrophoretic deposition²³ (Table 1-2). Among these techniques, electrochemical deposition (ECD) uses redox chemistry to modify the surface characteristics of a material. It can be favourable compared to other techniques due to its low cost, simplicity in performance and rapid deposition. In addition, ECD is not a “line-of-sight” technique, allowing for geometrically complex objects to be coated uniformly⁶. This advantage proves to be extremely useful because although the substrate used in this project were thin films, the structure of realistic bone material is highly irregularly shaped. Furthermore, the morphology, chemical composition and thickness of the Ca-P coating can be readily controlled by modifying the appropriate parameters within the deposition procedure^{24, 25}.

Table 1-2: Advantages and Limitations of Common Techniques used for Implant Coating Fabrication

Deposition Technique	Thickness	Advantages	Limitations
Plasma Spraying	< 20 μm	High deposition rate, low cost, improved corrosion resistance	Poor adhesion, lack of uniformity. ²⁶
Physical Vapour Deposition	0.5-3.0 μm	High adhesion, uniform thickness	Expensive, line-of-sight technique, slow rate of deposition. ²⁷
Sol-Gel	0.5-2.0 μm	Low temperature, uniform coating, excellent corrosion resistance	Precise control of reaction environment required; potential post-treatment required. ²⁸
Electrophoretic Deposition	0.1-2.0 mm	Uniform thickness, rapid deposition, low cost	Requires post-sintering, microstructures may contain cracks. ²⁹
Electrochemical Deposition	0.05-0.5 mm	Uniform coating, ability to deposit onto geometrically complex structures, rapid deposition	Poor adhesion, microstructure may contain cracks. ³⁰

Most experimental procedures for synthesizing Ca-P using ECD have involved the use of calcium nitrate tetrahydrate ((CaNO₃)₂·4H₂O) and ammonium dihydrogen phosphate (NH₄(H₂PO₄)) as the Ca²⁺ and PO₄³⁻ precursors respectively.²² Using these common inorganic reagents, a Ca/P ratio of 1.67 is typically obtained, allowing for the formation of stoichiometric HAp as the desired Ca-P phase. In this project, ECD was conducted using a two-electrode setup where the working electrode and the counter electrode are connected via an electrochemical workstation and dipped

into a solution composed of Ca^{2+} and PO_4^{3-} precursors. During ECD, a series of reactions occur on the cathode surface, which leads to Ca-P deposition:



The reduction of H_2O is shown in equation (1-2), where H_2 bubbles are formed in the vicinity of the cathode. The production of H_2 and OH^- in equations (1-2) and (1-3) resulted in a pH increase near the cathode, allowing for the acid-base reaction shown in equation (1-4). The spontaneous diffusion of OH^- ions from the surface of the cathode to the bulk electrolyte results in a pH change, allowing for the nucleation and growth of a Ca-P layer. As shown in Figure 1-1, during deposition, Ca^{2+} and H^+ migrate towards the cathode due to presence of an electric field gradient, while HPO_4^{2-} ions remain in the diffusing layer. Under normal circumstances, cations typically move toward the cathode, while anions move toward the anode. Throughout the deposition time, the concentration of HPO_4^{2-} in the bulk electrolyte increase, where the differential concentration can act as a driving force for HPO_4^{2-} to navigate towards the cathode.⁹

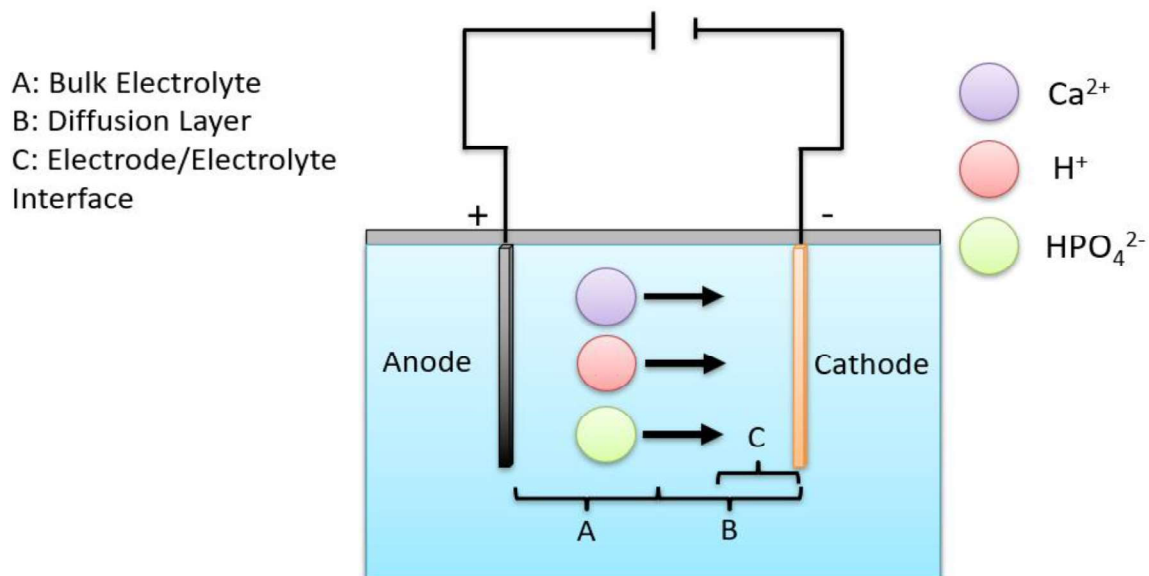
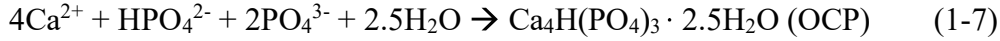
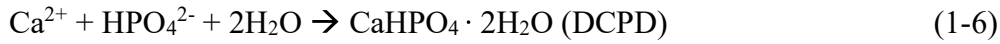


Figure 1-1: Movement of Ions during ECD

The production of OH⁻ ions on the cathode surface from equations (1-1) and (1-2) allows for higher HPO₄²⁻ and PO₄³⁻ production, which react with Ca²⁺ ions to form various Ca-P products:



DCPD, OCP and HAp (Table 1-1) are widely considered as the main bioactive Ca-P species commonly found in deposited thin films. Due to their different solubilities, the Ca-P phase synthesized is highly dependent on the pH of the synthesis environment. Past studies have often included small portions of H₂O₂ in the electrolyte to induce HAp formation, as it will supply additional OH⁻ through its reduction (Equation 1-9) and increase the local pH near the cathode surface.^{4,9}



Despite the advantages that ECD provides, there are some drawbacks with the utilization of this technique. In previous studies, it was found that deposition conducted using a constant current can lead to loose and low adhesive coatings. The reduction in water near the cathode surface can cause an excess of dihydrogen bubbles which may remain adsorbed on the cathode surface, preventing uniform deposition. The presence of these bubbles can not only promote the formation of porosities but could also produce undesired cracks within the coating.⁴ Furthermore, the ionic mobility of Ca²⁺ and phosphates can be negatively affected as well, which may cause a deviation in the expected Ca/P atomic ratio. The electrodeposition of calcium phosphate coatings is achieved through the precipitation of ions, where phosphate anions remain in the bulk electrolyte. At longer deposition times, the local concentrations within the electrolyte become modified, which can impact not only the stoichiometry, but potentially the desired phase of the Ca-P coating as well. One proposed solution is the use of pulsed ECD, where regular break times are implemented. By employing break times during deposition, there is a reduction in the accumulation of dihydrogen bubbles on the cathode surface, while also allowing for the restoration of the initial electrolyte concentrations within the cell.¹⁰ Finally, it is also hypothesized that the duration of the break times can also affect the nucleation and growth mechanisms of the deposited crystals, leading to

improved deposition conditions.³⁵ As a result of the limitations listed, this project will use pulsed ECD, instead of direct current ECD.

1.4 Synchrotron Radiation

Synchrotron radiation (SR) is a powerful electromagnetic radiation emitted tangentially to a curved orbit, generated from fast-travelling electrons approximating the speed of light. It covers a wide range of wavelengths from infrared to hard x-ray, with intensities much higher than radiation generated from conventional laboratory sources. On a much smaller scale, SR was first observed in a generic laboratory in 1947.³³ However, the potential of SR was unrealized until the late 1960s, when the first SR facility, Tantalus I, was built. This first-generation synchrotron light source paved the way for other SR facilities, as it introduced the inclusion of an electron storage ring, allowing for the preservation of high-energy radiation. These facilities soon evolved to second-generation light sources, which had a focal point of utilizing synchrotron x-rays to conduct experimental analysis. Years later, third-generation SR facilities have implemented the use of insertion devices to optimize the brightness of synchrotron light. In present day, there are currently over 80 synchrotrons operating worldwide which are used by researchers of different scientific disciplines. In this project, three third-generation SR facilities were used; the Canadian Light Source (CLS) in Saskatoon, the Advanced Photon Source (APS) in Illinois and the National Synchrotron Radiation Research Center (NSRRC) in Hsinchu.

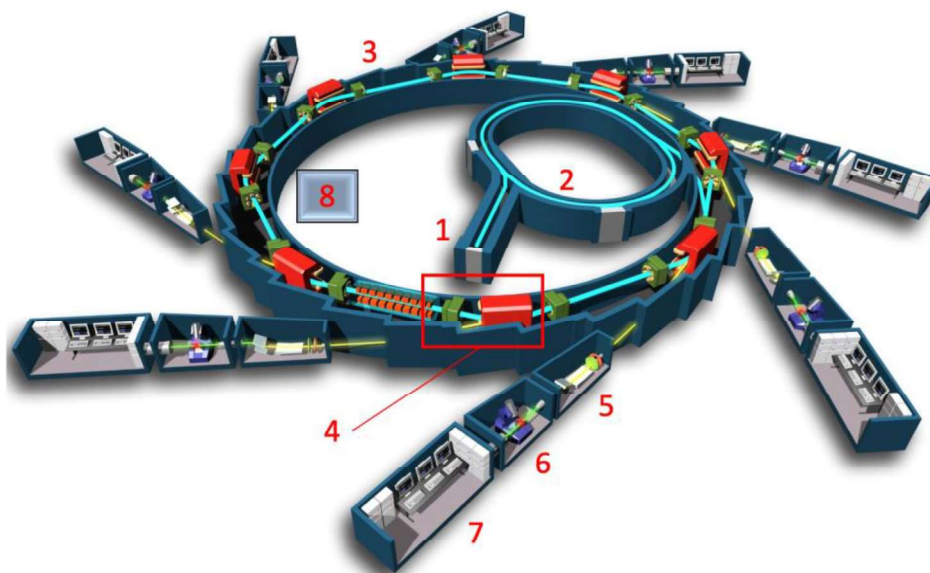


Figure 1-2: *General Schematic of Synchrotron Facility. Major components include 1) Linear Accelerator (LINAC), 2) Booster Ring, 3) Storage Ring 4) Magnet, 5) Optics Hutch, 6) Experimental Hutch, 7) Endstation and 8) Radio Frequency Cavity*

Figure 1-2 depicts the layout of a typical SR facility. Electrons are first generated by heating a cathode with high voltage. These emitted particles are sent into the linear accelerator (LINAC), where they get accelerated to an extremely high speed. Upon reaching sufficient speed, the electrons are ejected into the booster ring, where they are further accelerated to a speed approximating the speed of light. Due to the several magnets placed around the storage ring, the electron beam is guided circularly, where radiation emitted tangentially to the curved orbit can be used for synchrotron analysis at the beamline stations. To maintain the energy within the storage ring, the radio frequency cavity acts as an oscillating electromagnetic field which not only replenishes any energy loss but can also replenish the speed of the electrons.

As mentioned previously, third-generation SR facilities introduced the use of various insertion devices which enhance the brightness of the collimated beam. These devices include the wiggler and the undulator, which are specifically employed based on the beamline, desired angle of the beam and brilliance desired.³⁴ Functionally speaking, both apparatuses are similar as they are responsible for converting kinetic energy into radiation with the use of long, bending magnets with alternating polarity. Both types of multipolar magnets are placed in the straight, long sections of the storage ring, allowing for the emittance of higher volumes of radiation relative to the sole use

of bending magnets. The difference between the two devices lies in field strength. Wigglers provide stronger field strength, resulting in a wider opening angle ($1/\gamma$) and wiggling angle of the electron (α) compared to undulators.

$$\gamma = \frac{E}{m_0 c^2} \approx 1957 \text{ GeV} \tag{1-10}$$

Shown in Equation 1-10, γ is the ratio between the mass of a relativistic electron compared to its rest mass (m_0), E is energy and c is the speed of light. As mentioned, wigglers generate beams with wider openings ($\alpha > 1/\gamma$) while undulators produce narrower beams ($\alpha < 1/\gamma$). The difference in spatial distribution of radiation between the magnets is due to their distinct functionality. Typical bending magnets simply “bend” the electron beam, emitting wide and continuous spectrum of x-rays tangentially to the plane of the beam. This results in the production of synchrotron light less brilliant than the focused beam of x-rays introduced from using insertion devices.

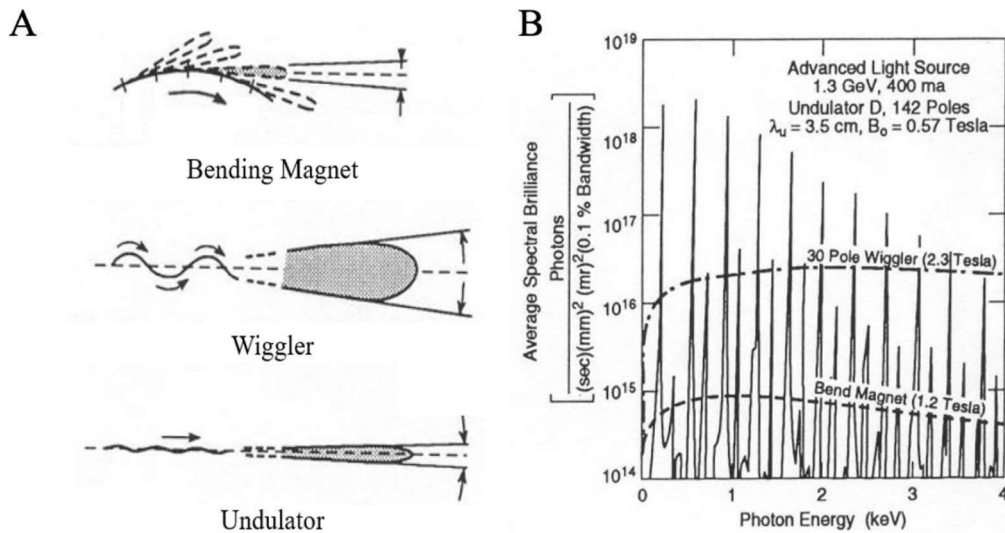


Figure 1-3 a) Spatial and b) spectral distribution of bending magnets, wigglers and undulators

Wigglers involve the use of less, but bigger bends which result in wider opening angles. Conversely, undulators utilize numerous smaller bends to create coherent beams of x-rays. Due to their wider angle, wigglers can output more radiation. However, due to the narrower beam produced by undulators, their brilliance and power per frequency could be higher. To date, third-

generation SR facilities have demonstrated that insertion devices allow for higher brightness, where the need for these devices is dependent on the energy of the storage ring and beamlines.³⁵

One of SR's greatest strengths is its tunability, as it can be employed from the IR to hard x-ray range.³⁶ However, the experimental apparatus must be set up accordingly to exploit this advantage. Due to SR's wide energy range, two different types of monochromators are used depending on whether soft or hard x-rays are being used. Soft x-ray (1-5 keV) beamlines typically use grating monochromators while double-crystal monochromators are employed at hard x-ray (5 – 40 keV) beamlines.

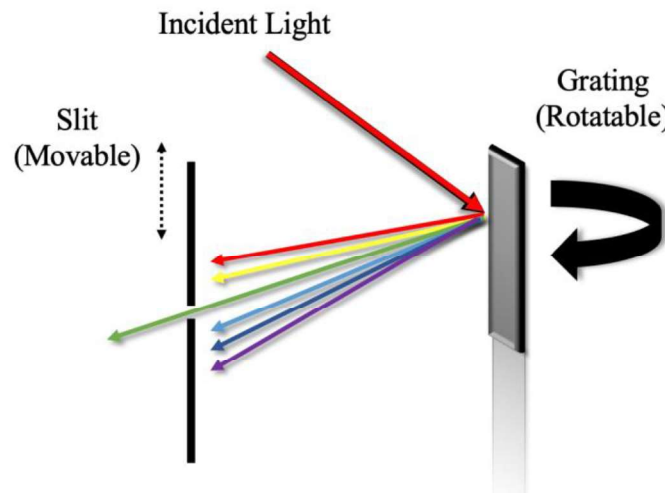


Figure 1-4: *Grating monochromator schematic*

In soft x-ray experiments, SR radiation hits the grating monochromator where a specific wavelength and colour can be chosen based on refraction. Within the experimental setup (Figure 1-4), the grating can be rotated, and the slit can be adjusted to select the wavelength desired. The interaction between the polychromator and grating monochromator can be expressed by Equation 1-11; where n is the order of diffraction, λ is the wavelength of refracted light, d is the distance between the grating lines, α is the angle of incidence and β is the angle of diffraction:

$$n\lambda = d(\sin\alpha + \sin\beta) \quad (1-11)$$

Hard x-ray beamlines make use of a double crystal monochromator setup which allows the selection and transmission of a specific x-ray energy onto the sample. This experimental setup is composed of two identical crystals parallel to each other which allows for the conversion of polychromatic SR to monochromatic light. The produced wavelength is expressed by Bragg's law (Equation 1-12).

$$n\lambda = 2d\sin\theta \quad (1-12)$$

where n is the order of diffraction, λ is the wavelength of the produced light, d is the lattice spacing of the crystal and θ is the Bragg angle. Figure 1-5 shows how the Bragg angle is determined. In this project, grating monochromators are used for soft x-ray beamlines while double-crystal monochromators were utilized for hard x-ray analysis.

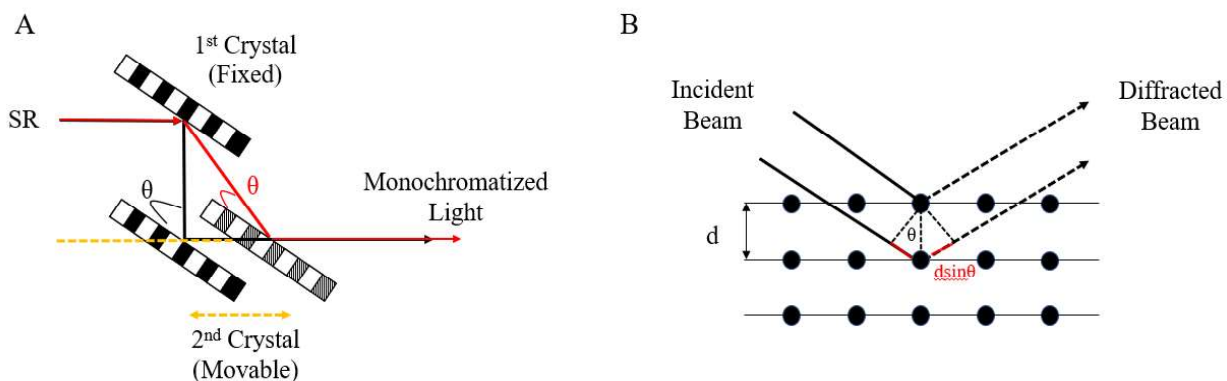


Figure 1-5: A) *Double-crystal Monochromator Schematic* and B) *Bragg Angle Illustration*

1.5 X-ray Absorption Spectroscopy

X-ray absorption spectroscopy (XAS) is a synchrotron-based technique which measures the absorption of x-rays near and above the core-level binding energies of a selected atom. As a result of distinct binding energies for each element, this technique allows for element-specific analysis, making it an essential probing technique for many disciplines of science. XAS is often separated into two energy regions: the X-ray Absorption Near-Edge Structure (XANES) and the Extended X-Ray Fine Structure (EXAFS), which can be used in combination to obtain detailed electronic structure, local geometric and structural information about a substrate.³⁷ The XANES region is composed of energies 20 eV below and 50 eV above the edge, whereas the EXAFS region ranges

from 50 eV to 1000 eV above the edge. This is illustrated in Figure 1-6, where the Ca K-Edge of HAp is shown.

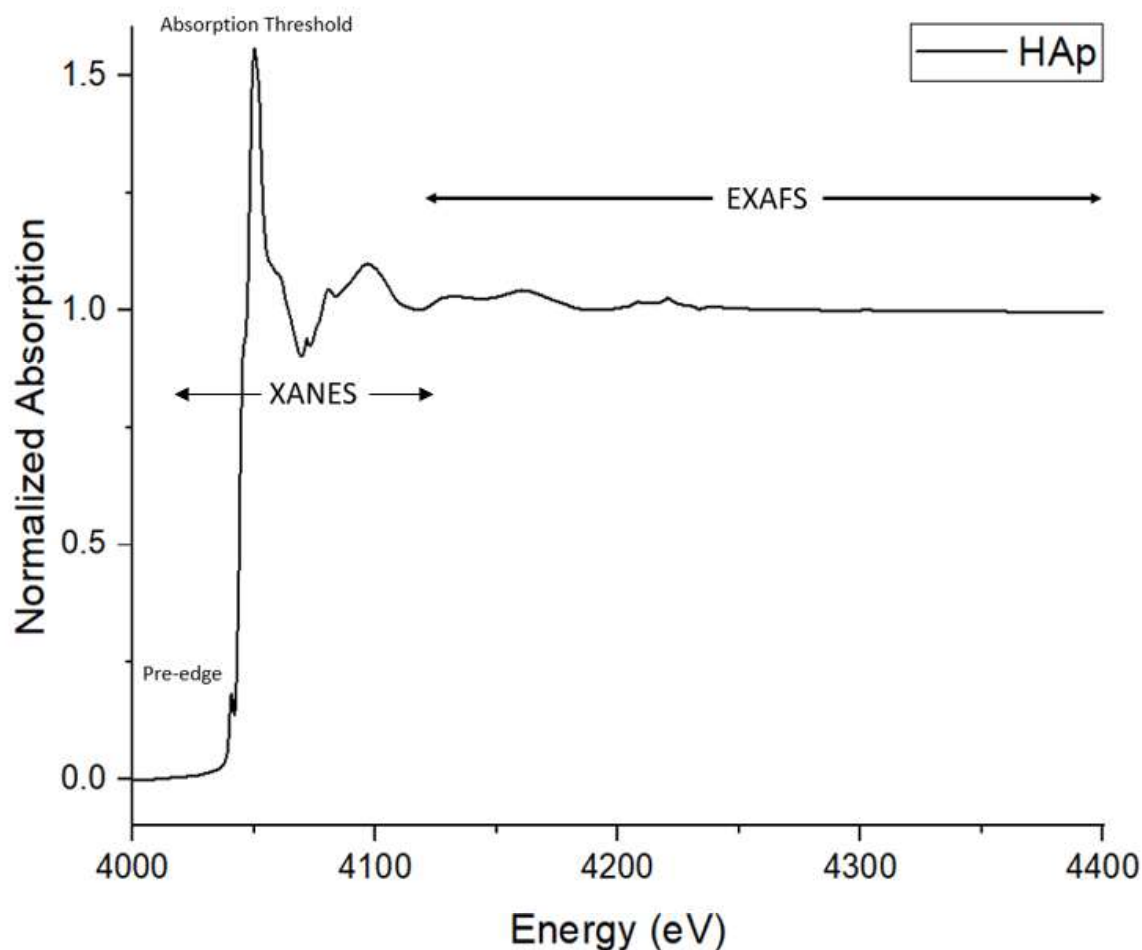


Figure 1-6: XANES and EXAFS Region of Ca K-Edge of HAp

The XANES region is attributed to electronic transitions into bound and quasi-bound states, followed by multiple scattering contributions from neighbouring atoms. Metal K-edge absorptions show the presence of a weak pre-edge which arise from a quadrupole-allowed dipole-forbidden transition ($1s \rightarrow 3d$). Next, the absorption threshold marks the energy required to initiate the core electron excitation, which is related to its binding energy. Oscillation beyond the absorption threshold is created by multiple scattering, and the profile is influenced by the geometry around the element being excited. Therefore, XANES provides electronic structure information such as oxidation state, symmetry, and local atomic arrangement around the element of interest. Past the XANES region, the EXAFS region provides quantitative information on the geometric structure

such as the type and number of surrounding elements, and their distance to the element probed. The EXAFS pattern is created mainly from single scattering of the outgoing electrons. In past studies, the use of XAS to study Ca-P nanoparticles and composites have been reported.^{13,38,39} However, there is a lack of synchrotron-related analysis for Ca-P coatings. In this thesis, the use of XAS is focused on K-edge XANES, where the 1s electron is excited into a previously occupied electronic state of p symmetry (dipole-allowed transition), and further into a continuum state.⁴⁰

1.6 Project Objective and Thesis Outline

There is currently an ever-increasing demand for orthopedic implants as the global population continues to age and increase. The investigation of suitable implant substrates and Ca-P coatings is crucial in furthering the understanding of orthopedic applications. The use of ECD to deposit Ca-P coatings onto Ti to create metal implants has been performed for several decades. However, this has traditionally involved the use of an inorganic phosphorus precursor to synthesize HAp coatings. In this thesis, different types of Ca-P-containing species are synthesized as coatings, with the hopes of improved biological advantages relative to standard HAp coatings. Several characterization methods are employed to analyze the coatings, including the use of SR techniques.

This thesis is separated into six main chapters. Chapter 1 provides a general introduction regarding substrate requirements for suitable metal implants, Ca-P coating using ECD, an overview of synchrotron radiation and the project objective. Chapter 2 discusses the experimental protocols used to fabricate the Ca-P coatings and the usage of several characterization methods employed in the experimental chapters. Chapter 3 involves the synthesis of a calcium phosphoserine complex coating, using phosphoserine as an organic phosphorus precursor. Chapter 4 presents the use of ATP as the starting material to produce an ACP coating with enhanced biological effects. Chapter 5 examines the inclusion of varying zinc concentrations into the Ca-pSer coating. Finally, Chapter 6 concludes the thesis and discusses the future work regarding this project.

1.7 References

- [1] Saini, M. *World J Clin Cases* **2015**, 3 (1), 52.
- [2] *Biological Responses to Metal Implants*. <https://www.fda.gov/media/131150/download> (accessed 2021-07-15)
- [3] Parithimarkalaignan, S.; Padmanabhan, T. V. *J Indian Prosthodont Soc* **2013**, 13 (1), 2–6.
- [4] Mokabber, T.; Lu, L. Q.; van Rijn, P.; Vakis, A. I.; Pei, Y. T. *Surf. Coat. Technol.* **2018**, 334, 526–535.
- [5] Su, Y.; Cockerill, I.; Zheng, Y.; Tang, L.; Qin, Y.-X.; Zhu, D. *Bioact. Mater.* **2019**, 4, 196–206.
- [6] Jiang, Y.-Y.; Wang, Z.-Q.; Chen, J.-T.; Li, J.; Zhu, Y.-J.; Liu, L.-J.; Guo, X.-X.; Hu, Y.-F.; He, S.-S.; Wu, J.; Chen, F.; Sham, T.-K. *Phys. Chem. Chem. Phys.* **2020**, 22 (23), 13108–13117.
- [7] Zhao, J.; Liu, Y.; Sun, W.; Yang, X. *J. Res. Dent. Sci.* **2012**, 7 (4), 316–323.
- [8] Albee, H.; Morrison, S.J. *Ann. Surg.* **1920**, (1) 32-39.
- [9] Safavi, M. S.; Walsh, F. C.; Surmeneva, M. A.; Surmenev, R. A.; Khalil-Allafi, J. *Coatings* **2021**, 11 (1), 110.
- [10] Eliaz, N.; Metoki, N. *Materials* **2017**, 10 (4), 334.
- [11] Ducheyne, P.; Hench, L. L.; Kagan, A.; Martens, M.; Bursens, A.; Mulier, J. C. *J. Biomed. Mater. Res.* **1980**, 14 (3), 225–237.
- [12] Habraken, W.; Habibovic, P.; Epple, M.; Bohner, M. *Mater. Today* **2016**, 19 (2), 69–87.
- [13] Zhou, H.; Jiang, Y.-Y.; Tan, S.; Liu, L.-J.; Yao, Q.-T.; Xia, Y.-J.; Fan, Y.-S.; Hu, J.-P.; Zhou, Z.-F.; Lu, B.-Q.; He, S.-S.; Chen, F. *Ceram. Int.* **2020**, 46 (13), 20914–20922.
- [14] Liao, H.; Yu, H.-P.; Song, W.; Zhang, G.; Lu, B.; Zhu, Y.-J.; Yu, W.; He, Y. *J Nanobiotechnol* **2021**, 19 (1), 270.
- [15] Jiang, Y.-Y.; Wang, Z.-Q.; Chen, J.-T.; Li, J.; Zhu, Y.-J.; Liu, L.-J.; Guo, X.-X.; Hu, Y.-F.; He, S.-S.; Wu, J.; Chen, F.; Sham, T.-K. *Phys. Chem. Chem. Phys.* **2020**, 22 (23), 13108–13117.
- [16] Combes, C.; Rey, C. *Acta Biomater.* **2010**, 6 (9), 3362–3378.
- [17] Termine, J. D.; Peckauskas, R. A.; Posner, A. S. *Arch. Biochem. Biophys.* **1970**, 140 (2), 318–325.
- [18] Qi, C.; Zhu, Y.-J.; Zhao, X.-Y.; Lu, B.-Q.; Tang, Q.-L.; Zhao, J.; Chen, F. *Chem. Eur. J.* **2013**, 19 (3), 981–987.
- [19] Hasan, M. F.; Wang, J.; Berndt, C. *Appl. Surf. Sci.* **2014**, 303, 155–162.

- [20] Brossa, F.; Cigada, A.; Chiesa, R.; Paracchini, L.; Consonni, C. *J Mater Sci: Mater Med* **1994**, *5* (12), 855-857.
- [21] Kim, H.-J.; Jeong, Y.-H.; Choe, H.-C.; Brantley, W. A. *Thin Solid Films* **2014**, *572*, 119–125
- [22] Balamurugan, A.; Balossier, G.; Kannan, S.; Rajeswari, S. *Mater. Lett.* **2006**, *60* (17-18), 2288-2293.
- [23] Sridhar, T. M.; Kamachi Mudali, U.; Subbaiyan, M. *Corros. Sci.* **2003**, *45* (2), 237–252.
- [24] Lin, D.-Y.; Wang, X.-X. *Surf. Coat. Technol.* **2010**, *204* (20), 3205–3213.
- [25] Schmidt, R.; Hoffmann, V.; Helth, A.; Gostin, P. F.; Calin, M.; Eckert, J.; Gebert, *Surf. Coat. Technol.* **2016**, *294*, 186-193.
- [26] Maleki-Ghaleh, H.; Khalil-Allafi, J. *Surf. Coat. Technol.* **2019**, *363*, 179-190.
- [27] Mohseni, E.; Zalnezhad, E.; Bushroa, A. R. *Int. J. Adhes. Adhes.* **2014**, *48*, 238–257.
- [28] Yang, Y.; Kim, K.; Ong, J. *Biomaterials* **2005**, *26* (3), 327–337.
- [29] Priyadarshini, B.; Rama, M.; Chetan; Vijayalakshmi, U. *J. Asian Ceram. Soc.* **2019**, *7* (4), 397–406.
- [30] Gong, D.; Grimes, C.A.; Varghese, O. K.; Hu, W.; Singh, R. S.; Chen, Z.; Dickey, E. C. *J. Mater. Res.* **2001**, *16* (12), 3331-3334.
- [31] Drevet, R.; Benhayoune, H. *Coatings* **2022**, *12* (4), 539.
- [32] Sierra-Herrera, D. K.; Sandoval-Amador, A.; Montañez-Supelano, N. D.; Peña-Ballesteros, D. Y. *J. Phys.: Conf. Ser.* **2017**, *935*, 012032.
- [33] Blewett, J. P. *J. Synchrotron. Rad.* **1998**, *5*, 135-139
- [34] Vinokurov, N. A.; Levichev, E. B. *Успехи физических наук* **2015**, *185* (9), 917–939.
- [35] Brown, G.; Halbach, K.; Harris, J.; Winick, H. *Nucl. Instrum. Methods Phys. Res.* **1983**, *208* (1–3), 65–77.
- [36] Chen, M.; Luo, J.; Li, F.-Y.; Liu, F.; Sheng, Z.-M.; Zhang, J. *Light Sci Appl* **2016**, *5* (1), e16015–e16015.
- [37] Kjaergaard, C. H.; Qayyum, M. F.; Wong, S. D.; Xu, F.; Hemsworth, G. R.; Walton, D. J.; Young, N. A.; Davies, G. J.; Walton, P. H.; Johansen, K. S.; Hodgson, K. O.; Hedman, B.; Solomon, E. I. *Proc. Natl. Acad. Sci.* **2014**, *111* (24), 8797–8802.
- [38] Andersson, K. O.; Tighe, M. K.; Guppy, C. N.; Milham, P. J.; McLaren, T. I.; Schefe, C. R.; Lombi, E. *Environ. Sci. Technol.* **2016**, *50* (8), 4229–4237.

[39] Oxmann, J. F. *Biogeosciences* **2014**, *11* (8), 2169–2183.

[40] Baker, M. L.; Mara, M. W.; Yan, J. J.; Hodgson, K. O.; Hedman, B.; Solomon, E. I. *Coord. Chem. Rev.* **2017**, *345*, 182–208.

Chapter 2

2 Experimental

In this chapter, the method for fabricating calcium phosphate (Ca-P) coated Ti substrates is explained. The process is separated into two sections: anodic oxidation as a pre-deposition technique to create a suitable implant replica and electrochemical deposition (ECD) to form the coating on the substrate surface. Next, the synchrotron radiation (SR) facilities and the specific beamlines used for in this project will be mentioned. The three SR facilities include the Canadian Light Source (CLS) in Saskatoon, the National Synchrotron Radiation Research Center (NSRRC) in Taiwan and the Advanced Photon Source (APS) in Illinois. Finally, other laboratory characterization methods used to determine the morphology, elemental composition, bonding, and crystallinity of the substrates will be discussed.

2.1 Anodic Oxidation to Fabricate a Porous Oxide Layer

Ti materials, in their natural state, can cause bodily harm as a result of their gradual release of metallic ions.¹ Despite the ideal mechanical properties associated with Ti, stress-shielding phenomena and lack of osseointegration result in practical limitations.² However, when Ti is exposed to air or water, it naturally forms a ceramic layer, TiO₂, which can be viewed as a passive condition of Ti. The presence of this thin layer inhibits the release of metallic ions, promoting biocompatibility of the implant substrate. By employing various surface oxidation treatments, the porous TiO₂ layer can be thickened, allowing for more biological advantages.¹ Through the creation of a porous material, the Young's modulus of Ti can be reduced, minimizing the effects of stress-shielding.³ Furthermore, the surface of TiO₂ generates OH⁻, which improves the binding of Ca²⁺ and PO₄³⁻ ions, promoting osteoblast attachment and growth.⁴ Finally, the porosity can also aid in stimulating bone growth, where the permeability of the implant material allows for vascularization.² In this thesis, a porous Ti surface is fabricated using a multi-step anodic oxidation technique.

Prior to deposition, the Ti foil was anodized to promote the attachment between the coating and substrate. The porous Ti was synthesized by undergoing a two-step anodic oxidation process. The

Ti foil was first cut into small rectangles with dimensions 40 mm x 10 mm x 0.127 mm. Prior to anodization, the Ti films underwent ultrasonic cleaning with EtOH for 10 minutes using the Fisherbrand FB11201 Bath Sonicator. Next, an electrolyte containing 61.5 mL deionized water, 35.5 mL (CH₂OH)₂ and 0.229 g NH₄F was synthesized. The sample is anodized in an electrochemical cell setup at 50 V for 4 hours at room temperature, where a Pt foil (10 mm x 10 mm x 0.5 mm) acted as the cathode. This anodization was performed using the STP6005H DC Power Supply. After the first anodization, the substrate was ultrasonically cleaned using 1 M HCl to remove the surface of the oxide layer. Next, the substrate is rinsed using deionized water and EtOH, then air dried. Finally, the sample was anodized for a second time under the same experimental conditions for 1 hour, which furthers the growth of the oxide layer. After anodization, deionized water and EtOH were used to rinse the substrate once again, where the anodized Ti were stored at room temperature until deposition use. This electrochemical process was applied to every Ti foil, which served as the working electrode in the deposition experiment.

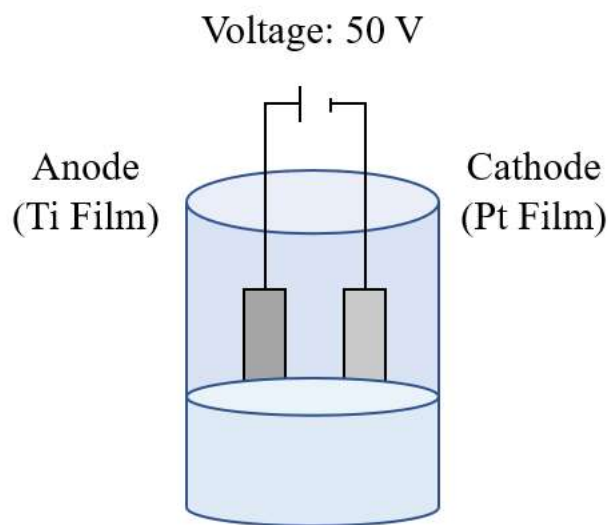


Figure 2-1: *Anodic Oxidation Setup*

2.2 ECD to Deposit Ca-P Coating

All coatings in this thesis were synthesized using pulsed ECD. During pulsed ECD, a two-electrode electrolytic cell setup was used to deposit the Ca-P-based coatings onto the porous oxide substrate. The electrochemical experiment was conducted using the Metrohm AutoLab electrochemical workstation, and Nova 2.1.4 software. The cathode in this experiment was a porous oxide substrate while the anode used was a Pt foil (10 mm x 10 mm x 0.5 mm). Multiple

deposition parameters were tested, using different pre-deposition treatments, pH, temperature and current. It was found that using pulsed ECD at a cycle of 0 mA/cm² (60 s) followed by -10 mA/cm² (60 s) yielded the best coating coverage, where the use of different parameters were compared by coating formation efficiency. For all coatings, the temperature of the electrolyte was maintained at 65±1 °C using an electric heater.

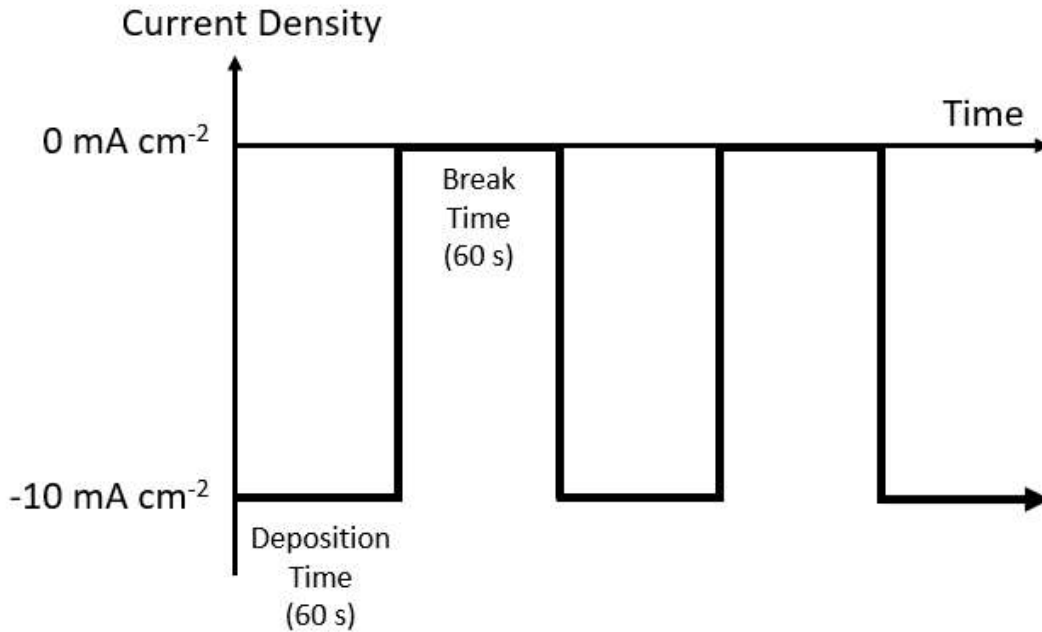


Figure 2-2: Pulsed ECD Parameters

2.3 Synchrotron Facilities

2.3.1 Canadian Light Source (CLS)

The CLS, a third-generation synchrotron light source located in Saskatoon, is one of the largest scientific projects ever produced in Canada. The synchrotron facility contains an electron beam of 2.9 MeV, and a 300 MeV linear accelerator used to accelerate electrons into the booster ring which consist of a circumference of 147 m. The CLS produces brilliant synchrotron radiation with continuous wavelengths from far infrared to hard X-ray, which has an intensity eight orders of magnitude higher than a laboratory source, allowing for a wide range of analyses (Figure 2-3). Currently, there are 16 (main) active beamlines with newer beamlines in development.⁵

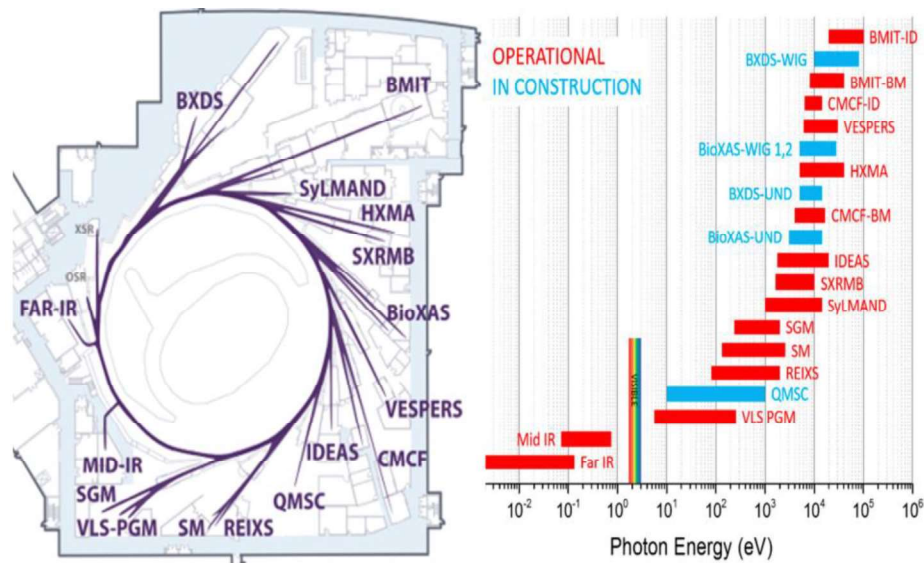


Figure 2-3: *Beamlines and their Correspondent Photon Energies at the CLS*

2.3.2 National Synchrotron Radiation Research Center (NSRRC)

The NSRRC is a non-profit institute funded by the Ministry of Science and Technology in Hsinchu, Taiwan. The NSRRC is the largest research facility in Taiwan and is composed of two accelerators: the Taiwan Light Source (TLS) and the Taiwan Photon Source (TPS). The TLS was first operated in 1993 and is the first third-generation synchrotron in Asia. This SR facility has a beam energy of 1.5 GeV, and a storage ring circumference of 120 m. Currently, there are 29 functioning beamlines at the TLS.⁶ The TPS is a newer SR facility, as it was first commissioned in 2016. This second accelerator is another third-generation synchrotron, with a beam energy of 3 GeV and a storage ring circumference of 518.4 m.⁷ There are currently over 50 active beamlines, with the construction of several more beamlines expected to be complete in 2023.⁸

2.4 Beamlines

2.4.1 Soft X-Ray Microcharacterization Beamline (SXRMB)

The beamline used at the CLS is the Soft X-Ray Microcharacterization Beamline (SXRMB), which is a medium energy X-ray beamline with an energy range of 1.7 – 10 keV. The SXRMB beamline does not make use of any insertion devices to enhance the brightness of the beam. Due to the bending magnets used, a larger beam size is used to analyze the substrates. At the SXRMB, X-ray is monochromatized using a double-crystal monochromator setup consisting of InSb (111)

or Si (111) crystals, where the choice of crystals allows for energy selection. SXRMB contain an energy range which allows the study of K-edge absorption of low Z elements and the L-edge of transition metals. Additionally, this beamline can also be used to perform high energy X-ray photoelectron spectroscopy and microprobe. In this project, the SXRMB beamline is used to obtain the Ca and P K-Edge XAS of the ACP-coated substrates.⁹

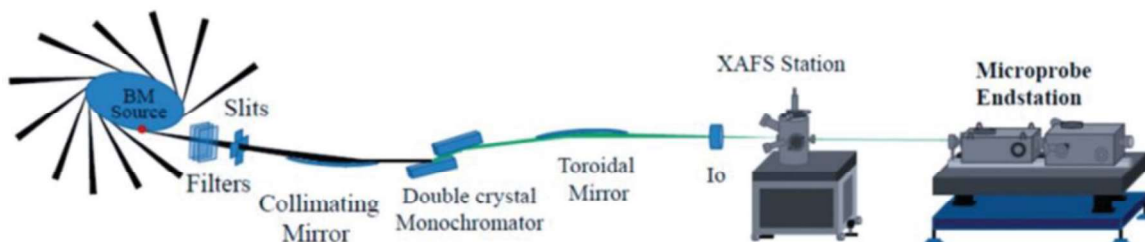


Figure 2-4: *Schematic of the SXRMB Beamline*

2.4.2 TLS16A1

This project also made use of the TLS16A1 beamline at the NSRRC for XANES measurements. The beamline consists of bending magnets, and a double-crystal monochromator to monochromatize medium X-rays with energies ranging from 1-8 keV. The 16A1 operate similar to the SXRMB, in terms of functionality, which also supports the study of the K-edges of elements Na to Co. Specifically, at this beamline, the Ca and P K-edge XAS of the samples in Chapter 3 were measured.

2.5 Other Characterization Methods

2.5.1 Scanning Electron Microscopy Imaging

Scanning electron microscopy (SEM) imaging is a conventional method of qualitatively analyzing the surface morphology of a sample. Compared to standard optical microscopes, SEM offers various advantages due to its use of electrons instead of visible light. The primary difference between the two observation methods is the disparity in resolution. Under normal conditions and given sufficient lighting, the human eye can distinguish points 0.2 mm apart from each other. With the assistance of an assembly of lenses from a microscope, the eye can distinguish two points even closer together due to magnification.¹⁰ Modern optical microscopes allow for magnification of up to 1500x, while electron microscopes exceed that limitation and permit the user to visualize

materials with up to 100,000x magnification.¹¹ As a result, SEM imaging can provide information regarding the topography and composition of a sample, with further enhanced detail.

Figure 2-5 shows a general schematic for SEM instrumentation. Electrons are first emitted from the electron gun, where they pass through the condenser and final (objective) lenses to form a focused electron beam. Upon bombardment of electrons onto the substrate, electron signals are generated as a result of the interaction between the beam and specimen. The substrate surface is then scanned linearly by the electron beam, where electron signals are collected by the detector. Finally, an electron image is generated pixel-by-pixel on a display, with the brightness of the corresponding points associated with the number of detected electrons.¹²

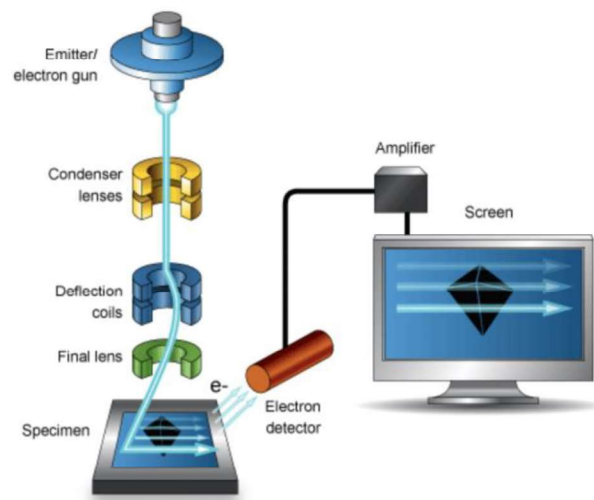


Figure 2-5: *SEM instrument schematic*

When the incident electron beam interacts with the sample, secondary electrons, backscattered electrons, Auger electrons, transmitted electrons and characteristic X-rays are produced. By measuring these particles emitted, various types of characterization can be conducted, such as Auger electron spectroscopy, energy dispersive x-ray (EDX) analysis and transmission electron microscopy. The practicality of these characterization techniques is heavily dependent on the properties of the sample (e.g., transmitted electrons cannot go through thicker substrates). In the form of SEM, the particles of interest are the backscattered electrons and the secondary electrons. Backscattered electrons, as the name suggests, are electrons which are reflected after elastic interactions between the beam and specimen. They provide chemical composition information, because their signal intensity is related to the atomic number of the specimen. However, due to their lower resolution for morphology characterization, backscattered electron detectors are rarely

used. Secondary electrons originate from the atoms of the sample and are attributed to inelastic interactions between the beam and sample. Relative to backscattered electrons, secondary electrons provide topographic information with a higher resolution and improved signal-to-noise ratio. SEM imaging is generated by probing the sample with a focused beam of electrons which scans across the specimen in a pattern. The interaction of the beam electrons with the sample atoms produces signals which provide information on the surface topography. As a result, the detector within the instrumentation primarily detects secondary electrons, allowing for “secondary electron” imaging.^{13,14}

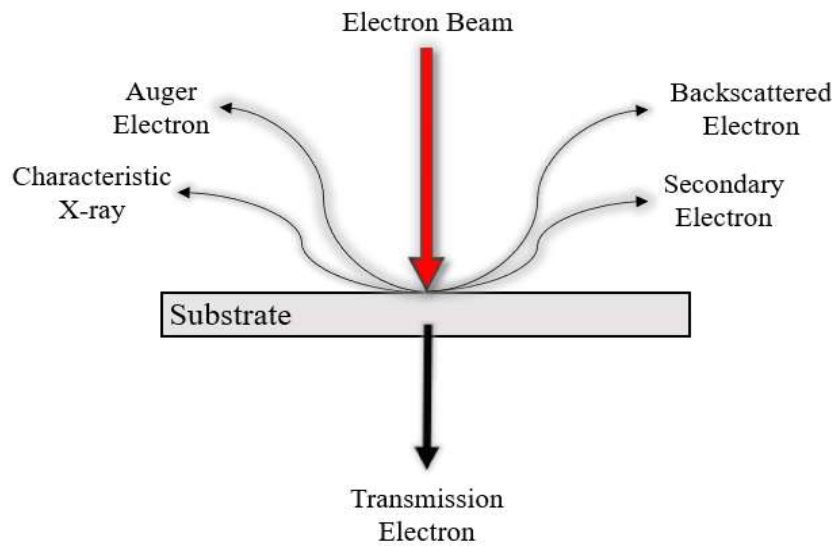


Figure 2-6: *Electron signals generated from incident electron beam*

Due to the thickness of the substrate used in this project, the characterization method used to monitor the morphology is SEM imaging. Specifically, SEM imaging is employed in every experimental chapter to 1) observe the advantages of using ECD as a deposition technique, 2) track the changes in coating coverage using different deposition durations and 3) to observe the composition and morphology of the deposited Ca-P coating. The SEM instrumentation used to image the morphology of the samples is the Zeiss Leo 1530, at Nanofabrication Facility, Western University (UWO).

2.5.2 Energy Dispersive X-Ray Analysis

EDX analysis is a technique commonly used in conjunction with SEM imaging. This characterization method involves the measurement of emitted x-rays generated by interactions between the sample and incident electron beam. Upon contact with the beam, a core electron within the inner shell of the atom is excited and ejected, causing the formation of an electron hole. When electrons from the outer shell fill up the vacancy within the inner shell, characteristic x-rays are emitted (Figure 2-7). The emitted x-ray photons have quantized energy and are related to the type of element and its specific electronic transition process. Consequently, by measuring the energy of the element-specific x-rays, elemental quantification can be conducted using an energy dispersive spectrometer.¹⁵

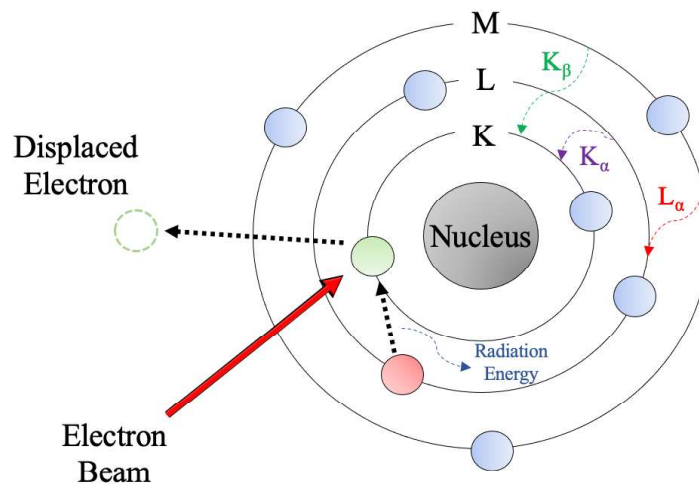


Figure 2-7: *X-ray Emittance using External Energy Source*

Electrons in the K, L and M shells correspond to the principal quantum numbers ($n = 1, 2, 3$ respectively). K electrons from the inner shell are ejected upon excitation from an electron beam, and an outer electron fills the hole, emitting distinct energy levels in the form of x-rays. To conveniently describe the radiative decay produced by electron transitions, the Siegbahn notation is used, where the first letter denotes the shell which contains the electron hole while α and β are used to show the size of the transition. The EDX instrumentation used to quantitatively measure the elemental composition of the samples was the Zeiss Leo 1540.

2.5.3 Fourier Transform Infrared Spectroscopy

Infrared (IR) spectroscopy is a common method of analysis often used to understand the chemical bonding of a sample by measuring the change in dipole moment during vibration. One of its greatest advantages is the lack of sample limitation when making use of this technique. Liquids, solids, gases and virtually all other physical states can efficiently utilize IR spectroscopy as a result of this technique functioning at the molecular level. IR spectroscopy theory makes use of the concept that each molecule interacts (e.g., absorption, emission, scattering, etc.) with electromagnetic radiation differently. Specifically, IR spectroscopy utilizes IR radiation to irradiate the sample, and then detects the frequencies which are absorbed by the molecule. The frequencies that are absorbed are correspondent to the frequency of the vibration of bonds in the molecule.¹⁶

IR spectroscopy takes advantage of the fact molecules absorb radiation at their resonant frequency (e.g., frequency where absorbed radiation matches the bond or functional group's vibration) to obtain detailed information regarding the molecular structure of an analyte. Upon absorption of IR radiation, transitions occur from the ground vibrational state to an excited vibrational state. This oscillation of the dipole interacts with the electric field of the radiation source and absorbs it. As a result, one of the limitations involving the use of IR characterization is the requirement of molecules without a null dipole moment. The factors corresponding to the dipole moment are dependent on variation of dipolar moment ($\delta\mu$) and variation of the normal coordinates (δq), and can be expressed as:

$$\frac{\delta u}{\delta q} \neq 0 \quad (2-1)$$

One of the most significant advances involving IR spectroscopy is the introduction of Fourier-Transform spectrometers, allowing for Fourier-transform IR (FTIR) spectroscopy. By combining the use of an interferometer and Fourier-transform theory, FTIR spectroscopy can not only improve the quality of data, but it can also reduce the time required to obtain a spectrum. Typical IR spectrometers are dispersive and include simple components such as an IR source, monochromator, splitter, and a detector. Within the experimental setup, the reference and sample beams with equivalent energies pass through the reference and sample respectively. The absorption

of IR radiation by the sample is then recorded, compared to the reference, and finally processed. With the introduction of an FTIR spectrometer, a Michelson interferometer is incorporated into the instrument. This component includes a fixed mirror, movable mirror and a beam splitter which is used to split, recombine, and redirect the beam of light into the detector, where the difference in intensity can be measured based on its wavelength.^{17,18} In this thesis, the Bruker Compact FT-IR Spectrometer: Alpha II was used to conduct FT-IR spectroscopy.

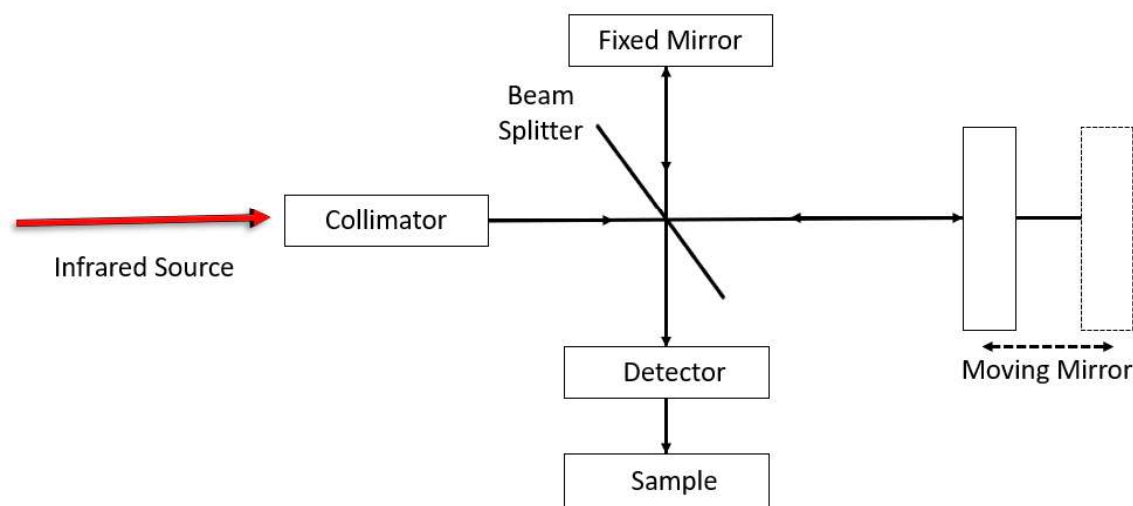


Figure 2-8: *FTIR Spectrometer Schematic Diagram*

2.5.4 X-ray Diffraction

X-ray diffraction (XRD) is a common technique used to determine the crystal structure of a material. When an x-ray interacts with an atom, elastic scattering occurs, where the electrons surrounding the atom absorb the energy, and re-emit the same energy in the form of an x-ray. The angle of x-ray diffraction is dependent on the incident angle, as well as the spacing between the atomic planes. Most x-rays are diffracted, regardless of the type of material. However, the practicality involving crystalline materials is much higher. In crystals, atoms are arranged in a pattern, which would result in a constructive interference of diffracted x-rays. In amorphous materials, such as amorphous calcium phosphate, the atoms are arranged randomly, and will provide less intense peaks, due to the destructive interference of x-rays. The relationship between the wavelength of incident x-rays, angle of incidence and spacing between the crystal lattice planes is expressed as Bragg's Law:

$$n\lambda = 2d\sin\theta \quad (2-2)$$

where n is an integer, λ is the wavelength of the X-ray, d is the distance between the crystal layers, and θ is the incident angle. Using this equation, the information provided in a XRD spectra can be quantified which can be matched with databases (e.g., International Centre for Diffraction Data: ICDD) to verify the identity of a material.¹⁹ In this thesis, XRD was conducted to measure the crystallinity of all coatings fabricated in this thesis. XRD was performed using an Inel XRG3000 generator and an Inel CPS 120 detector, at the X-ray facility, UWO.

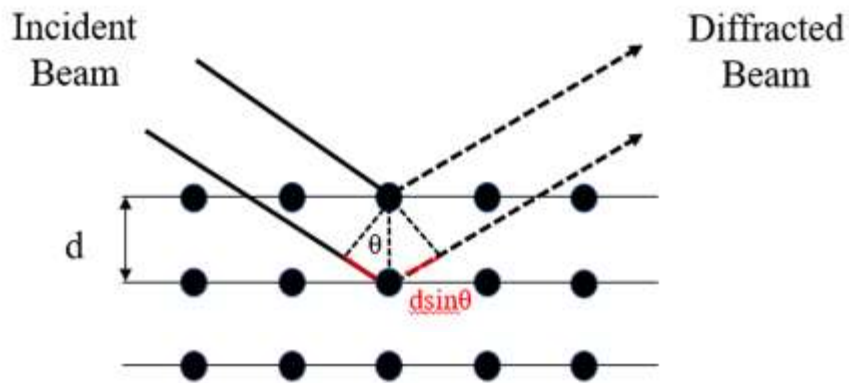


Figure 2-9: *Bragg Angle Illustration*

2.6 References

- [1] Wang, G.; Li, J.; Lv, K.; Zhang, W.; Ding, X.; Yang, G.; Liu, X.; Jiang, X. *Sci Rep* **2016**, *6* (1), 31769.
- [2] Domínguez-Trujillo, C.; Ternero, F.; Rodríguez-Ortiz, J. A.; Heise, S.; Boccaccini, A. R.; Lebrato, J.; Torres, Y. *Surf. Coat. Technol.* **2018**, *349*, 584–592.
- [3] Torres, Y.; Rodríguez, J. A.; Arias, S.; Echeverry, M.; Robledo, S.; Amigo, V.; Pavón, J. J. *J Mater Sci* **2012**, *47* (18), 6565–6576.
- [4] Tsou, H.-K.; Chi, M.-H.; Hung, Y.-W.; Chung, C.-J.; He, J.-L. *BioMed Res. Int.* **2015**, *2015*, 1–9.
- [5] Cutler, J.; Chapman, D.; Dallin, L.; Lamb, R. *QuBS* **2017**, *1* (1), 4.
- [6] Chang, S.-L.; Chen, C.-T. *Synchrotron Radiat.* **2013**, *26* (4), 32–38.
- [7] Liu, Y. C.; Chen, C. H.; Chen, J. Y.; Chiu, M. S.; Chou, P. J.; Huang, C. S.; Fann, S.; Kuo, C. C.; Lee, T. Y.; Liang, C. C.; Luo, G. H.; Tsai, H. J.; Tseng, F. H. *J. Phys.: Conf. Ser.* **2017**, *874*, 012020.
- [8] Hsu, K.-T.; Liu, Y.-C.; Kuo, C.-H.; Kuo, C.-C.; Wang, C.; Luo, G.-H.; Chou, P.-J.; Chen, C.-H.; Chiu, P.-C.; Cheng, Y.-S.; Huang, C.-H.; Chen, J.; Hu, K.-H.; Wu, C.-Y.; Liao, C.-Y.; Lee, D.; Chang, Y.-T. Current Status of the TPS and Its Future Prospects; Taipei, Taiwan, 2019; p 030003.
- [9] Xiao, Q.; MacLennan, A.; Hu, Y.; Hackett, M.; Leinweber, P.; Sham, T.-K. *J Synchrotron Radiat.* **2017**, *24* (1), 333–337.
- [10] Scanning Electron Microscopy. <https://www.nanoscience.com/techniques/scanning-electron-microscopy/> (accessed December 9th, 2021).
- [11] The Difference Between SEM and Optical Microscopes. <https://www.thermofisher.com/ca/en/home/materials-science/learning-center/applications/sem-optical-microscopes-difference.html> (accessed December 9th, 2021).
- [12] Zhu, F.-Y., Q.-Q. Wang, X.-S. Zhang, W. Hu, X. Zhao, and H.-X. Zhang, *Nanotechnology*, **2014**, *25*(18): p. 185705
- [13] *Scanning Electron Microscopy for the Life Sciences*, 1st ed.; Schatten, H., Ed.; Cambridge University Press, 2012.
- [14] Zhu, F.-Y.; Wang, Q.-Q.; Zhang, X.-S.; Hu, W.; Zhao, X.; Zhang, H.-X. *Nanotechnology* **2014**, *25* (18), 185705.

- [15] Groarke, R.; Vijayaraghavan, R. K.; Powell, D.; Rennie, A.; Brabazon, D. In *Fundamentals of Laser Powder Bed Fusion of Metals*; Elsevier, **2021**; pp 491–527.
- [16] Stuart, B. H. *Infrared Spectroscopy: Fundamentals and Applications: Stuart/Infrared Spectroscopy: Fundamentals and Applications*; **2004.**,Chapter 1 pp1-13
- [17] Giacomo, P. The Michelson Interferometer. *Mikrochimica Acta* 1988, III (19-31)
- [18] Stuart, B. H. *Infrared Spectroscopy: Fundamentals and Applications: Stuart/Infrared Spectroscopy: Fundamentals and Applications*; **2004.**,Chapter 2 pp15-44
- [19] Alqaheem, Y.; Alomair, A. A. *Membranes* **2020**, 10 (2), 33.

Chapter 3

3 Phosphoserine as an Organic Phosphorus Source for Calcium Phosphoserine Coating

3.1 Introduction

Calcium phosphate (Ca-P)-based biomaterials are prominent materials used in the biomedical field due to their high biocompatibility and osteoconductivity. This type of biomaterial is shown to exhibit bioactive properties within the human body, making it an excellent candidate for bone growth and remodeling applications.¹ Furthermore, due to its high compositional resemblance to bone material, synthesized Ca-P cements can be safely injected into the human body without undergoing foreign body response.² Despite the chemical similarities between the two, Ca-P materials are mechanically weaker than bone due to its brittle nature, prohibiting many load-bearing applications such as fracture fixation and dental implantation.³ Metals, on the other hand, have ideal mechanical properties such as high tensile strength, but lack the bioactivity desired. As a result, for implant applications, the production of Ca-P osteoconductive coatings on suitable implant surfaces has shown great potential as bone fillers and grafting materials for bone loss.⁴ Biomineralization is a strategy in which natural organic molecules and inorganic substances are used to promote bone regeneration. There is currently a strong desire for inorganic-organic hybrid biomaterials which can mimic not only the chemical composition but the physical properties of bone as well. Research performed in recent decades has shown that biomineralization to generate orderly structured inorganic-organic hybrid biomaterials is possible when combining inorganic molecules with the use of organic biomolecules such as adenosine triphosphate (ATP) and collagen.^{5,6} With this synthesis method in mind, researchers have been exploring and attempting to extend the list of organic phosphorus sources which can not only be used for Ca-P synthesis but can also exhibit superior bioactive properties.⁷

The discovery of phosphoserine (pSer) in biological fluids has drawn interest regarding its role in biomineralization.⁸ Studies in the past have shown that pSer contain biological significance, yet its interaction with Ca^{2+} and various Ca-Ps phases was not yet fully understood. Since then, Kesseli *et al.* discovered that a coordination network of calcium phosphoserine (Ca-pSer) forms when

Ca^{2+} reacts with pSer.¹ In a more recent study by Zhou, a Ca-pSer complex was successfully synthesized by biomineralization, with high biocompatibility and osteogenic potential.⁷

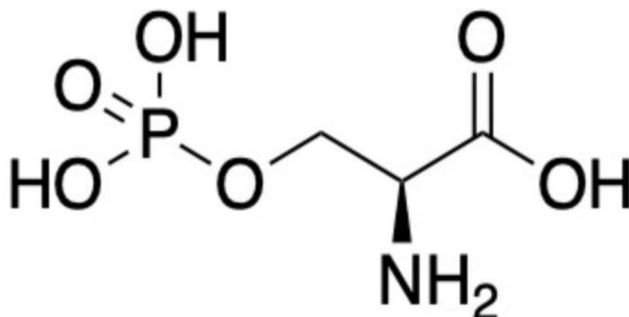


Figure 3-1: Chemical structure of pSer

However, Zhou had only studied Ca-pSer as inorganic-organic complex, while its synthesis, morphology, and biological potential as a coating for implant applications remain unrealized. In this chapter, pSer is used as an organic phosphorus precursor for the synthesis of a Ca-pSer coating on a porous Ti surface. Alongside the Ca-pSer coating, an inorganic Ca-P coating was synthesized using an inorganic phosphate salt which will act as a reference for comparison. Anodization of Ti is performed using multi-step anodic oxidation, while the deposition of the coatings is facilitated by pulsed electrochemical deposition (ECD). Various characterization methods are employed to study the growth of the coatings. Scanning electron microscopy (SEM) imaging is used to track the changes in morphology of the coating at different deposition times. Fourier transform – infrared (FT-IR) spectroscopy, x-ray diffraction (XRD) and x-ray absorption near edge structure (XANES) are used to identify the coatings formed, and to monitor any potential differences between the Ca-pSer complex and as a coating.

3.2 Experimental Methods

3.2.1 Materials

Calcium nitrate tetrahydrate ($\text{Ca}(\text{NO}_3)_2 \cdot 4\text{H}_2\text{O} > 99.0\%$), ammonium dihydrogen phosphate ($(\text{NH}_4)\text{H}_2\text{PO}_4 > 99.0\%$), calcium chloride ($\text{CaCl}_2 > 99.0\%$), commercially pure Ti film (cp-Ti $> 99.7\%$, 150 mm x 150 mm x 0.127 mm), hydrochloric acid (HCl, 37%) and phosphoserine (pSer) were purchased from Sigma Aldrich. Ammonium fluoride, ($\text{NH}_4\text{F} > 98.0\%$) was obtained from Alfa Aesar. Ethylene glycol ($(\text{CH}_2\text{OH})_2$) and ethanol (EtOH) were obtained from Fisher Chemical.

3.2.2. Ca-pSer Coating Electrolyte Synthesis

The deposition process was carried out using two different phosphorus precursors for two separate sets of samples, one inorganic and one organic. To form the inorganic Ca-P coating, a 100 mL electrolyte solution was created containing 0.042 M $\text{Ca}(\text{NO}_3)_2 \cdot 4\text{H}_2\text{O}$, 0.0025M $(\text{NH}_4)\text{H}_2\text{PO}_4$, and 3 mL H_2O_2 . Coatings were prepared with a deposition time of 30 minutes, 1 hour and 3 hours, respectively. Throughout the duration of the experiment, the pH of the bulk electrolyte was constant around 4.3 with a temperature of 65 °C under constant stirring. Some of the electrolyte was put aside for a submersion test, which is used to test the role of current within the ECD experiment.

The organic Ca-pSer coating was formed using the same pre-deposition and ECD configuration, To prepare the electrolyte, 5 mL of $(\text{CH}_2\text{OH})_2$ was added to a beaker containing 20 mL H_2O , 0.025M CaCl_2 and 0.0843 M pSer. Next, 1 M NaOH was added to adjust the pH of the solution to 5. This mixture was placed in a water bath at 55 °C for 10 minutes, where it could then be used for deposition. The samples synthesized and synthesis parameters used in this chapter are shown in Table 3-1.

Table 3-1: *Synthesis parameters and the notations of the samples investigated in this study*

Sample Treatment	Ca and P Precursors	Deposition Time	Sample Name
ECD using inorganic electrolyte	Ca(NO ₃) ₂ · 4H ₂ O and (NH ₄)H ₂ PO ₄	30 minutes	I-30
		1 hour	I-60
		3 hours	I-180
ECD using Ca-pSer electrolyte	CaCl ₂ and pSer	30 minutes	pSer-30
		1 hour	pSer-60
		3 hours	pSer-180
Submerged in Ca-P Electrolyte	Ca(NO ₃) ₂ · 4H ₂ O and (NH ₄)H ₂ PO ₄	24 hours	Sub-24h

3.3 Results and Discussion

3.3.1 Visual Observation

Figure 3-2 shows the appearance of anodized film before and after coating formation. Prior to ECD, the Ti foil underwent anodization with the aim of creating a porous oxide surface to facilitate deposition. From Figure 3-2A, the porous Ti has a tinted colour, different from the Ti foil prior to anodization. The top part of the foil was not submerged in the electrolyte and remains as metallic Ti. Figure 3-2B shows the formation of a white coating on the porous Ti, which is indicative of successful Ca-P synthesis. This coating was synthesized in an ECD experiment using the inorganic phosphorus precursor. As a comparative experiment, the porous Ti was submerged in the electrolyte without applying current, and its appearance is shown in Figure 3-2C. There are some clear differences between the two sets of samples, as the white coating for the ECD sample is much more uniform and provides greater coverage. The advantage of utilizing ECD is made much more apparent, as shown in SEM imaging later.

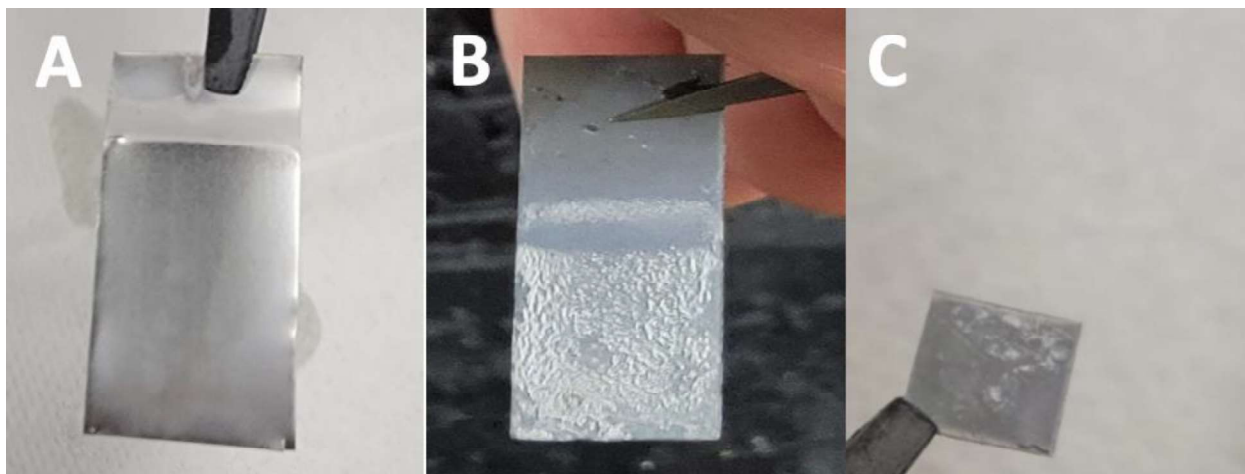


Figure 3-2: Photographs of Ti substrates at various treatment stage. (A) Anodized Ti substrate, (B) Anodized Ti substrate after electrochemically depositing inorganic Ca-P (Sample I-180), (C) Anodized Ti substrate after being submerged in inorganic Ca-P electrolyte for 24 hours (Sub-24h)

3.3.2 Morphology Characterization by SEM

Using SEM imaging, the surface morphologies of the coatings are observed. Firstly, a comparison is made between the electrochemically deposited samples, and the samples which were simply submerged in the Ca-P electrolyte. This comparison not only allows for the detection of the role of current in this experiment, but it also provides information on the efficiency of the set parameters chosen. The second comparison in this experiment involves the inorganic coating created using inorganic phosphate salt and the samples generated using the phosphorus precursor of interest, pSer. Typically, the use of inorganic phosphorus salt leads to the synthesis of crystalline HAp, while the expected phase for the product of interest is Ca-pSer, based on Zhou's study.⁷

In the past, researchers have opted to synthesize HAp as the Ca-P coating phase.⁹ Due to this reason, only the inorganic coatings will be shown in the comparison between ECD and simple submersion as a deposition method. This is a result of less familiarity associated with using Ca-pSer as a coating. Similar to the visual comparison observed earlier, SEM imaging shows similar results in terms of coating efficiency and coverage, as shown in Figure 3-3. Without applying the current, only scattered clusters were formed after immersing the porous Ti within the electrolyte for 24 hours. This suggests that the inclusion of current in ECD drives the reaction and promotes

the formation of Ca-P as a coating. Furthermore, in Figure 3-3B, the porous Ti surface cannot be observed, whereas in the Sub-24h sample, the surface is primarily made up of porous Ti. This shows that the usage of ECD provides greater coating coverage in comparison to the submerged coating, and such high surface coverage can be achieved within a much shorter duration.

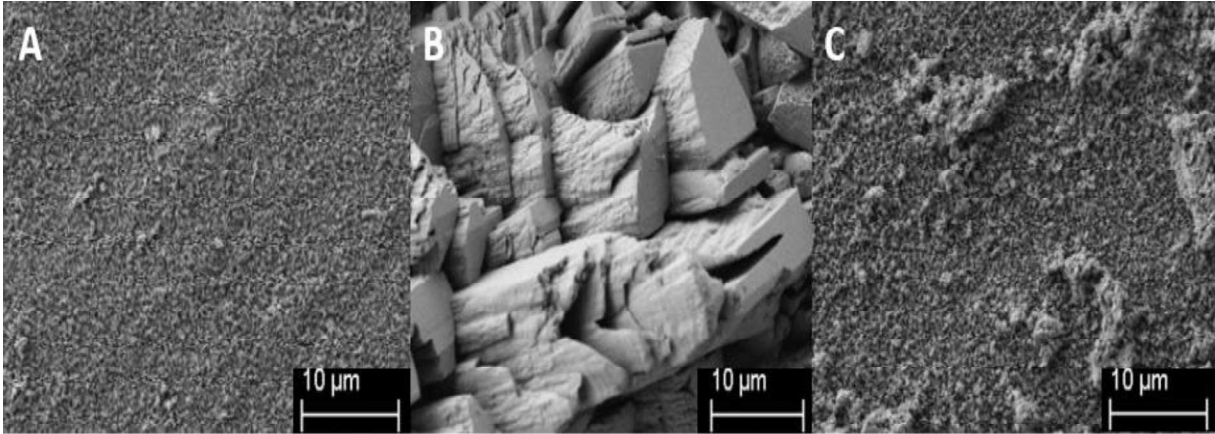


Figure 3-3: SEM imaging of Ti substrates at various treatment stages. (A) Anodized Ti substrate, (B) Anodized Ti substrate after electrochemically depositing inorganic Ca-P (Sample I-180), (C) Anodized Ti substrate after being submerged in inorganic Ca-P electrolyte for 24 hours (Sub-24h)

Next, the morphological evolution of the Ca-P coating was examined by SEM for samples prepared under different ECD duration. As shown in Figures 3-4A and 3-4B, most of the Ca-P deposited had a bud-like formation, with higher deposition time resulting in more buds. This is consistent with previous findings of electrochemically deposited HAp.¹⁰ For I-180, however, it contains the appearance of several bud-like shapes emerging from the plates. It is assumed that the denser plates are derived from excessive growth of the inorganic Ca-P coating.

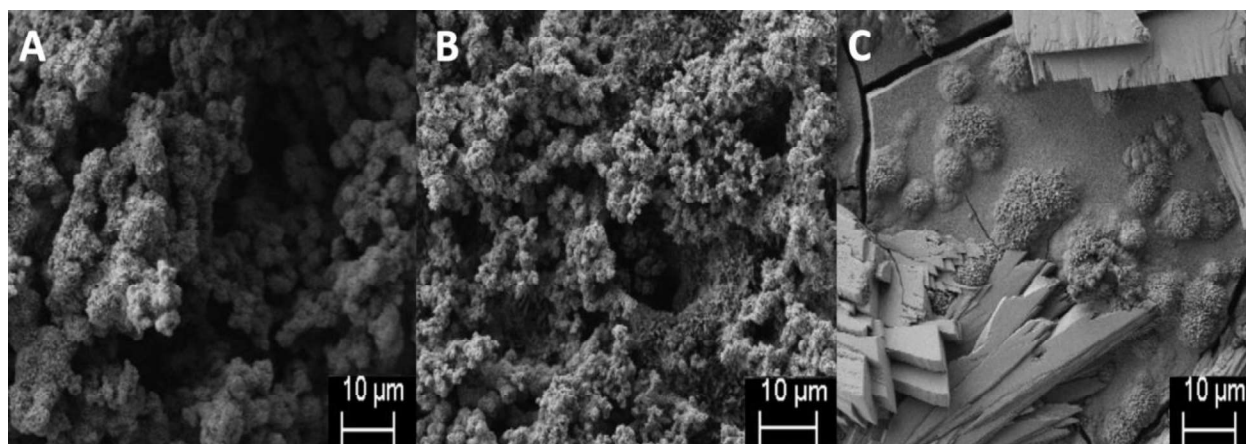


Figure 3-4: SEM Imaging of Ca-P coatings formed using inorganic phosphorus precursor. (A) I-30, (B) I-60, (C) I-180

In the previous study performed by Zhou, the synthesized Ca-pSer complex had formed in a flower-like morphology.⁷ Similar shapes were observed in the coatings prepared using shorter ECD duration (e.g., pSer-30), shown in Figure 3-5A. At longer ECD duration, however, there was also the formation of cubic shapes alongside the flower-like structures. A positive correlation between the deposition time and the amount of cubic structures can be observed. The cubic structure found at higher deposition times does not resemble the morphology in Zhou's study and does not correlate with any other past literature involving pSer synthesized Ca-Ps.^{1,7} In the previous study performed by Kesseli *et al*, Ca-pSer had been synthesized in a potentiometric titration experiment, where pSer was used as the titrant. They observed a similar morphology,¹ but their product lacks the quantity and distinct cuboid shape shown in Figure 3-5B and 3-5C. To conclude, the morphology of the synthesized pSer coating at higher deposition time is unique and requires further characterization methods for its determination.

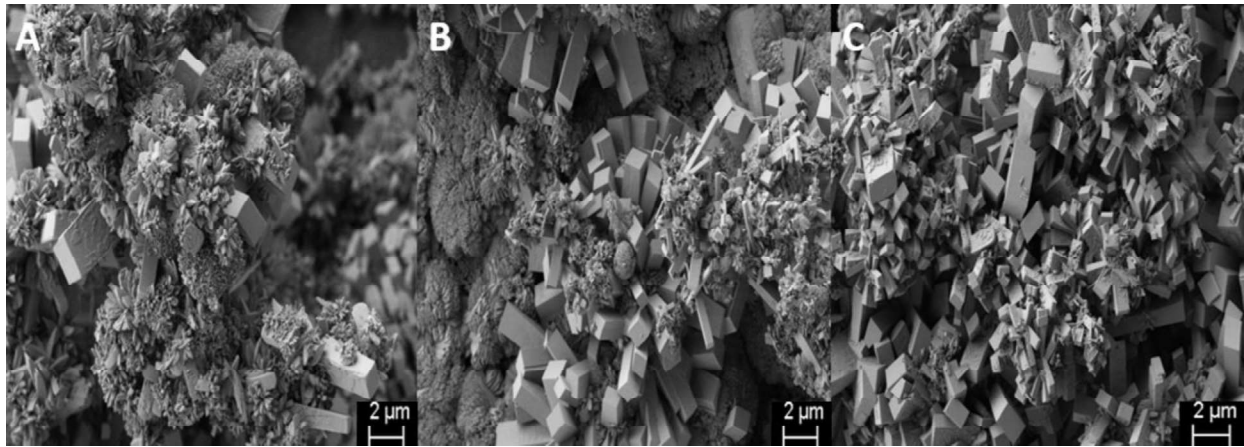


Figure 3-5: SEM Imaging of Ca-P coatings formed using pSer as phosphorus precursor. (A) pSer-30, (B) pSer-60, (C) pSer-180

3.3.3 Elemental Analysis

In conjunction with SEM imaging, EDX analysis was also conducted to determine the elemental composition of the synthesized coatings. Using this characterization technique, the elemental composition for both sets of samples can be measured and compared to literature. Specifically, by comparing the experimental Ca/P ratio to literature, the phase of the synthesized coatings can be deduced.⁹ For example, the Ca/P ratio for stoichiometric HAp is 1.67, which can become Ca-deficient apatite at Ca/P ratios 1.34 – 1.66.^{11,12} Another bioactive Ca-P of interest is dicalcium phosphate dihydrate (DCPD), which has a Ca/P ratio of 1.00.¹³

As shown in Table 3-2, Ca and P are detected on all the coatings, suggesting successful formation and deposition of a Ca-P species or Ca-pSer. When investigating the elemental composition of both coatings, it is apparent that the concentration of Ca and P are higher in all the inorganic Ca-P coatings. This could be the result of the inorganic coating having improved adhesion between the coatings and substrate. This observation could also be visually confirmed, as the white coating for the pSer samples begin to fall off the film given sufficient external movement.

Table 3-2: *Elemental composition (atomic %) and Ca/P ratio of inorganic, pSer and submerged samples*

	Ca (%)	P (%)	Ti (%)	Ca/P Ratio
I-30	12±3.1	10.5±1.4	0.3±0.8	1.10
I-180	12±4.8	10.7±1.9	1.0±0.9	1.13
pSer-30	5.5±2.1	5.5±1.5	4.1±0.4	0.99
pSer-180	5.6±2.1	6.1±1.9	0.1±0.1	0.92
Sub-24	0.3±0.3	0.3±0.3	20±10	1.07

Shown in Table 3-2, the Ca/P ratio of all the inorganic Ca-P coatings are lower than 1.67 (stoichiometry of HAp). It is worth noting that past studies have pointed out, due to the modification in local concentrations within the electrochemical cell, Ca-deficient apatite is commonly synthesized when using ideal direct current ECD parameters while using pulsed ECD.⁹ While the use of pulsed ECD can offset the limitation presented, the experimental protocol may require higher current density or H₂O₂ concentration than the current experimental procedure. Despite this, the experimental conditions were maintained for all other ECD experiments, because the coatings exhibited sufficient coverage, while the drawback present is exclusive to the inorganic coatings (e.g., insufficient OH⁻ production for HAp synthesis). As a result, for the remainder of Chapter 3, the inorganic coatings synthesized will be compared to not only HAp, but DCPD and Ca-deficient apatite as well. On the other hand, the calculated Ca/P ratio of pSer-30 is consistent with Ca-pSer (Ca/P Ratio = 1.0). However, the cubic shapes in pSer-180 have a Ca/P ratio of 0.92, which is slightly lower than the flower-like structures found in pSer-30. Furthermore, the atomic percent of Ti in pSer-30 is slightly higher than the other samples, indicating slow initial formation of the coating. However, at higher deposition time, the Ti% is decreased, suggesting the coating formed had thickened over time.

3.3.4 X-Ray Diffraction

XRD was used as a characterization method to determine the crystal structure of the coatings synthesized. The XRD pattern of I-60 is shown in Figure 3-6. For comparison, porous Ti and two reference Ca-P compounds are also included. Porous TiO_2 exhibits several sharp peaks which correspond to metallic Ti. The porous TiO_2 formed after anodization has an amorphous nature,¹⁴ so the XRD has no TiO_2 -related diffraction peaks. The feature from metallic Ti weakens significantly in I-60, and a few additional features occur at lower diffraction angles. Compared with the XRD of HAp and DCPD, the new features in I-60 resemble HAp but with poor crystallinity. This confirms the Ca-P coating prepared using inorganic phosphorus source has an apatite-like structure.

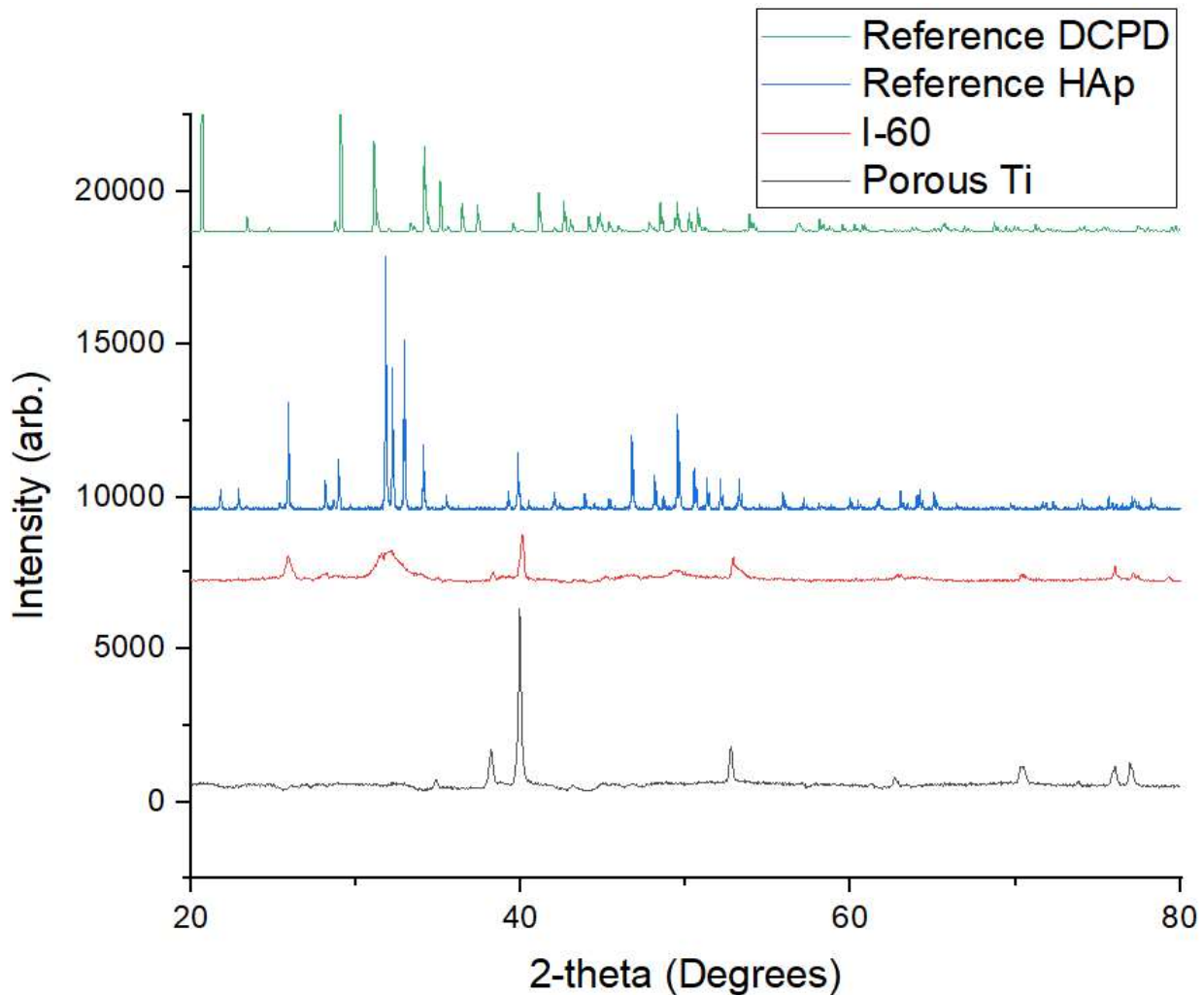


Figure 3-6: XRD of I-60 in comparison with reference Ca-Ps and porous Ti substrate

The XRD was also obtained for the pSer samples, as shown in Figure 3-7. At 30-minute deposition time, there are multiple characteristic peaks ranging from 15-40 degrees, which correspond to Ca-pSer complex reported in past literature.¹ However, at higher deposition times, all Ca-pSer-related peaks disappeared, leaving only peaks from the Ti substrate. This is quite surprising, since SEM confirms the coating presence as shown in Figures 3-5B and 3-5C. However, the lack of features within the XRD suggests that the cuboid structures found in the coating have an amorphous nature.

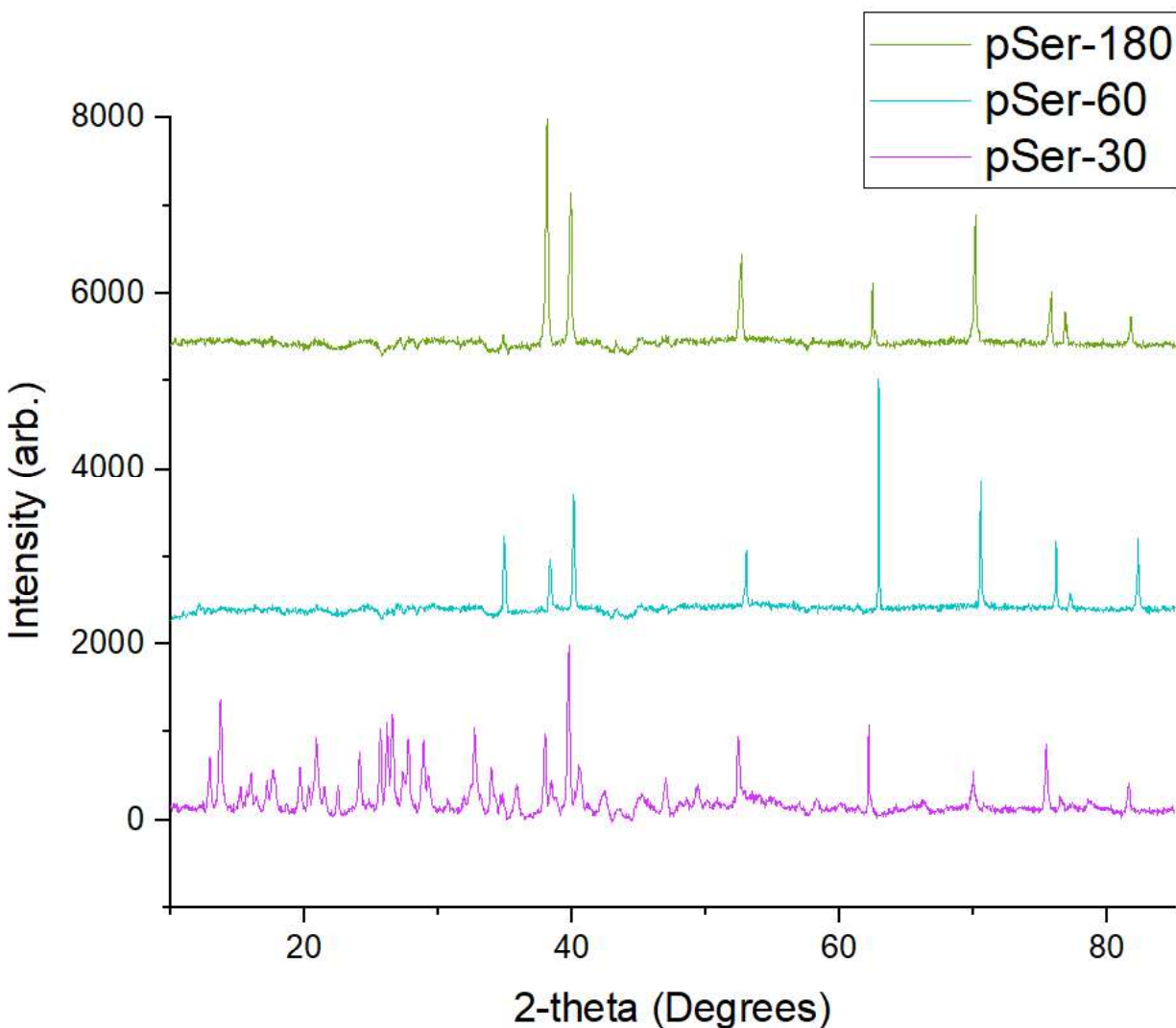


Figure 3-7: XRD of pSer samples at different deposition times

3.3.5 FT-IR Spectroscopy

FT-IR spectroscopy was used to detect any functional groups present within the coatings, which can also indicate the Ca-P phase of the products. Firstly, Figure 3-8 shows the FT-IR spectrum of I-60. The peaks at 3310 cm^{-1} and 644 cm^{-1} are attributed to the stretching and vibrational modes of -OH in HAp, although the peaks in I-60 are less noticeable. Next, the features indicating PO_4^{3-} at 562 cm^{-1} (ν_2), 602 cm^{-1} (ν_4), 962 cm^{-1} (ν_1), 1025 cm^{-1} (ν_3) closely resemble to HAp.¹⁵ It is worth noting that the FT-IR of Ca-deficient apatite is similar to that of HAp, and that the distinct peaks in the FT-IR spectrum of I-60 match both reference Ca-Ps.⁹

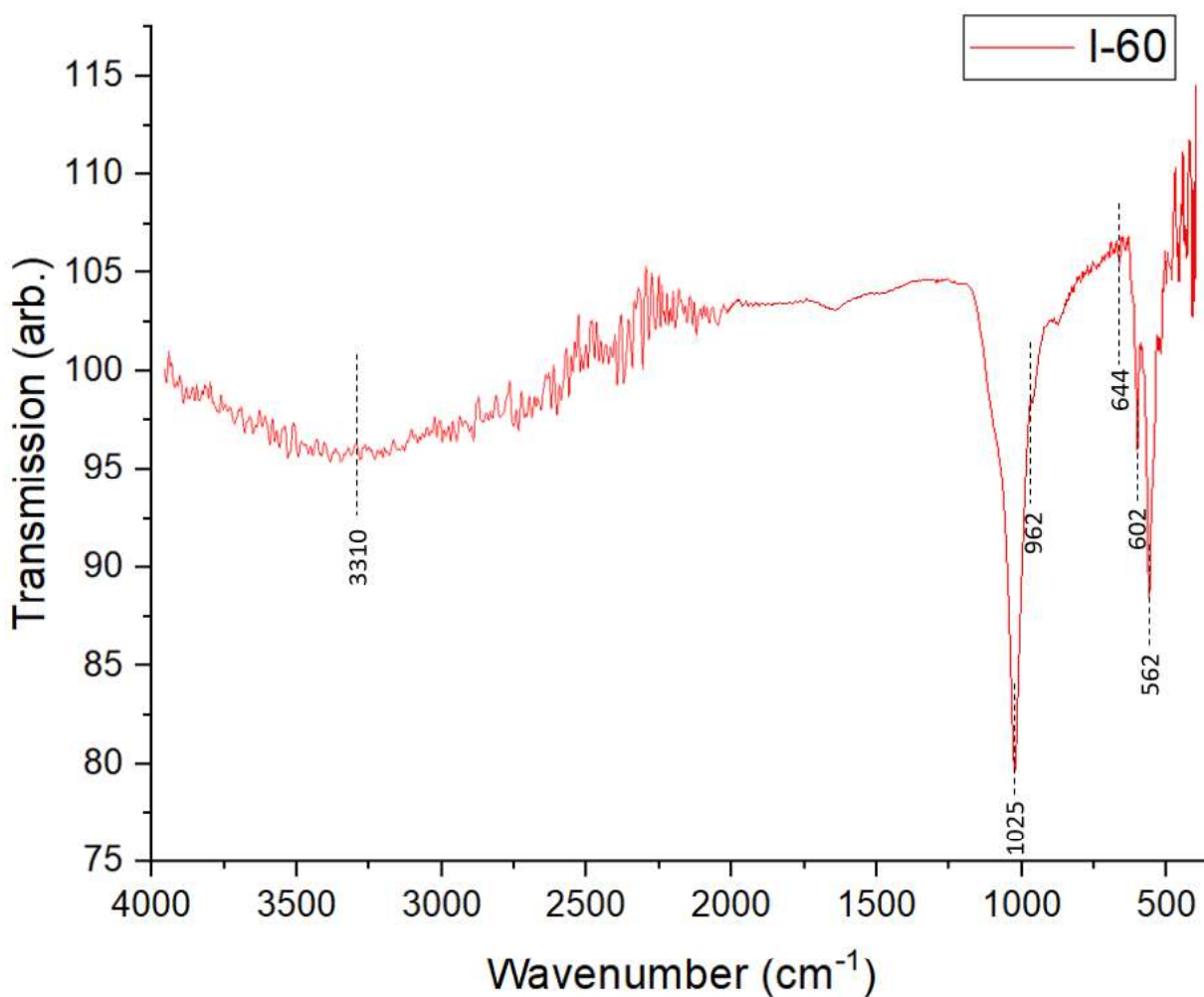


Figure 3-8: FT-IR spectrum of I-60

Next, the Ca-pSer samples are compared to the reference pSer to verify whether pSer used in the precursor has combined with Ca to form the Ca-pSer complex. Figure 3-9 shows the IR spectra of the Ca-pSer coatings, which correspond to Kesseli and Zhou's study.^{1,7} In comparison to their findings, the literature Ca-pSer and synthesized pSer coatings exhibited similar features: the carboxyl and amine peaks at 1650 cm^{-1} , as well as the several PO_4^{3-} -related vibration modes from 1200 cm^{-1} to 500 cm^{-1} . Next, the peak at 1258 cm^{-1} is ascribed to the stretching mode of P=O bond in pSer. The intensity of this feature is lessened in pSer-60 and pSer-180 due to attachment between Ca and PO_4^{3-} . Furthermore, when comparing the synthesized Ca-pSer coatings to the reference pSer, various features are notably different. The shift in peak intensity for the carboxyl and PO_4^{3-} peaks is due to the formation of the Ca-pSer complex, where Ca is bonded to the $-\text{COOH}$ and PO_4^{3-} respectively.

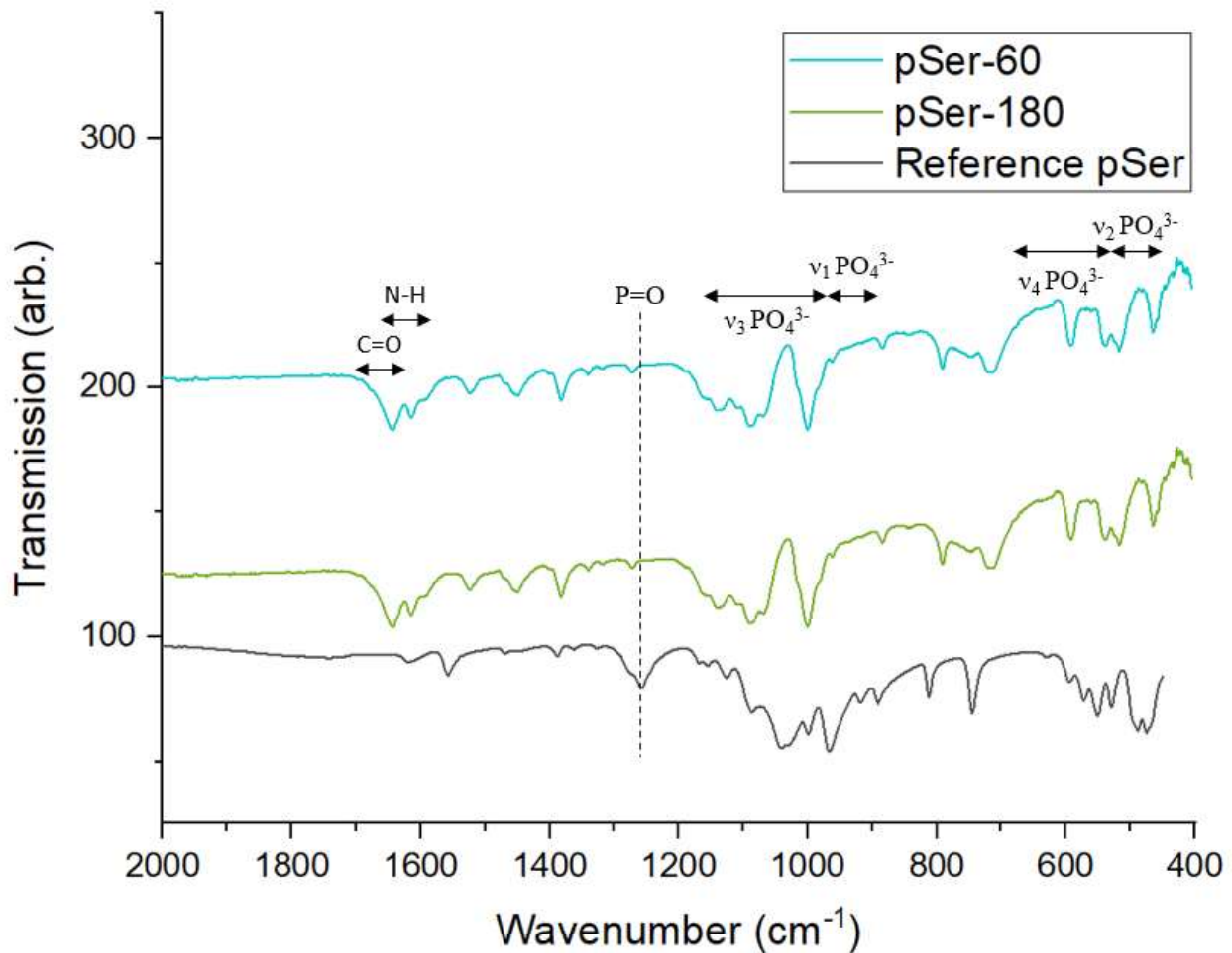


Figure 3-9: FT-IR spectra of inorganic and Ca-pSer coatings

3.3.6 XANES

Lastly, the electronic structure of the coatings was examined using X-ray absorption near-edge structure (XANES). The Ca K-edge XANES is taken from 4020 – 4140 eV. The first spectra measure the inorganic coatings in Figure 3-10, and are compared with reference Ca-Ps. I-60 bare a weaker resemblance to reference HAp, as shown in the edge jump (4044 – 4050 eV), broader post-edge shoulder (4060 eV) and the post-edge peaks (4065-4090 eV). However, I-180 contains several distinct features which correspond to HAp. These features include the pre-edge ($1s \rightarrow 3d$ transition), edge jump ($1s \rightarrow 4s$ transition), the absorption coefficient ($1s \rightarrow 4p$ transition), a spectral feature in the post-edge shoulder which suggests its crystallinity, and post-edge peaks from 4065 eV onwards. The slight difference in absorption is attributed to the lower Ca/P ratio, where a lower concentration of the absorbing atom corresponds to a lower absorption coefficient.¹⁶ While some of these spectral features also correlate to the reference DCPD, there is a noticeable distinction in the post-edge shoulder around 4060 eV.

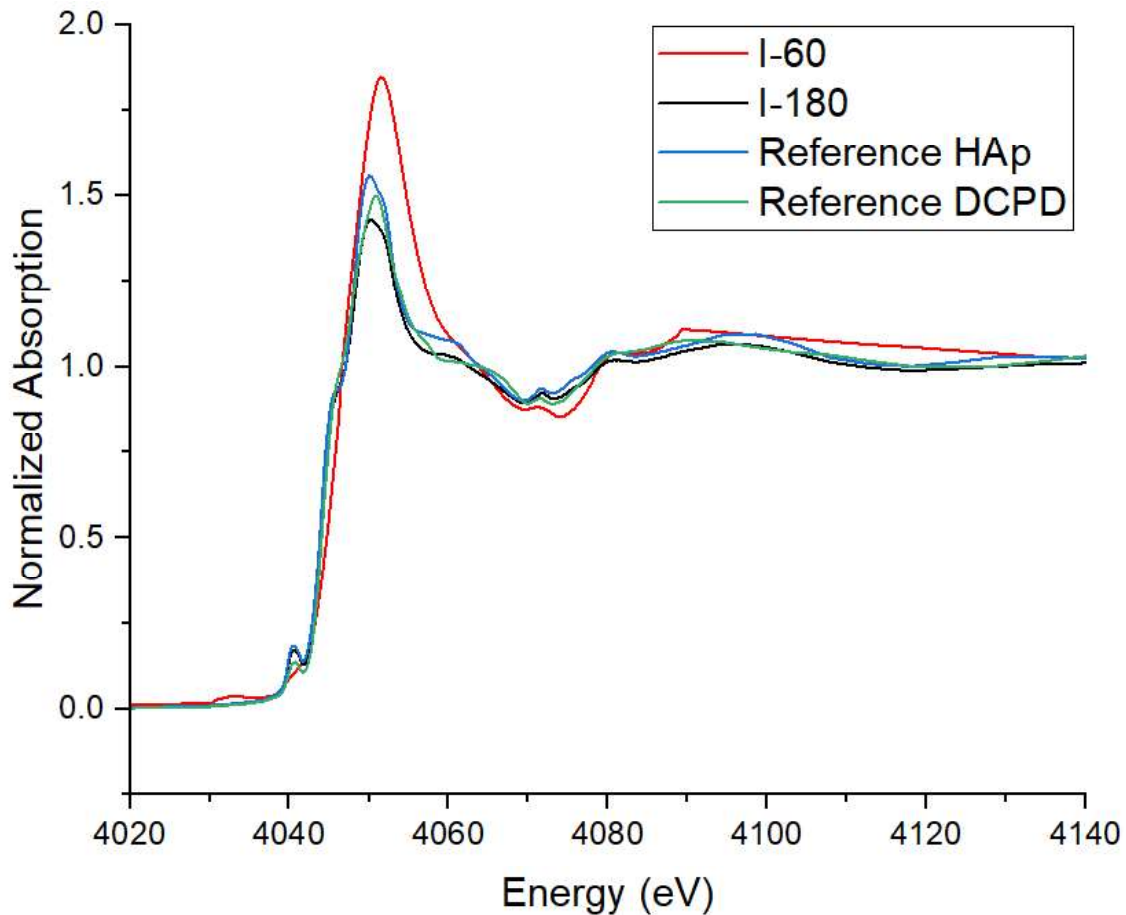


Figure 3-10: Ca K-Edge of inorganic samples in comparison to reference Ca-Ps

Next, the Ca K-edge XANES for the pSer samples were compared to commercially bought ACP in Figure 3-11. At 4030-4042 eV, the distortion at the pre-edge is attributed to the thickness of the sample. The emitted fluorescence x-ray is being re-absorbed by the sample, causing a slight deviation within the pre-edge. Next, there is a slight shoulder at the rising edge at 4046 eV for the reference ACP, and none for the pSer samples. This is likely due to Ca binding to free PO_4^{3-} in the reference ACP, whereas in the pSer samples, the PO_4^{3-} is from an amino acid. Furthermore, there is a difference in the absorption coefficient at 4052 eV as well, which indicates a difference in coordination state of Ca atoms within the samples. Finally, the post-edge shoulders for the pSer-60 and pSer-180 samples, although different from the reference ACP, show that it becomes more amorphous at higher deposition times, when compared to pSer-30. This suggests that at higher deposition times, the chemical environment changes while the crystallinity of the coating decreases.

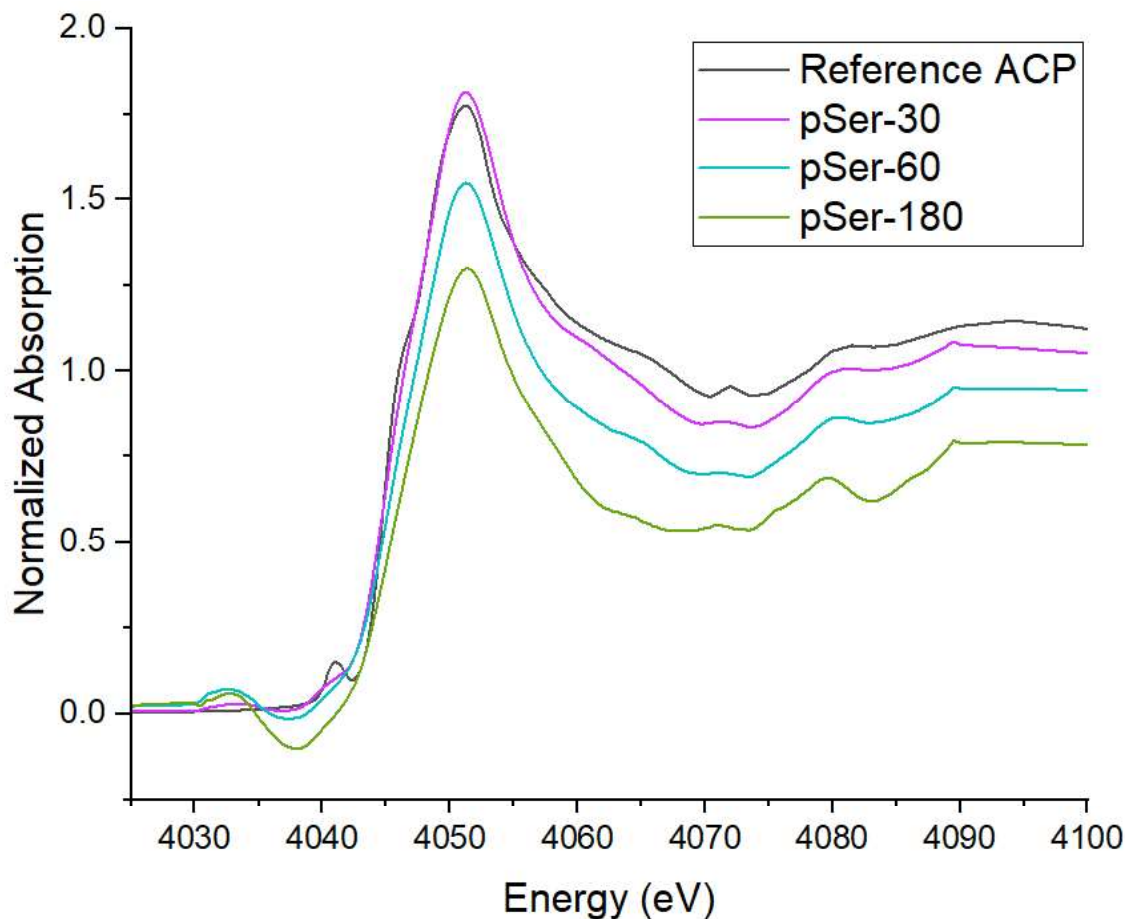


Figure 3-11: Ca K-Edge of pSer samples and ACP reference

The P K-edge XANES peak energies were between 2140 and 2180 eV, as shown in Figure 3-12. The spectra revealed minor variances between the pSer samples at different deposition times. While pSer-30 and pSer-60 contained similar spectral features, pSer-180 shows a slight shift in absorption threshold, which is from an excitation of an electron from a 1s orbital to a 3p transition. Although the P K-edge XANES cannot aid in phase determination, the spectra indicates that the phosphorus in the Ca-pSer coating is neither pSer nor ACP.

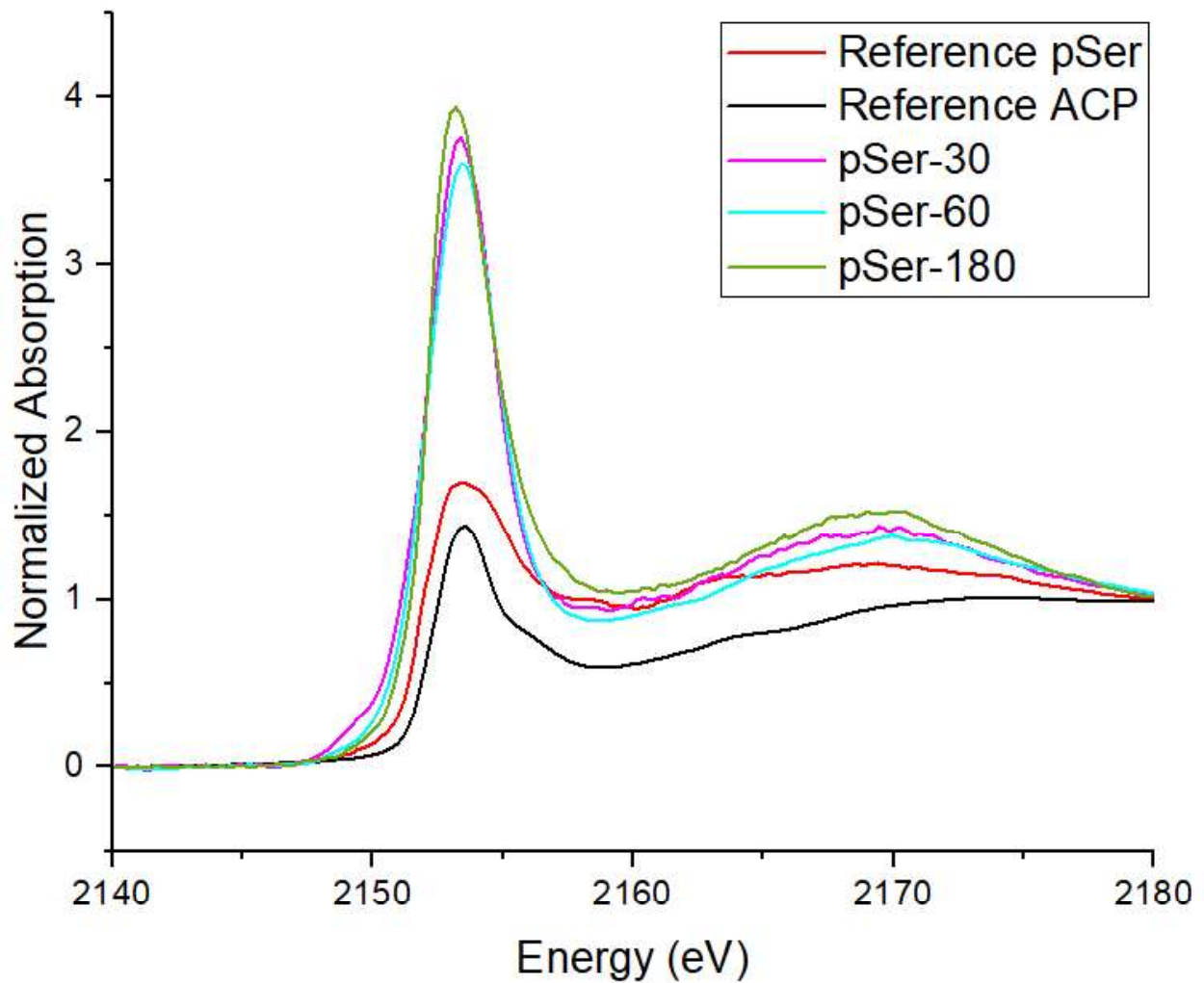


Figure 3-12: *P K-Edge of pSer samples and pSer reference*

3.4 Conclusion

In this chapter, an experimental method was developed for the electrodeposition of Ca-P and Ca-pSer onto a Ti substrate. Using this method, the inorganic and organic coatings synthesized showed moderate growth, coverage, and attachment to the porous film. Therefore, the pre-deposition technique and electrochemical parameters used in this chapter are utilized in future ECD experiments. The mentioned experimental procedure was separated into two sections: anodic oxidation as a pre-deposition technique to fabricate a porous Ti surface and pulsed ECD to synthesize the Ca-P coating onto the Ti substrate. Two different sets of reactants were used to synthesize the Ca-P coating, one involved the use of traditional inorganic phosphorus salt while the other made use of an organic phosphorus source, pSer.

Using the inorganic reagents, a Ca-deficient apatite coating was synthesized, likely due to the lack of OH⁻ production. This is demonstrated through the relatively low Ca-P ratio calculated using EDX analysis and other characterization methods which show HAp or Ca-deficient apatite synthesis. Using pSer as the phosphorus precursor, the flower-like morphology observed in Zhou's study was achieved, but only for the pSer-30 sample. Using higher deposition times, the development of unexpected cuboid structures was observed using SEM. Through the use of XRD, XANES and FT-IR, it is hypothesized that amorphous Ca-pSer was synthesized in the form of cubic structures. The presence of these shapes is unrelated to any previous Ca-P coating synthesis and require further characterization for a thorough determination of the product created.

3.5 References

- [1] Kesseli, F. P.; Lauer, C. S.; Baker, I.; Mirica, K. A.; Van Citters, D. W. *Acta Biomater.* **2020**, *105*, 280–289.
- [2] Low, K. L.; Tan, S. H.; Zein, S. H. S.; Roether, J. A.; Mouriño, V.; Boccaccini, A. R. *J. Biomed. Mater. Res.* **2010**, *94*, 273–286.
- [3] Xu, H. H. K.; Quinn, J. B. *Biomater.* **2002**, *23* (1), 193–202.
- [4] Jeong, J.; Kim, J. H.; Shim, J. H.; Hwang, N. S.; Heo, C. Y. *Biomater Res* **2019**, *23* (1), 4.
- [5] Favarin, B. Z.; Bolean, M.; Ramos, A. P.; Magrini, A.; Rosato, N.; Millán, J. L.; Bottini, M.; Costa-Filho, A. J.; Ciancaglini, P. *Arch. Biochem. Biophys.* **2020**, *691*, 108482.
- [6] Liu, Y.; Liu, S.; Luo, D.; Xue, Z.; Yang, X.; Gu, L.; Zhou, Y.; Wang, T. *Adv. Mater.* **2016**, *28* (39), 8740–8748.
- [7] Zhou, H.; Jiang, Y.-Y.; Tan, S.; Liu, L.-J.; Yao, Q.-T.; Xia, Y.-J.; Fan, Y.-S.; Hu, J.-P.; Zhou, Z.-F.; Lu, B.-Q.; He, S.-S.; Chen, F. *Ceram. Int.* **2020**, *46* (13), 20914–20922.
- [8] Bennick, A.; McLaughlin, A. C.; Grey, A. A.; Madapallimattam, G. *J. Biol. Chem.* **1981**, *256* (10), 4741–4746.
- [9] Drevet, R.; Benhayoune, H. *Coatings* **2022**, *12* (4), 539.
- [10] Benhayoune, H.; Drevet, R.; Fauré, J.; Potiron, S.; Gloriant, T.; Oudadesse, H.; Laurent-Maquin, D. *Adv. Eng. Mater.* **2010**, *12* (6), B192–B199.
- [11] Wang, H.; Guan, S.; Wang, Y.; Liu, H.; Wang, H.; Wang, L.; Ren, C.; Zhu, S.; Chen, K. *Colloids Surf., B.* **2011**, *88* (1), 254–259.
- [12] Drevet, R.; Benhayoune, H.; Wortham, L.; Potiron, S.; Douglade, J.; Laurent-Maquin, D. *Mater. Charact.* **2010**, *61* (8), 786–795.
- [13] Abdel-Aal, E.A.; El-Sayed, D.; Shoeib, M.; Kandil, A.T. *Appl. Surf. Sci.* **2013**, *285*, 136–143.
- [14] Narayanan, R.; Kwon, T.-Y.; Kim, K.-H. *Mater. Chem. Phys.* **2009**, *117* (2–3), 460–464.
- [15] Manoj, M.; Mangalaraj, D.; Ponpandian, N.; Viswanathan, C. *RSC Adv.* **2015**, *5* (60), 48705–48711.
- [16] Liou, S.-C.; Chen, S.-Y.; Lee, H.-Y.; Bow, J.-S. *Biomater.* **2004**, *25* (2), 189–196.

Chapter 4

4 Adenosine Triphosphate as a Phosphorus Source for ACP Coating Synthesis

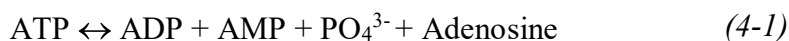
4.1 Introduction

Among the many bioactive calcium phosphate (Ca-P) species, hydroxyapatite (HAp) has been studied and applied the most extensively in biological applications due to its similar chemical composition to natural bone and high thermodynamic stability in physiological environments.¹ These desirable properties allowed for synthetic HAp to be used in a wide spectrum of bioimplant applications including orthopedics and orthodontics.² However, there has been a steady gain of interest in amorphous calcium phosphate (ACP) due to various unique properties that other Ca-Ps do not have.³ ACP has demonstrated better *in vivo* osteoconductivity than HAp and superior biodegradability compared to tricalcium phosphate.⁴ This has permitted ACP to be used in different types of applications within the biomedical field, in recent years.⁵ ACP is formed as an intermediate phase in the crystallization pathway of several Ca-Ps, but it can also be synthesized as the desired end product using the proper starting materials and experimental conditions. In the past, ACP has been successfully formed using various inorganic phosphorus precursors such as diammonium phosphate ((NH₄)₂HPO₄) and orthophosphoric acid (H₃PO₄).^{6,7} In recent studies, however, it was found that synthetic ACP with improved biological properties can be used for the promotion of bone-tendon healing and drug delivery through the use of various organic phosphorus precursors.^{8,9} Additionally, due to its inferior stability, the reactivity of ACP can be exploited to prepare coatings with enhanced adhesion.¹⁰ ACP shows potential as a candidate for implant coatings, inspiring its synthesis using non-traditional Ca-P precursors.

The potential for ACP usage has been studied for several decades, and its advantages over other Ca-Ps have been well documented. However, its instability raises problems for mass production and storage, limiting the development of ACP-based biomaterials. Metastable ACP is a transient phase and can readily convert to crystalline HAp through the process of dissolution, nucleation, and crystal growth when placed in aqueous media without some method of stabilization.^{11,12} One of these methods involves the addition of molecules or ions named stabilizers which are used to prevent the conversion from ACP to HAp. Some additives previously used as stabilizers include

polyethylene glycol, zinc ions, magnesium ions and adenosine triphosphate (ATP).^{13,14,15,16} The particular use of ATP biomolecules for ACP synthesis has drawn attention because it functions as a stabilizer, but can also be hydrolyzed in aqueous solution, producing PO_4^{3-} ions for Ca-P formation (Equation 1).¹⁷ Additionally, the use of ATP as an organic phosphorus source can provide biological advantages compared to traditional inorganic salts.^{2,17,18}

Recently, Liao *et al* have synthesized ACP NPs in an attempt to cure rotator cuff tear, a common problem involving the musculoskeletal system.⁸ They had hypothesized that typical synthetic Ca-Ps may not provide enough bone regeneration to resolve this issue, which inspired the idea behind ACP synthesis using ATP. ATP is rich in adenosine, which can be employed to reduce tissue injury, enhance tissue regeneration and repair through several receptor-mediated mechanisms.¹⁹ Furthermore, adenosine can maintain bone homeostasis and accelerates the rate of bone generation.²⁰ Through ATP hydrolysis in aqueous solution, adenosine is formed as a by-product and can provide dual biological activities of osteogenesis and angiogenesis, providing an excellent biomaterial in the form of NPs. The synthetic ACP was applied in experiments involving cells and rats, displaying promising results both *in vitro* and *in vivo*.⁸



To date, the particular use of ATP as an organic phosphorus source to synthesize and stabilize ACP has only been applied using materials in the micro- and nano-sized scale.^{8,9,18,21,22,23,24,25} Within those studies, there is a heavy focus on the drug-loading capabilities of ACP, due to its high biodegradability and large specific surface area. However, its synthesis and potential as a suitable implant coating remains unknown. In this chapter, ACP is synthesized as a coating using ATP as the phosphorus precursor. Porous Ti is used as the substrate, and the coating is produced using electrochemical deposition (ECD). This chapter focuses on three discussions: 1) composition and morphology of the ACP coatings, 2) the efficiency of stabilization when using ATP to produce ACP, and 3) biocompatibility of the coatings.

4.2 Experimental Methods

4.2.1 Materials

Ammonium fluoride (NH_4F , $\geq 98.0\%$) and calcium chloride dihydrate ($\text{CaCl}_2 \cdot 2\text{H}_2\text{O}$, 74.0-78.0%) were purchased from Alfa Aesar. Adenosine triphosphate disodium salt (Na_2ATP , $\geq 99\%$) and commercially pure Ti foil (cp-Ti $\geq 99.7\%$, 150 mm x 150 mm x 0.127 mm) were bought from Sigma Aldrich. Ethylene glycol and ethanol (EtOH) were obtained from Fisher Chemical.

4.2.2 ACP Electrolyte Synthesis

The electrolyte used for ECD was created by mixing 0.0048 mol Na_2ATP , 0.025 mol $\text{CaCl}_2 \cdot 2\text{H}_2\text{O}$ and 100 mL deionized water. The pH of the solution was raised to 9.7 using 1 M NaOH dropwise, until a cloudy mixture was apparent. The solution was then heated in an oven for 1 hour at 95 °C, where it was then cooled to room temperature prior to deposition use. These samples were named accordingly depending on their deposition time, as shown in Table 4-1.

Table 4-1: *Synthesis parameters used in ATP study*

Deposition Time (min)	Sample Name
0	ATP-0
5	ATP-5
10	ATP-10
15	ATP-15
30	ATP-30
60	ATP-60

4.2.3 MTS Assay

In this study, a 72-hour cytotoxicity assay was conducted to measure the biocompatibility of the ACP coatings. The assay measured the absorbance of a blank, bare porous Ti substrate prior to deposition, I-60 (inorganic Ca-P coating electrodeposited at 60-minute deposition time from Chapter 3) and ATP-30, where the blank control consists of a sample-free culture medium. To increase accuracy within the measurements, three duplicate substrates were made for each set of samples. Prior to cell exposure, all materials were sterilized using ultraviolet irradiation for 2 hours. The cell used in this experiment is an osteoblast precursor, MC3T3, where it was seeded with a density of 0.2×10^6 cells/well in a 96-well plate and left to adhere for 5 hours. The substrates were submerged in the well once the cells were adhered and were cultured for 72 hours. The proliferation rate is measured using CellTiter 96® Aqueous One Solution Cell Proliferation Assay.

After 72-hours incubation, the wells were replaced with 500 μL of fresh media and 100 μL of MTS solution was added into each well and incubated at 37 $^{\circ}\text{C}$ for 2 hours. 75 μL of the culture supernatant was transferred into a new 96-well plate and diluted with 75 μL PBS (1:1 dilution). Finally, the absorbance of the supernatant was measured at 490 nm with a spectrophotometric microplate reader.

4.3 Results and Discussion

4.3.1 SEM-EDX Analysis

Using SEM imaging, the morphology of the coatings was monitored at different deposition times, as shown in Figure 4-1. As observed, there is a positive correlation between the amount of deposited Ca-P and deposition time.

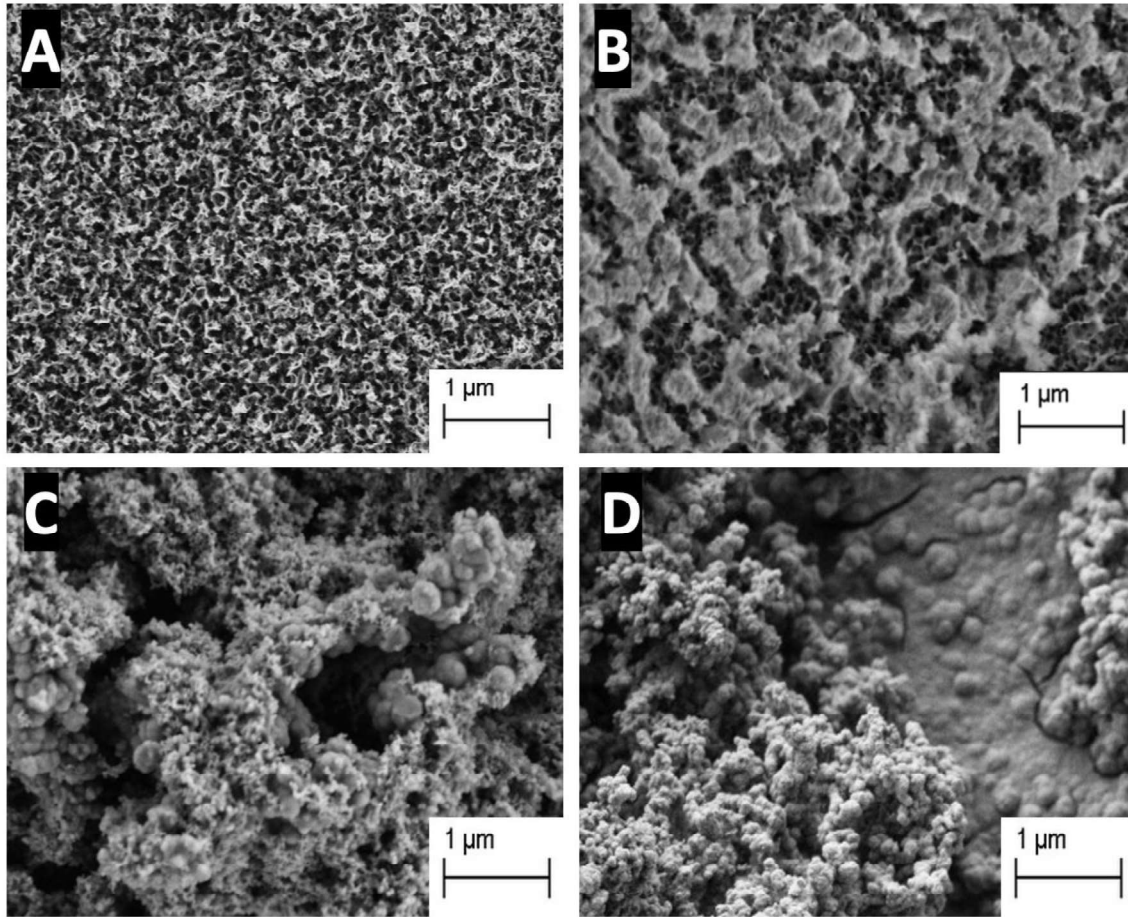


Figure 4-1: SEM imaging of ACP electrodeposited onto porous Ti. (a) 0 min (ATP-0), (b) 15 min (ATP-15), (c) 30 min (ATP-30), and (d) 1 hour (ATP-60) deposition time

Figure 4-1A shows a porous TiO₂ surface prior to the ECD process. At 15-minutes, there is only partial coverage of the coating, and the porous Ti surface can still be observed. The increase in density of the coating directly correlates to the duration of the deposition time. In addition, the deposition time plays a crucial role in the morphological evolution of the Ca-P coating. At 30-minutes, there is the presence of two distinct morphologies within the coating: the larger, packed

spheres and the smaller, dispersed crystals. In ATP-60, there is continual growth of the coating which covers the entire substrate surface. The bottom layer contains a dense coating with embedded spheres, while loosely packed spheres are attached to the surface.

The coating shown at 30-minutes is of great interest because although it has previously been observed, the reason for the variance in morphologies has not been reported.¹⁸ As a result, EDX analysis was also utilized to quantitatively identify the elemental composition of the two morphologies, as shown in Figure 4-2.

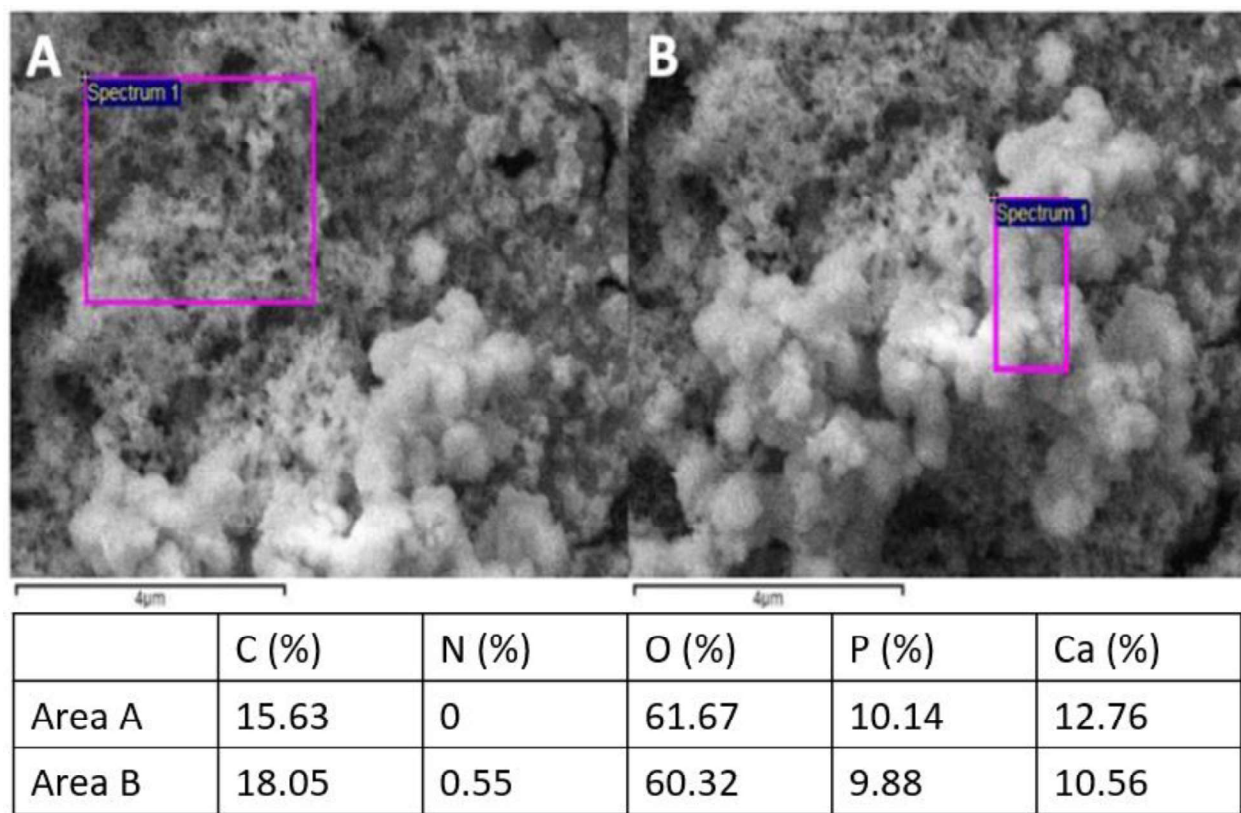


Figure 4-2: EDX analysis of the distinct morphologies in ATP-30

Aside from the expected elements due to atmospheric exposure, there is the presence of Ca and P from both morphologies. In addition to those elements, the packed spheres in Figure 4-2B also contained traces of N, which derived from the adenosine component of ATP. Through a comparative analysis between the two areas of interest with distinct morphologies, small concentrations of nitrogen are detected in the sphere-shaped NPs. Since the only N-containing species involved throughout the coating process is the adenosine component of ATP, it is

confirmed that the residual ATP is present in the coating and only in the “foam-like” region. Conversely, the dispersed crystals are mainly Ca-P.

4.3.2 FT-IR Spectroscopy

FT-IR spectroscopy is used to analyze the chemical species in the ATP-30 sample. As shown in Figure 4-3, the ATP-30 sample exhibits similar features with both the reference ACP and Na₂ATP starting material. Firstly, ATP-30 contains intense peaks at 1092 cm⁻¹ (PO₄³⁻ ν₁ bending) and 541 cm⁻¹ (PO₄³⁻ ν₄ bending), which are both characteristic of ACP. Furthermore, ATP-30 also has several peaks which correspond to ATP molecules. The strong absorption peak at 1645 cm⁻¹ (-C=C- stretching) alongside the peaks at 1477 cm⁻¹, 1422 cm⁻¹, 1209 cm⁻¹, 915 cm⁻¹ and 721 cm⁻¹ (PO₃⁴⁻) are all attributed to the presence of ATP. Finally, the peaks at 2976 cm⁻¹ and 2922 cm⁻¹ originate from the -CH₃ and -CH₂ of ATP, respectively. This suggests the successful formation of an ACP coating, which also contains residual ATP molecules.

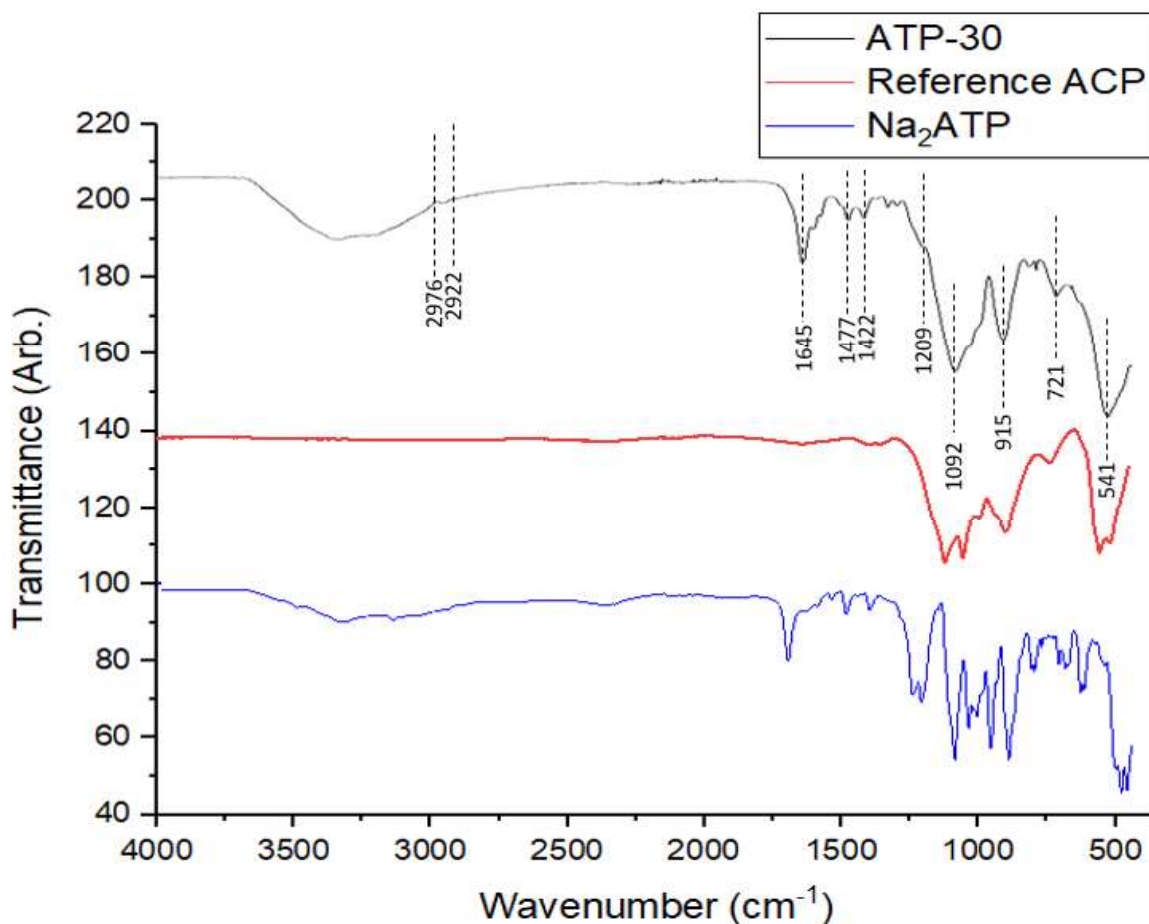


Figure 4-3: FT-IR spectra of ATP-30, Reference ACP and Na₂ATP

4.3.3 Ca and P K-Edge XANES

Next, the Ca and P K-edge XANES were used to comparatively analyze the electronic structure of the coatings synthesized. For the Ca K-edge XANES, the spectra were taken between 4025-4150 eV. Figure 4-4A shows a comparison between the coatings at different deposition times. The pre-edge peak at 4039 eV ($1s \rightarrow 3d$ transition) of the samples has a close resemblance to the commercially bought ACP, although there are some slight differences in the absorption threshold and the post-edge shoulder. First, the difference in intensity for the absorption threshold indicates a deviation in the unoccupied states for Ca p. This change in the unoccupied states of Ca suggests a modification in the surrounding environment of the Ca atom. This is likely due to presence of the ATP biomolecules, which donate charge to the Ca 4p states.⁹ The differences in the post-edge shoulder can be attributed to the difference in crystallinity between the samples. Figure 4-4B shows that despite the aqueous environment of the electrochemical experiment, ATP-30 does not contain the same spectral features as the reference HAp. The lack of strong signals in the post-edge shoulder supports the idea that an amorphous phase had been synthesized, despite the aqueous environment used during ECD.

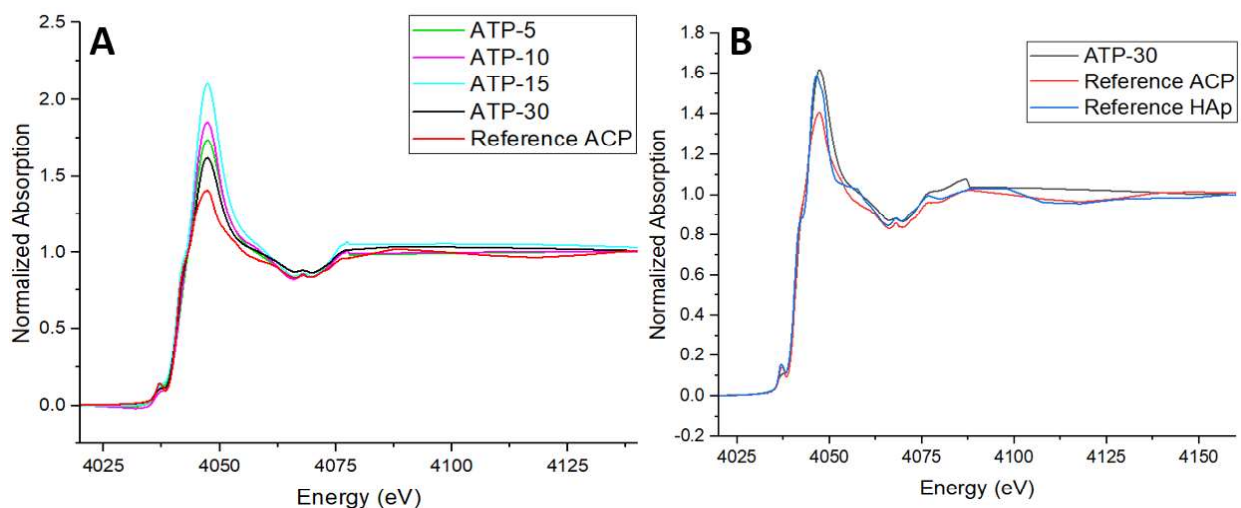


Figure 4-4: Ca K-edge XANES of ACP coatings. (a) comparison of samples at different deposition times, (b) comparison to reference Ca-Ps

Next, the P K-edge XANES was measured, which was taken between 2140 and 2190 eV. Figure 4-5 shows a drastic change in the absorption coefficient (Peak A: $1s \rightarrow 3p$ transition) and post-edge shoulder (Peak B: $1s \rightarrow 3p$ transition with distortion from Td symmetry).²⁷ The slight post-shoulder (labelled as Peak C) is due to additional multiple scattering effects involving distant

neighbouring atoms. Finally, the broad post-edge (Peak D) at 2171 eV is due to the P-O σ^* resonance.⁹ To conclude, ATP-30 contains spectral features that resemble both ACP and Na₂ATP. These findings indicate that the synthesized coating is ACP, which contains ATP biomolecules.

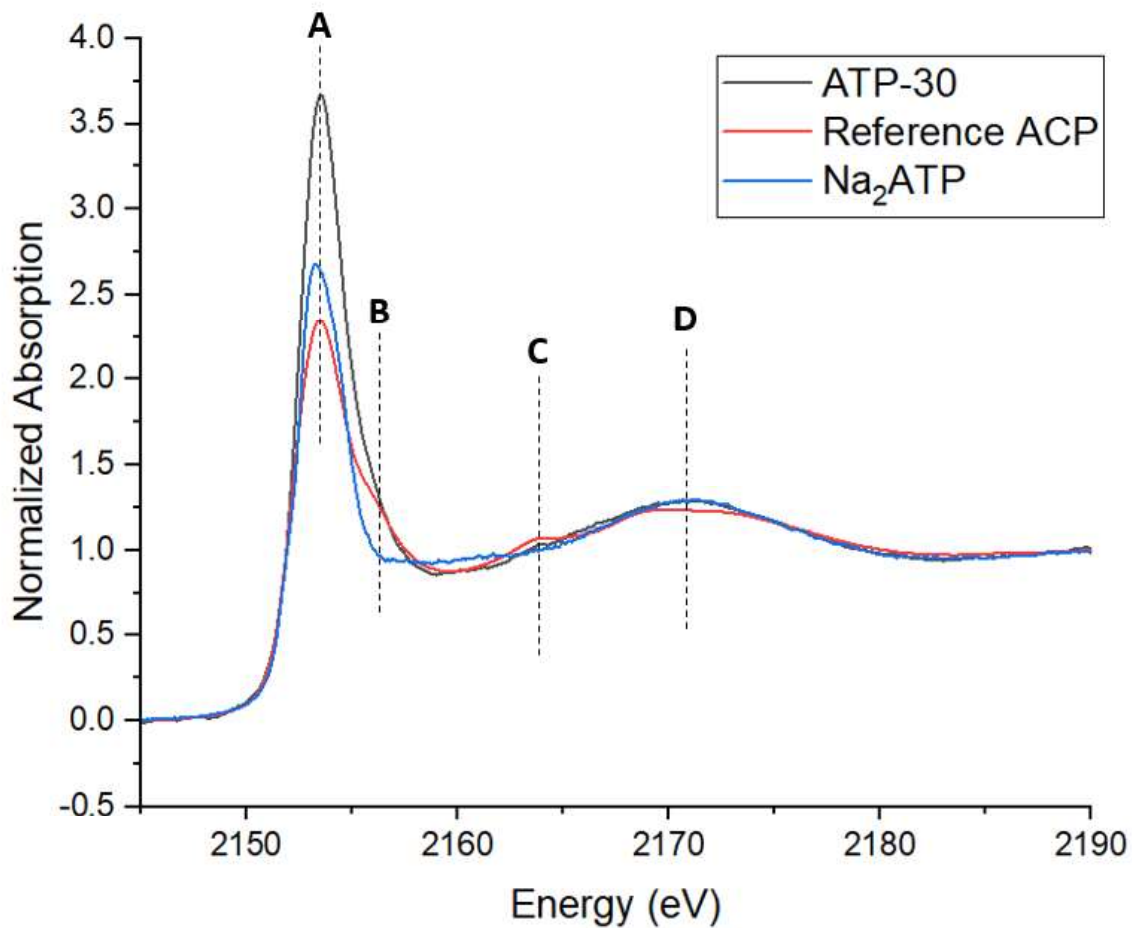


Figure 4-5: The P K-edge XANES of ATP-30, reference ACP and Na₂ATP

4.3.4 Stability Test

In aqueous media (e.g., water), ACP readily converts to HAp without some method of stabilization. As a result, a stability test was designed to investigate whether the presence of ATP within the coating helps to prevent ACP from crystallization. The test was performed by first fabricating duplicate ATP-30 samples using identical experimental conditions. The samples were then submerged in separate water containers for up to 7 days, where they were characterized and comparatively analyzed.

Table 4-3: *Synthesis parameters used in stability test*

Submersion Time in Water	Sample Name
0 days	ATP-30
1 day	Water-1
3 days	Water-3
7 days	Water-7

Theoretically, as the conversion from ACP to HAp takes place, there will be an increase in crystallinity, as well as changes in the chemical and physical states which is characteristic of HAp. In this study, ATP-30 is comparatively studied with the submerged samples. SEM imaging is used to monitor the morphological changes in the coating. XRD is used to measure any change in crystallinity that may occur throughout the submersion time. Lastly, FT-IR spectroscopy is used to detect changes in functional groups between the submerged samples.

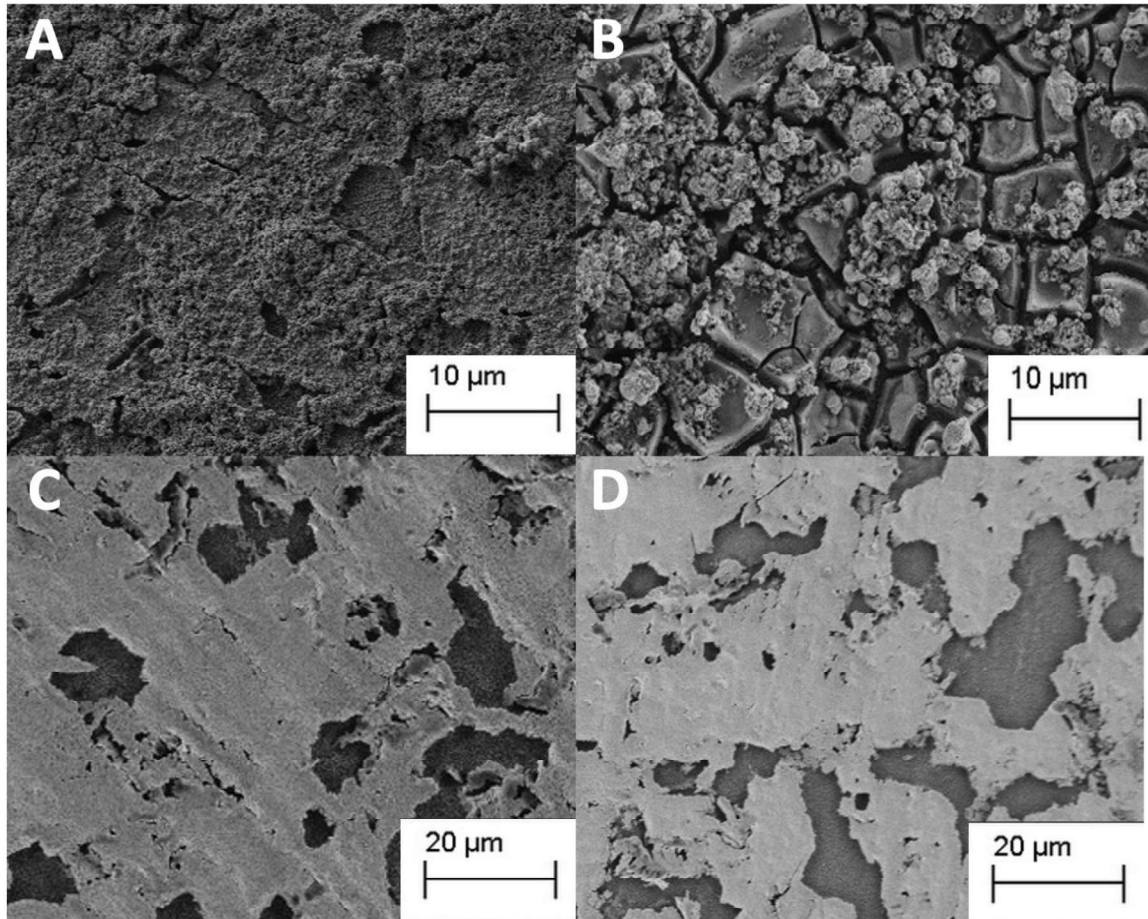


Figure 4-6: SEM images of submerged samples (lower magnification). (a) ATP-30, (b) Water-1, (c) Water-3, (d) Water-7

Figure 4-6 shows SEM images of the submerged samples at low magnification to compare the difference in coating coverage during different submersion periods. Prior to submerging the samples in water, ATP-30 shows high coating coverage onto the porous Ti substrate. However, as the submersion time increases, cracks within the coating becomes apparent and the coating gradually falls off. At higher submersion times, the porous Ti surface can be seen, demonstrating poor attachment between the coating and substrate when submerged in water.

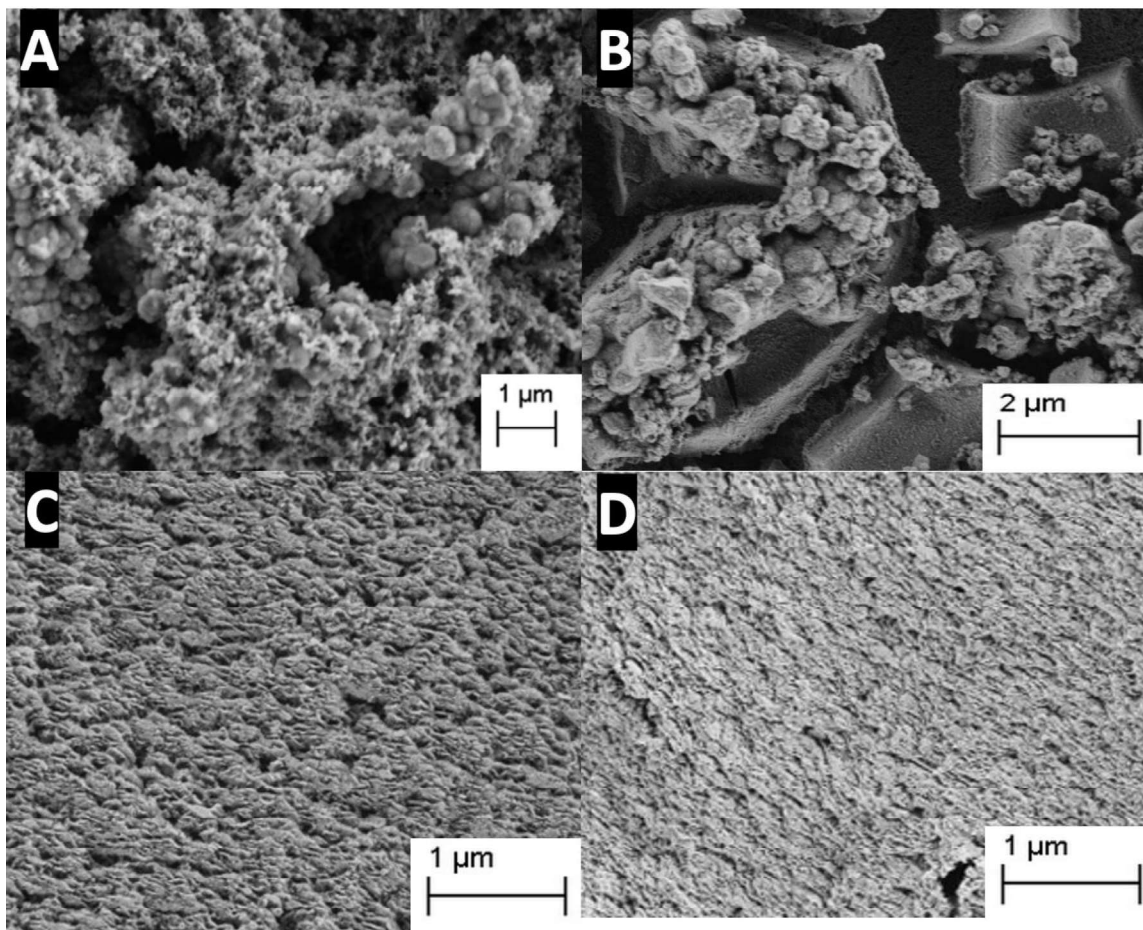


Figure 4-7: SEM images of stability test samples. (a) ATP-30, (b) Water-1, (c) Water-3, (d) Water-7

Next, higher magnification SEM images were taken to track the changes in morphology throughout submersion. In Figures 4-7A and 4-7B, two different morphologies can be observed. Notably, at 1 day submersion time, the presence of the ATP stabilizers is still visible, while the coating begins to form dense chunks. At higher immersion times, the difference in coating morphologies can no longer be observed, as depicted in Figures 4-7C and 4-7D. Despite the high submersion periods in water, the morphology of the coatings does not resemble typical electrodeposited HAp coatings.²⁸ At this point, further characterization is necessary to detect whether the coating remained amorphous.

Next, XRD was used to qualitatively measure the change in crystallinity at different submersion times. Without the addition of ATP as a method of stabilization, ACP would convert to HAp. If ACP had converted to HAp after being immersed in water, there will be an expected increase in

crystallinity detected. ACP is an amorphous species, which will not display any distinct peaks, similar to the porous oxide layer formed on the Ti surface. Figure 4-8 shows a XRD spectrum of the ATP coatings before and after submersion in water. Aside from the Al background signals which is caused by a portion of the x-ray not hitting the substrate surface, the submerged samples closely resemble ATP-30 prior to submersion. Furthermore, they did not display any peaks corresponding to HAp (or any other crystalline Ca-P species).²⁹ As shown in Water-3 and Water-7, there are higher intensity peaks associated with Ti as submersion time increased, due to some of the ACP coating falling off the substrate.

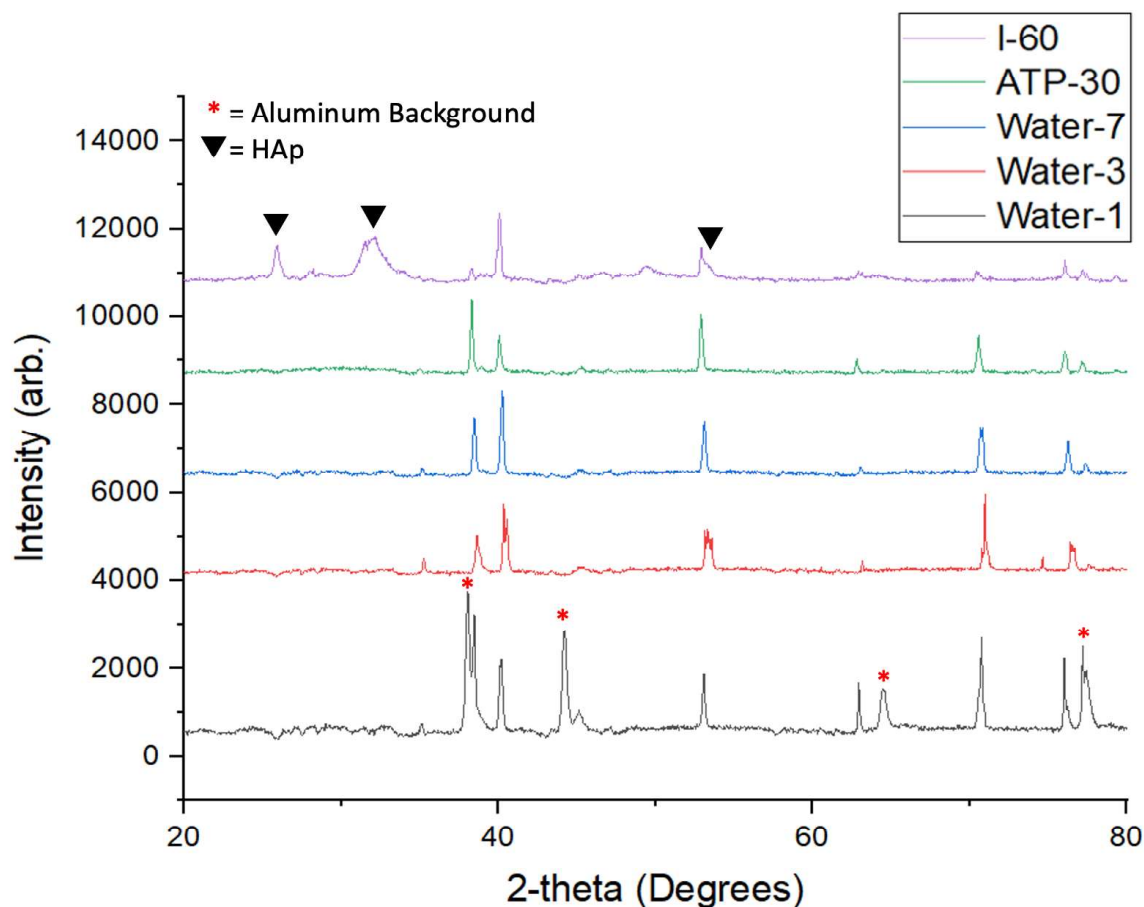


Figure 4-8: XRD spectrum of submerged samples, ATP-30 and I-60

Lastly, the FT-IR spectroscopy was used to compare the functional groups within the ATP-30 sample and the submerged samples. Shown in Figure 4-9, although the intensity of various peaks differs, the wavenumber of the signals was similar. Notably, there is a deviation in the intensity of the -OH peak, which indicates absorbed water. The peaks corresponding to PO_4^{3-} within ACP at

1092 cm^{-1} and 541 cm^{-1} are still present. Similarly, the peaks characteristic of ATP (located at 2976 cm^{-1} , 2922 cm^{-1} , 1477 cm^{-1} , 1422 cm^{-1} , 1209 cm^{-1} , 915 cm^{-1} and 721 cm^{-1}) are also present, although the intensity of some is clearly weaker than before. Despite the similarities in peak signals, there is a clear distinction between some of the submerged samples, indicating a change in various bond vibrations.

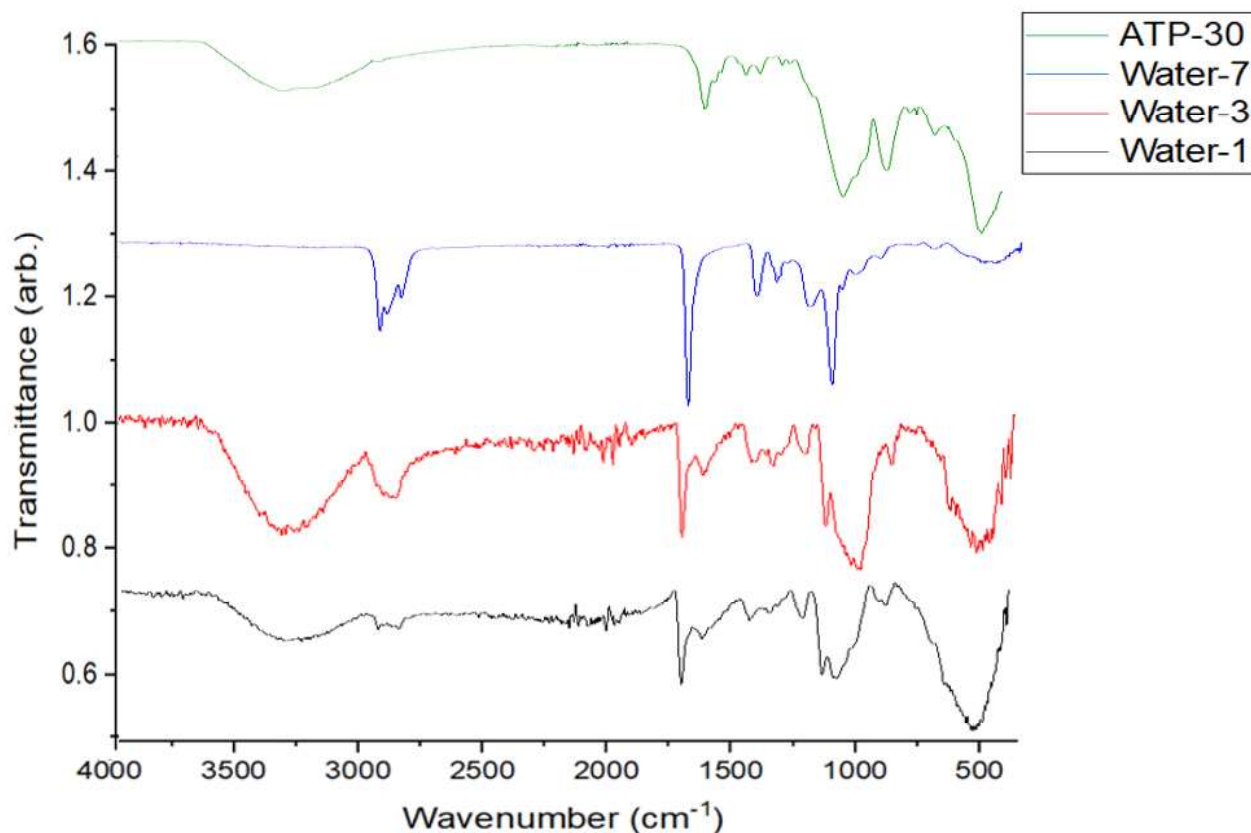


Figure 4-9: FT-IR spectra of submerged samples and ATP-30

With the sole use of FT-IR spectroscopy, it is difficult to discern ACP from HAp, simply due to its close resemblance in peak locations and intensity.²⁹ The lack of crystallinity in the submerged samples shown in XRD suggests that the coating remained amorphous despite the morphological change observed through SEM imaging and the difference in FT-IR spectra. To conclude the findings of the stability test, the submerged coatings remained amorphous and contained ATP, even after 7-day immersion in water. However, the test conducted shows two concerns: 1) the coating gradually falls off with increasing submersion time and 2) the immersion in water induces a change in the Ca-P phase, despite maintaining its amorphous structure.

4.3.5 Biocompatibility Test

To measure the biocompatibility of the coatings, a cytotoxicity assay was performed. Within this test, three sets of samples were exposed to MC3T3 cells for up to 72 hours. The supernatant was collected, and their absorbance of the 490 nm light was measured. The results are summarized in Figure 4-10.

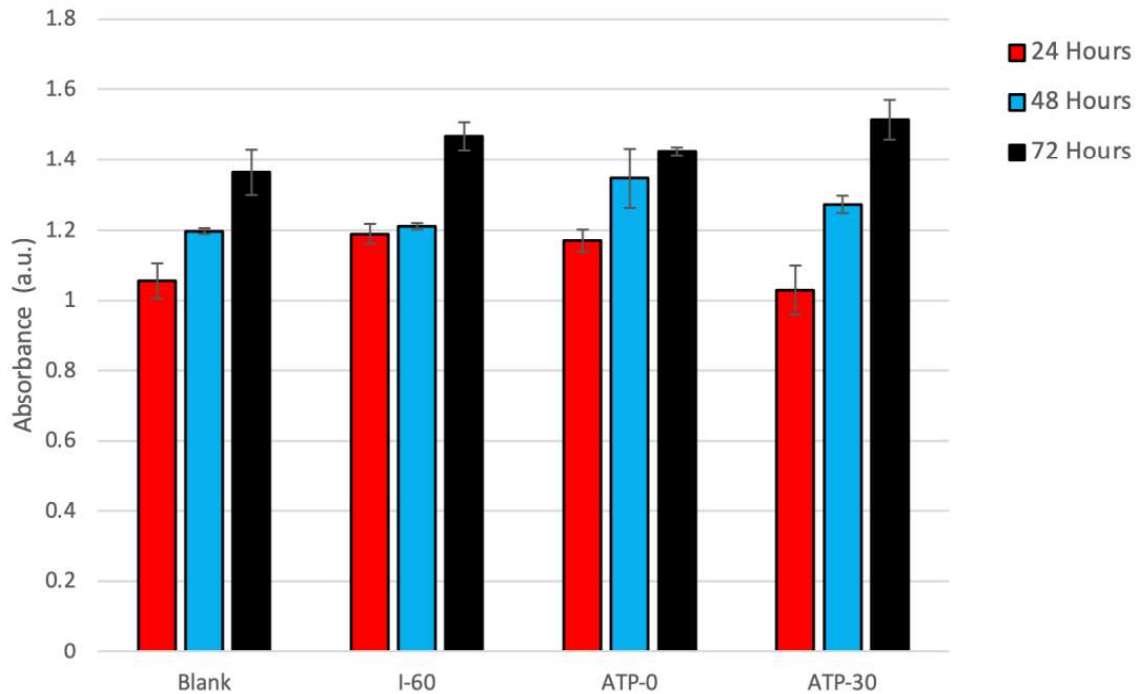


Figure 4-10: Cell activity measured using MTS assay (MC3T3) for blank, I-60, ATP-0 and ATP-30 at different co-culture times

Higher absorbances indicate healthy and normal cell growth, demonstrating cell proliferation. Conversely, lower absorbances mean inhibited growth. At 24 hours, the I-60 and ATP-0 samples showed higher absorbance than the blank, which is consistent with previous literature, as it is known that Ti and crystalline Ca-Ps are biocompatible and applicable as cell culture substrates.³⁰ However, the ATP-30 coating demonstrated inferior cell growth at 24 hours. Similar results can be observed at 48-hours, however, there was a significant increase in absorbance for the ATP-30 sample. Finally, at 72-hours, ATP-30 showed a higher cell count than all other samples. This suggests that the ATP-30 sample has improved cell proliferation and/or cell adhesion over time. This is consistent with previous histological evaluations where ACP synthesized using ATP has

improved cell viability with increasing co-cultured time.¹⁸ The cells adhered on the substrates were then observed using a fluorescent dye, calcein, as shown in Figure 4-11. The cells on all samples were shown to be healthy, elongated and fully intact.

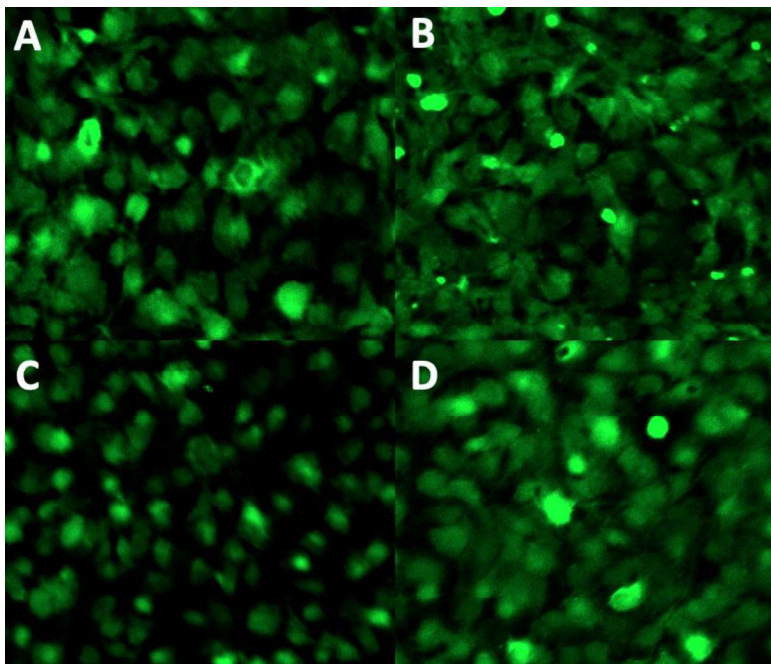


Figure 4-11: *Calcein Images of substrates at 72-hour co-culture time. (a) Blank, (b) I-60, (c) ATP-0, (d) ATP-30*

To conclude the findings of the biocompatibility test, the MTS assay has shown that the ATP-30 sample had lower cell viability at 24-hour co-culture time. However, as the co-culture time increased, a significant increase in absorbance was observed. At 72-hours, there was higher cell activity than not only the blank, but the inorganic Ca-P coating as well. This suggests healthy and high cell proliferation for the sample of interest, ATP-30.

4.4 Conclusion

In this chapter, an ACP coating was synthesized using ATP biomolecules as the starting phosphorus precursor. This was performed through the electrodeposition of ACP onto a porous Ti surface, which showed two different morphologies within the coating: the buds and the nanospheres. EDX analysis revealed the presence of nitrogen, presumably from the adenosine component of ATP within the nanospheres. XRD and K-edge XANES indicated the successful formation of an amorphous species, while FT-IR spectroscopy showed that the coatings contained several distinct features resembling both ACP and ATP. This reinforces the presence of ATP within the coating, alongside ACP.

It was previously hypothesized that the presence of ATP within the ACP composites could inhibit the crystallization of HAp, due to the higher instability of ACP.⁴ Therefore, a stability test was conducted by immersing ATP-30 samples into water for up to 7 days. SEM imaging revealed that within an aqueous environment, the attachment between the coating and substrate is poor, which is shown through the coating gradually falling off. XRD showed that despite a submersion time in water for 7 days, the coating remained amorphous, while FT-IR spectroscopy showed a close resemblance in spectral features between the pre-submerged sample and the submerged samples.

Lastly, a biocompatibility test was conducted to measure the cell viability and cell proliferation of the ATP samples. In this study, the ATP-30 sample was comparatively studied with I-60 synthesized in Chapter 3, a bare porous Ti surface and a control which contained only the osteoblast cells. At 24 hours co-culture time, the ACP coating showed inhibited growth of cells relatively, however, at 72 hours, there was a significant increase in absorbance indicating high cell proliferation. Based on these findings within the biocompatibility test, ATP-30 has shown to be a promising material for bone tissue engineering applications.

4.5 References

- [1] Isa, N. N. C.; Mohd, Y.; Yury, N. *APCBEE Procedia* **2012**, *3*, 46–52.
- [2] Safavi, M. S.; Walsh, F. C.; Surmeneva, M. A.; Surmenev, R. A.; Khalil-Allafi, J. *Coatings* **2021**, *11* (1), 110.
- [3] Zhou, H.; Jiang, Y.-Y.; Tan, S.; Liu, L.-J.; Yao, Q.-T.; Xia, Y.-J.; Fan, Y.-S.; Hu, J.-P.; Zhou, Z.-F.; Lu, B.-Q.; He, S.-S.; Chen, F. *Ceram. Int.* **2020**, *46* (13), 20914–20922.
- [4] Zhao, J.; Liu, Y.; Sun, W.; Zhang, H. *Chem. Cent. J.* **2011**, *5* (1), 40.
- [5] Degli Esposti, L.; Iafisco, M. *Biomater. Biosyst.* **2022**, *5*, 100037.
- [6] Somrani, S.; Banu, M.; Jemal, M.; Rey, C. *J. Solid State Chem.* **2005**, *178* (5), 1337–1348.
- [7] Layrolle, P.; Lebugle A. *Chem. Mater.* **1994**, *6*, 1996-2004.
- [8] Liao, H.; Yu, H.-P.; Song, W.; Zhang, G.; Lu, B.; Zhu, Y.-J.; Yu, W.; He, Y. *J Nanobiotechnol* **2021**, *19* (1), 270.
- [9] Jiang, Y.-Y.; Wang, Z.-Q.; Chen, J.-T.; Li, J.; Zhu, Y.-J.; Liu, L.-J.; Guo, X.-X.; Hu, Y.-F.; He, S.-S.; Wu, J.; Chen, F.; Sham, T.-K. *Phys. Chem. Chem. Phys.* **2020**, *22* (23), 13108–13117.
- [10] Combes, C.; Rey, C. *Acta Biomater.* **2010**, *6* (9), 3362–3378.
- [11] Blumenthal, N. C.; Betts, F.; Posner, A. S. *Calc. Tis Res.* **1977**, *23* (1), 245–250.
- [12] Jin, B.; Liu, Z.; Shao, C.; Chen, J.; Liu, L.; Tang, R.; De Yoreo, J. J. *Cryst. Growth Des.* **2021**, *21* (9), 5126–5134.
- [13] A. L. Boskey.; A. S. Posner, *J. Phys. Chem.* **1973**, *77* (19), 2313 – 2317.
- [14] Y. B. Li.; W. J. Weng, *J. Mater. Sci. Mater. Med.* **2007**, *18*, 2303 – 2308.
- [15] Schweikle, M.; Bjornoy. S. H.; Helvoort, A.; Haugen, H.; Sikorski, P.; Tiainen, H. *Acta Biomater.* **2019**, *90* (132 – 145)
- [16] Shahrezaee, M.; Raz, M.; Shishehbor, S.; Moztarzadeh, F.; Baghbani, F.; Sadeghi, A.; Bajelani, K.; Tondnevis, F. *Silicon* **2018**, *10* (3), 1171–1179.
- [17] Qi, C.; Zhu, Y.-J.; Zhao, X.-Y.; Lu, B.-Q.; Tang, Q.-L.; Zhao, J.; Chen, F. *Chem. Eur. J.* **2013**, *19* (3), 981–987.
- [18] Feng, W.; Feng, C.; Wang, B.; Jing, A.; Li, G.; Xia, X.; Liang, G. *Mater. Today Commun.* **2020**, *25*, 101455.
- [19] Linden, J. *Mol Pharmacol* **2005**, *67* (5), 1385–1387.
- [20] Strazzulla, L.; Cronstein, B. *Purinergic Signal.* **2016**, *12* (4), 583-593

- [21] Ding, G.-J.; Zhu, Y.-J.; Qi, C.; Lu, B.-Q.; Wu, J.; Chen, F. *J. Colloid Interface Sci.* **2015**, *443*, 72–79.
- [22] Ding, G.-J.; Zhu, Y.-J.; Qi, C.; Lu, B.-Q.; Chen, F.; Wu, J. *J. Mater. Chem. B* **2015**, *3* (9), 1823–1830.
- [23] Lu, B.-Q.; Zhu, Y.-J.; Chen, F.; Qi, C.; Zhao, X.-Y.; Zhao, J. *Chem. Asian J.* **2014**, *9* (10), 2908–2914.
- [24] Qi, C.; Zhu, Y.-J.; Zhang, Y.-G.; Jiang, Y.-Y.; Wu, J.; Chen, F. *J. Mater. Chem. B* **2015**, *3* (37), 7347–7354.
- [25] Ding, G.-J.; Zhu, Y.-J.; Qi, C.; Lu, B.-Q.; Wu, J.; Chen, F. *J. Colloid Interface Sci.* **2015**, *443*, 72–79.
- [26] Zhang, Z.; Wu, H. *Chem. Commun.* **2014**, *50* (91), 14179–14182
- [27] Ingall, E. D.; Brandes, J. A.; Diaz, J. M.; de Jonge, M. D.; Paterson, D.; McNulty, I.; Elliott, W. C.; Northrup, P. *J Synchrotron Rad* **2011**, *18* (2), 189–197.
- [28] Lopez-Heredia, M. A.; Weiss, P.; Layrolle, P. *J Mater Sci: Mater Med* **2007**, *18* (2), 381–390.
- [29] Drouet, C. *BioMed Res. Int.* **2013**, *2013*, 1–12.
- [30] Blinova, M. I.; Yudintzeva, N. M.; Nikolaenko, N. S.; Potokin, I. L.; Raykhtsaum, G.; Pitkin, M. R.; Pinaev, G. P. *Cell Tiss. Biol.* **2010**, *4* (6), 572–579.

Chapter 5

5 Zinc-doped Calcium Phosphoserine Coating

5.1 Introduction

Calcium phosphate (Ca-P)-based coatings to synthesize osteoconductive implants have been widely used for orthopedic and dental purposes for several decades.^{1,2} Currently, biomaterial research surrounding implant applications attempts to further promote biological significance while also diminishing any limitations present. One method of achieving this involves the doping of ions which have previously shown improved biological benefits, such as Zn, Sr and Se.^{3,4,5} These improved effects include antibacterial properties, improved corrosion resistance and cancer suppression respectively. However, one of the major concerns surrounding the production of Ca-P coatings is the colonization of bacteria which eventually occurs on the substrate surface.³ Microbial infections, if left untreated, will result in implant loosening and eventually required replacement of the metal implant.⁶ A proposed solution is the implementation of Zn, which may not only provide the bacterial resistance properties, but can also promote the osteoconductivity of the coating.⁷

Zn, an important trace element found in the human body, is considered a crucial mineral in the growth and development of the skeletal system.⁸ In previous studies, Zn has demonstrated its role in bone metabolism through its influence on osteoblast and osteoclast behaviour.^{9,10} As a result, Zn is often introduced to various synthetic Ca-P systems with the expectation that the release of Zn over time may promote the bone-forming capabilities of the biomaterial. Furthermore, since Zn^{2+} is a bivalent ion and has a smaller ionic radius than Ca^{2+} , it can easily replace the Ca within the Ca-P, providing distinctive properties to the Zn-doped Ca-P biomaterial. By incorporating Zn ions into various Ca-P systems, coatings with reduced risk of infection post-surgery can be obtained.⁶

In the past, researchers have traditionally used hydroxyapatite (HAp) as the phase of the Ca-P coating when using Zn as a dopant.^{3,6,11,12} Through this, they have found that Zn-doped HAp coatings increased antibacterial efficiency against common pathogens (*E. coli* and *S. aureus*),

provided superior corrosion resistance and demonstrated enhanced *in vitro* cytocompatibility in comparison to standard HAp coatings.^{6, 13} Zn has also been used as a dopant to synthesize Zn-doped amorphous calcium phosphate (ACP) mesoporous microspheres using adenosine triphosphate (ATP) as a phosphorus precursor. The Zn-doped ACP synthesized by Zhao *et al.* showed good antibacterial activity against *E. coli* and *S. aureus* as well.¹⁴ However, to date, the doping of Zn into a calcium phosphoserine (Ca-pSer) complex has not been performed. In this chapter, different concentrations of Zn are incorporated into the Ca-pSer system. Porous Ti is used as the substrate, and the coating is produced using electrochemical deposition (ECD). This chapter focuses on two discussions: 1) composition and morphology of the Zn-doped Ca-pSer coating and 2) influence of varying Zn concentration within the Ca-pSer complex.

5.2 Experimental Methods

5.2.1 Materials

Ammonium fluoride (NH_4F , $\geq 98.0\%$) was purchased from Alfa Aesar. Commercially pure Ti foil (cp-Ti $> 99.7\%$, 150 mm x 150 mm x 0.127 mm), hydrochloric acid (HCl, 37%), zinc chloride (ZnCl_2) and phosphoserine (pSer) were purchased from Sigma Aldrich. Ethylene glycol ($(\text{CH}_2\text{OH})_2$) and ethanol (EtOH) were obtained from Fisher Chemical.

5.2.2 Zn-doped Ca-pSer Electrolyte Synthesis

The deposition process was first carried out by synthesizing Ca-pSer coatings without Zn, as a standard for comparison. The electrolyte for ECD was first prepared by adding 10 mL of $(\text{CH}_2\text{OH})_2$ into a 40 mL solution containing 0.025 M CaCl_2 and 0.0843 M pSer. Next, dilute NaOH (1 M) was added to adjust the pH of the solution to 5. The mixture was placed in a water bath at 55 °C for 10 minutes, where it is then cooled for deposition use. ECD was then performed for 30 minutes and 3 hours.

To synthesize the Zn-doped Ca-pSer coatings, two other electrolytes were created for the two different concentrations of Zn used. The first electrolyte consisted of 5 mol% Zn and the second used 10 mol% Zn, using ZnCl_2 as the precursor. Finally, the same ECD pre-deposition and ECD configurations were employed to synthesize and deposit the coating. The synthesis parameters used in this chapter are shown in Table 5-1.

Table 5-1: *Synthesis parameters and the notations of the samples investigated in this study*

Sample Type	Reactants Used	Deposition Time	Sample Name
Ca-pSer	CaCl_2 and pSer	30 minutes	pSer-30
		3 hours	pSer-180
Zn-doped Ca-pSer (5 mol% Zn)	CaCl_2 , pSer and ZnCl_2	30 minutes	5Zn-30
		3 hours	5Zn-180
Zn-Doped Ca-pSer (10 mol% Zn)	CaCl_2 , pSer and ZnCl_2	30 minutes	10Zn-30
		3 hours	10Zn-180

5.3 Results and Discussion

5.3.1 SEM-EDX Analysis

Through the use of SEM imaging, the morphologies of the coatings were observed at different deposition times. Figure 5-1 A-C shows the coatings at 30-minute deposition time, for the varying concentrations of Zn at a lower magnification. Overall, the coatings all exhibited moderate coverage of the Ti surface, despite the lower deposition time.

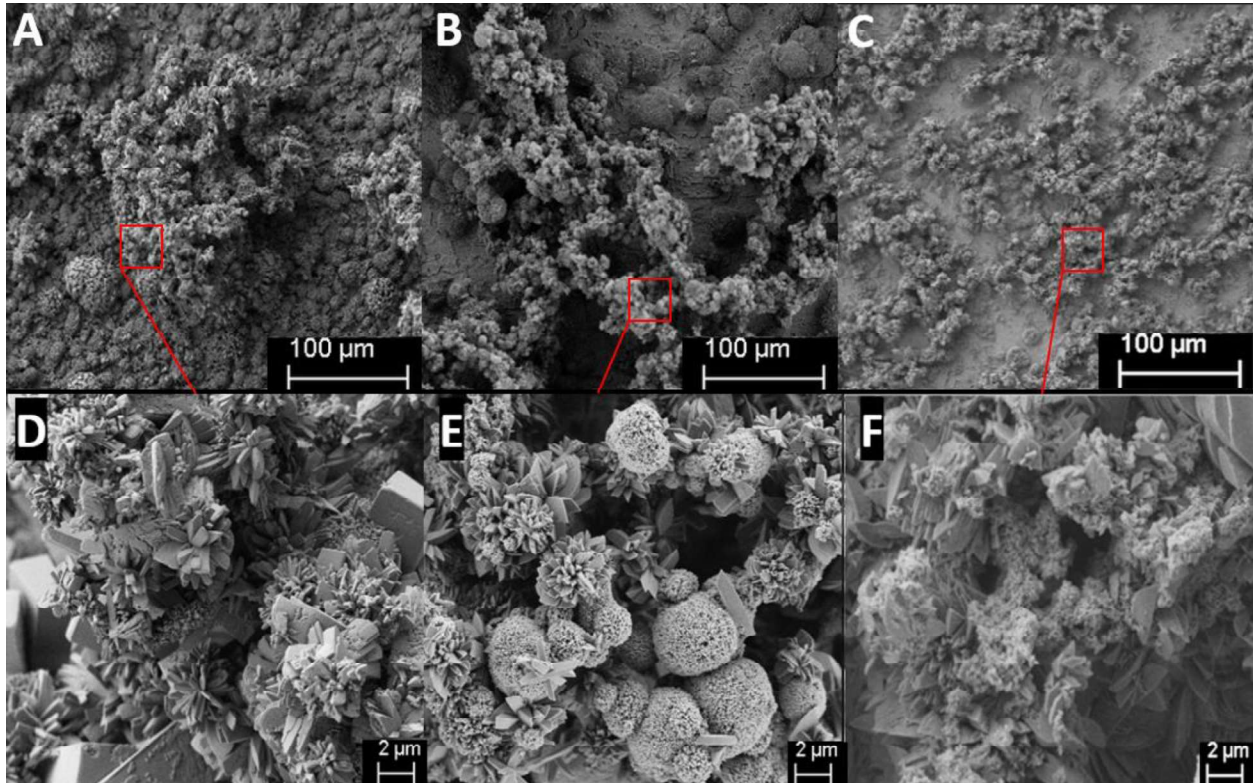


Figure 5-1: SEM imaging of coatings formed at 30-minute deposition time. Lower magnification: (a) pSer-30, (b) 5Zn-30 (c) 10Zn-30, higher magnification: (d) pSer-30, (e) 5Zn-30 (f) 10Zn-30

To observe the difference in morphology influenced by Zn concentration, higher magnification images were taken, as shown in Figure 5-1 D-F. Without the inclusion of Zn, there is the appearance of a flower-like Ca-pSer complex, as observed in Zhou's study.¹⁵ However, there was also the presence of cubic structures, which do not correlate to past studies involving Ca-pSer synthesis. In Chapter 3, it was hypothesized that these cubic structures have an amorphous nature. However, with the inclusion of 5 mol% Zn, the cubic structures cannot be seen. Instead, the

formation of porous microspheres was observed. Furthermore, as shown in Figure 5-1E, the presence of the flower-like Ca-pSer can still be observed. With the use of 10 mol% Zn, the flower-like morphology and cubic structures cannot be observed. Instead, the presence of scattered micro-plate structures form, alongside microporous non-spherical shapes.

At 3-hour deposition time, there are different morphologies observed for all three samples, as observed in Figure 5-2. For pSer-180, the flower-like morphologies shown in Figure 5-2A cannot be observed at all. Instead, there is an abundant number of cubic structures throughout the synthesized coating. In 5Zn-180, the flower-like morphology is no longer observable and instead, it looks similar to the morphology observed in Figure 5-2C. However, the formation of microspheres were still observable. Finally, with the use of 10 mol% Zn, no spheres are found. Instead, dense shards with refined edges can be seen, with smaller pieces sticking to the surface.

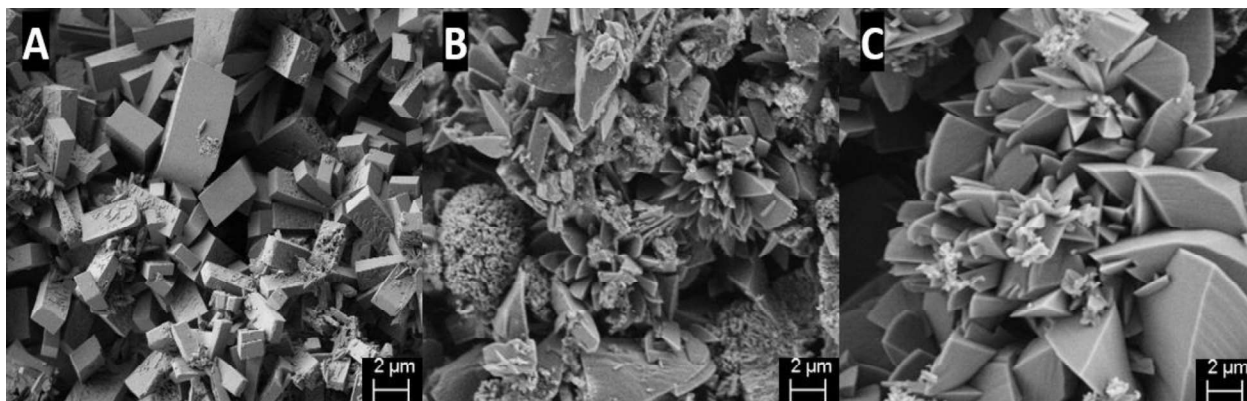


Figure 5-2: SEM imaging of coatings formed at 3 hours deposition time. (a) pSer-180, (b) 5Zn-180 (c) 10Zn-180

Next, EDX analysis was performed to evaluate the elemental composition of the coatings. In Table 5-2, the Ca, P and Zn concentrations are shown for the different samples and varying morphologies. This is also illustrated in Figure 5-3, which clearly shows the elemental composition for each morphology.

Table 5-2: Elemental composition (atomic %) of the pSer and Zn-doped pSer samples

Sample	Morphology	Ca (%)	P (%)	Zn (%)
pSer-30	Flower	6.22	6.39	0
	Cuboid	7.68	7.25	0
5Zn-30	Flower	6.37	7.87	0
	Sphere	0.24	5.66	7.72
10Zn-30	Chunks	7.13	10.16	2.76
pSer-180	Cuboid	5.67	6.25	0
5Zn-180	Plate	6.15	6.55	0.24
	Sphere	0.27	6.68	8.46
10Zn-180	Shards	4.66	7.26	1.11

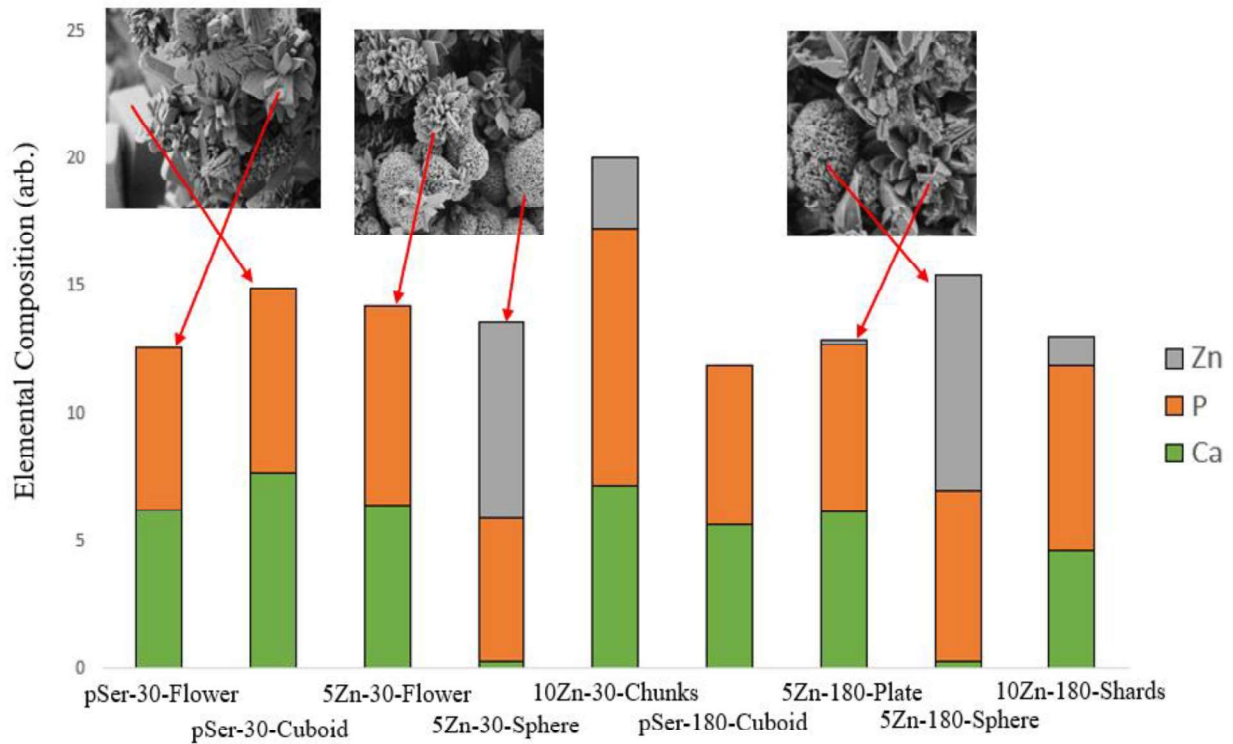


Figure 5-3: Elemental Composition of Coating Morphologies

EDX analysis has shown that the flower-like morphology and cuboids found in pSer-30 and pSer-180 contained similar concentrations of Ca and P. However, when 5% mol Zn is added,

microspheres begin to form. These spheres contain high concentrations of Zn and P, and very low concentrations of Ca, suggesting the formation of a zinc phosphate species.¹⁷ The flower and plate-like morphologies found within those samples mainly contain Ca and P, with little to no Zn detected. This indicates that with the inclusion of 5 % mol Zn, Zn-containing spheres are formed as opposed to replacing Ca²⁺ within the Ca-pSer complex. Using higher concentrations of Zn, spheres can no longer be observed, as shown in 10Zn-30 and 10Zn-180. Within the plates and shards, a mixture of Ca, P and Zn is detected. Furthermore, the concentration of Ca (relative to P) is lower when Zn is introduced. This suggests that using 10 mol% Zn, Ca is substituted by the Zn within the Ca-pSer complex, instead of fabricating any of the microspheres shown in 5Zn-30 and 5Zn-180.

5.3.2 X-ray Diffraction

The crystallinity of the samples was evaluated using XRD, as shown in Figure 5-4. Firstly, the pSer samples without Zn show high crystallinity at 30 minutes. The several peaks located from 12-29 degrees correspond to Ca-pSer and are similar to the complex synthesized by Kesseli *et al.*¹⁸ However, at the higher deposition time of 3 hours, the coating becomes amorphous over time. This is demonstrated through the lack of peaks, except for the Ti peaks at 38, 41, 53 and 71 degrees.¹⁹ With the inclusion of 5 and 10 mol% Zn, the position of peaks obtained at 30-minute deposition time were similar. However, at 3-hour deposition time, deviations in the spectrum can be observed for the differing concentrations of Zn. Using 5 mol% Zn, the coating becomes amorphous, like that of pSer-180. In contrast, the usage of 10 mol% Zn maintains the crystallinity of the sample. In a previous study, Esfahani had reported that the inclusion of 6 or higher mol% Zn increased the crystallinity of HAp.¹⁶ Although the doping of Zn into Ca-pSer has not been studied before, the XRD spectrum demonstrate that the use of 10 mol% kept the crystalline nature of the coating. Furthermore, when comparing 10Zn-30 to pSer-30, the intensity of the peaks is significantly higher in 10Zn-30, whereas the peaks associated with 5Zn-30 had similar intensity in comparison to pSer-30. This was also demonstrated in the SEM image (Figure 5-2C), where the morphology of the shards resembles the crystalline flower-like Ca-pSer more than the amorphous cubic structures formed in Figure 5-2A.

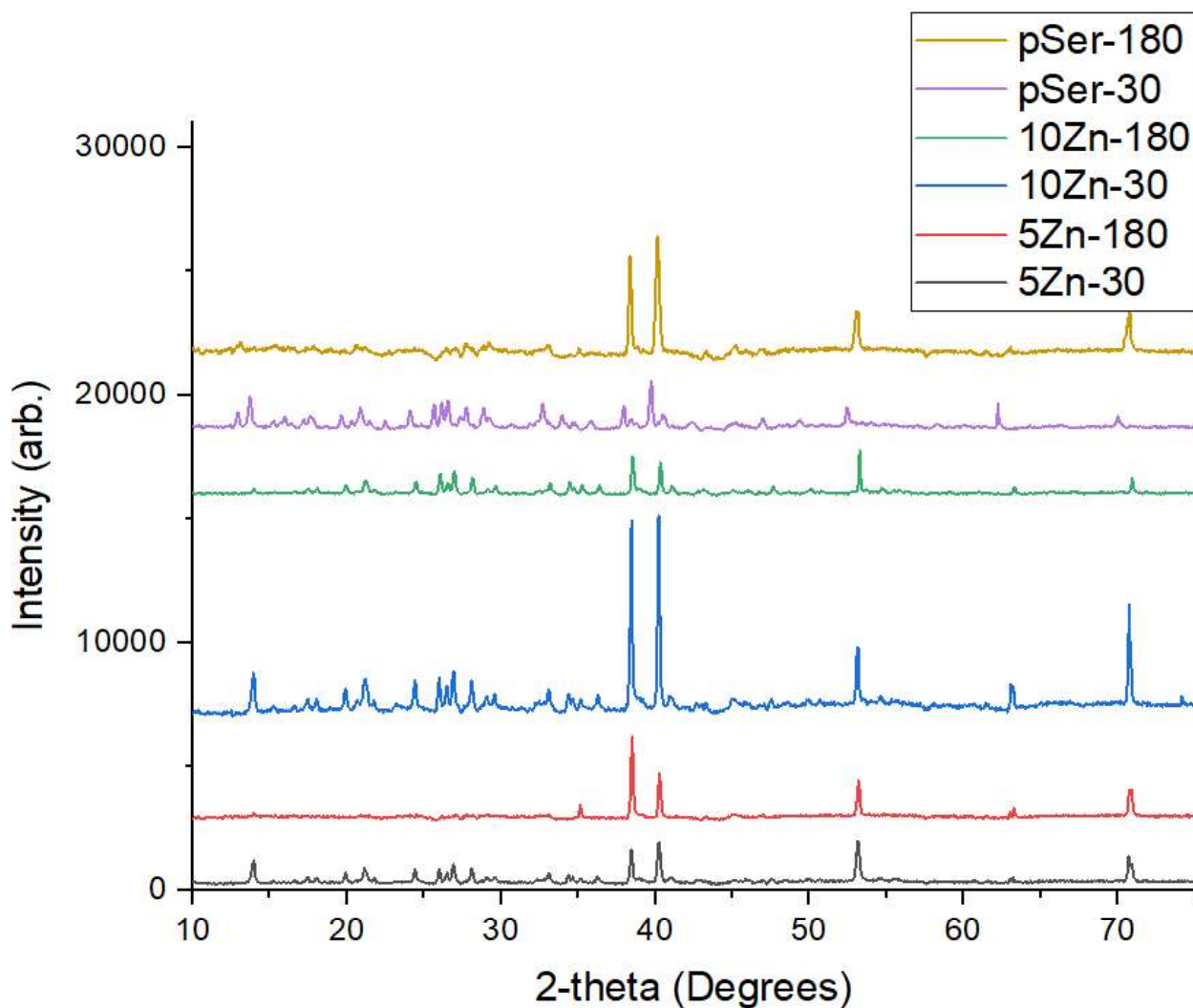


Figure 5-4: XRD spectrum of pSer and Zn-doped pSer samples

3.3.3 FT-IR Spectroscopy

FT-IR spectroscopy was employed next to detect the functional groups within the coatings, as shown in Figure 5-5. Through a quick qualitative comparison, each of the Zn-doped Ca-pSer samples contained similar peaks, with the exception of 5Zn-180, where a series of Zn-OH and Zn-O peaks can be found from 400 to 950 cm^{-1} .²⁰ Aside from the broad peak shown in 5Zn-180, all samples exhibited the following peaks: C=O stretching (1638 cm^{-1}), N-H bending (1609 cm^{-1}), $\nu_3\text{PO}_4$ (993-1139 cm^{-1}), and $\nu_1\text{PO}_4$ (839-880 cm^{-1}). However, several peaks cannot be observed in 5Zn-180 ($\nu_4\text{PO}_4$ (706-785 cm^{-1}) and $\nu_4\text{PO}_4$ (459-585 cm^{-1})) due to the broad peak.

Overall, 10Zn-30 and 10Zn-180 resemble the pSer samples more than 5Zn-30 and 5Zn-180. This is demonstrated through several features. First, the peak at 1268 cm^{-1} attributed to P=O stretching from pSer is lessened with the inclusion of 5 mol% Zn. Next, the several peaks ascribed to PO_4^{3-} are also lessened in 5 mol% Zn, relative to the other samples. This is likely due to the formation of $\text{Zn}_3(\text{PO}_4)_2$ microspheres which have a different peak intensity than Ca-pSer and Zn-doped Ca-pSer.

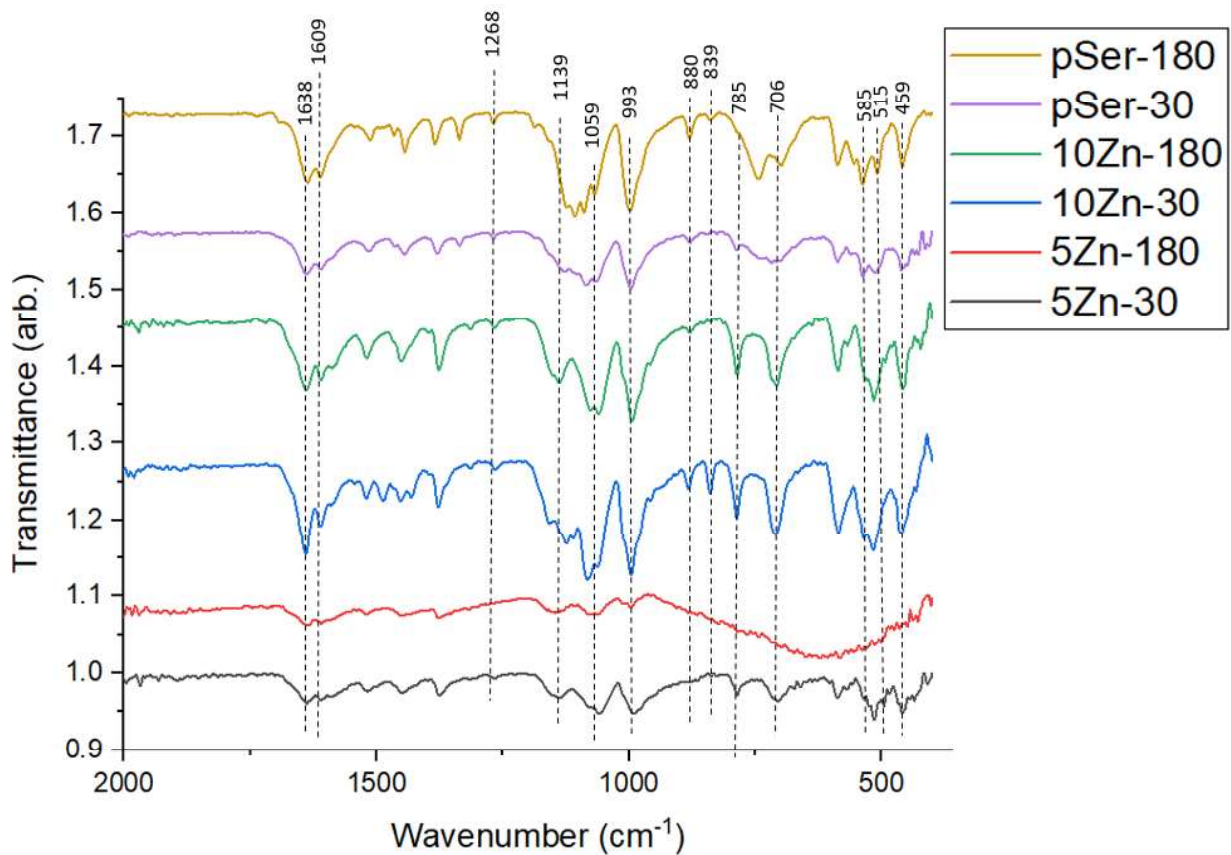


Figure 5-5: FT-IR spectra of Zn-doped Ca-pSer samples

5.4 Conclusion

In this chapter, Zn-doped Ca-pSer coatings were synthesized and deposited onto a porous Ti substrate using ECD. These samples were then compared to Ca-pSer coatings, which did not contain any Zn. SEM was used to track the morphology of the coatings over time, which revealed different morphologies depending on the differing concentrations of Zn and deposition time. Without Zn, the pSer samples contained flower-like structures and eventually cuboids for 30-minute and 3-hour deposition times, respectively. By introducing 5 mol% Zn, microspheres were formed alongside the flower and plate-like morphologies. The inclusion of 10 mol% Zn inhibited the growth of the cubic structures. EDX analysis was used to measure the elemental composition of the different shapes: the flower, plate and shard-like morphologies contained mainly Ca and P, while the spheres primarily contained Zn and P. The SEM-EDX analysis has also shown that using 5 mol% Zn does not replace Ca in the Ca-pSer complex, and instead forms spheres. However, at 10 mol% Zn, Ca gets replaced by Zn, which is shown by the lowered concentration of Ca (relative to P) and detection of Zn. XRD revealed that 10 mol% Zn increased the crystallinity of the coating at 30-minute deposition time and maintained the crystallinity of the 3-hour sample. Lastly, FT-IR spectroscopy revealed very similar functional groups present for both concentrations of Zn used. This suggests that the doping of Zn does not influence FT-IR of the sample, with the exception of the broad peak shown in 5Zn-180. The large peak is likely attributed to Zn-O and Zn-OH, ranging from 400 to 950 cm^{-1} . Formation of the flower-like and cuboid morphologies is inhibited in 5Zn-180, which may suggest some Zn replacing Ca in the Ca-pSer complex. It is hypothesized that for the inclusion of 5 mol% Zn, $\text{Zn}_3(\text{PO}_4)_2$ microspheres are formed which has different peak intensities compared to Ca-pSer and 10 mol% Zn-doped Ca-pSer.

5.5 References

- [1] Su, Y.; Zheng, Y.; Tang, L.; Qin, Y.-X.; Zhu, D. *Orthop. Biomater.*; Springer International Publishing: Cham, 2017; pp 167–183.
- [2] Al-Sanabani, J. S.; Madfa, A. A.; Al-Sanabani, F. A. *Int. J. Biomater.* **2013**, *2013*, 1–12.
- [3] Huang, Y.; Zhang, X.; Mao, H.; Li, T.; Zhao, R.; Yan, Y.; Pang, X. *RSC Adv.* **2015**, *5* (22), 17076–17086.
- [4] Huang, C. H.; Yoshimura, M. *Sci Rep* **2020**, *10* (1), 10602.
- [5] Yilmaz, B.; Evis, Z.; Tezcaner, A.; Banerjee, S. *Int. J. Appl. Ceram. Technol.* **2016**, *13* (6), 1059–1068.
- [6] Uysal, I.; Yilmaz, B.; Evis, Z. *J Aust Ceram Soc* **2021**, *57* (3), 869–897.
- [7] O'Connor, J. P.; Kanjilal, D.; Teitelbaum, M.; Lin, S. S.; Cottrell, J. A. *Materials* **2020**, *13* (10), 2211.
- [8] Luo, X.; Barbieri, D.; Davison, N.; Yan, Y.; de Bruijn, J. D.; Yuan, H. *Acta Biomater.* **2014**, *10* (1), 477–485.
- [9] Yamaguchi, M.; Weitzmann, M. N. *Mol Cell Biochem* **2011**, *355* (1–2), 179–186.
- [10] Li, X.; Senda, K.; Ito, A.; Sogo, Y.; Yamazaki, A. *Biomed. Mater.* **2008**, *3*, 045002.
- [11] Predoi, D.; Iconaru, S.; Predoi, M.; Buton, N.; Motelica-Heino, M. *Coatings* **2019**, *9* (3), 156.
- [12] Candidato, R. T.; Thouzellier, C.; Pawłowski, L. *J. Biomed. Mater. Res.* **2018**, *106* (6), 2101–2108.
- [13] Ding, Q.; Zhang, X.; Huang, Y.; Yan, Y.; Pang, X. *J Mater Sci* **2015**, *50* (1), 189–202.
- [14] Zhao, J.; Zhu, Y.-J.; Zheng, J.-Q.; Chen, F.; Wu, J. *Microporous Mesoporous Mater.* **2013**, *180*, 79–85.
- [15] Zhou, H.; Jiang, Y.-Y.; Tan, S.; Liu, L.-J.; Yao, Q.-T.; Xia, Y.-J.; Fan, Y.-S.; Hu, J.-P.; Zhou, Z.-F.; Lu, B.-Q.; He, S.-S.; Chen, F. *Ceram. Int.* **2020**, *46* (13), 20914–20922.
- [16] Esfahani, H.; Salahi, E.; Tayebifard, A.; Rahimpour, M.R.; Keyanpour-Rad, M. *Rev. Mater.* **2016**, *11726*, 569-676.
- [17] Ning, Z.; Li, W.; Sun, C.; Che, P.; Chang, Z. *Trans. Nonferrous Met. Sco. China* **2013**, *23* (3), 718–724.

[18] Kesseli, F. P.; Lauer, C. S.; Baker, I.; Mirica, K. A.; Van Citters, D. W. *Acta Biomater.* **2020**, *105*, 280–289.

[19] Jiang, X.; Zhang, Wenjie; Yan, L.; Li, J.; Xu, L.; Wei, B.; Zhang, X.; Liu; Li, Zihui; Ye, D. *IJN* **2012**, 4459.

[20] Balogun, S. W.; James, O. O.; Sanusi, Y. K.; Olayinka, O. H. *SN Appl. Sci.* **2020**, *2* (3), 504.

Chapter 6

6 Summary and Future Work

6.1 Summary

In this thesis, the use of electrochemical deposition (ECD) to deposit calcium phosphate (Ca-P)-based coatings was performed, and the coatings were characterized using a variety of analytical techniques. To create a suitable implant substrate, a Ti film underwent anodic oxidation to create a porous TiO₂ layer. Next, different electrolytes were synthesized. Chapter 3 made use of two different electrolyte systems: Ca(NO₃)₂ · 4H₂O and NH₄H₂PO₄ for the inorganic coating, and CaCl₂ and phosphoserine (pSer) for the organic coating. The electrolyte in Chapter 4 was composed of CaCl₂ · 2H₂O and Na₂ATP to synthesize an ACP coating. Lastly, Chapter 5 utilized an electrolyte which consisted of CaCl₂, pSer and small concentrations of ZnCl₂. These electrolytes were then used in a pulsed ECD experiment to deposit the coating onto the substrate. The characterization methods used to characterize the coatings include scanning electron microscopy (SEM) imaging for morphology, energy dispersive x-ray (EDX) analysis to determine the elemental composition, X-ray diffraction (XRD) to detect the crystal structure, Fourier transform – infrared (FT-IR) spectroscopy to measure the presence of functional groups and X-ray absorption near edge structure (XANES) to probe the electronic structure of the coatings.

In Chapter 1, several background topics were introduced. The current state of biomaterial research concerning Ti usage, types of Ca-Ps and the advantages associated with synthesizing certain Ca-P phases were explained. To conclude the chapter, details regarding synchrotron radiation and x-ray absorption spectroscopy were discussed as well.

In Chapter 2, the pre-deposition treatment and deposition conditions to create the Ca-P coatings was explained in detail. The mentioned protocol was applied to each substrate fabricated throughout this thesis. Next, the synchrotron facilities and beamlines used in this thesis were introduced. Finally, other characterization methods were explained, which included SEM, EDX, XRD and FT-IR spectroscopy.

In Chapter 3, a calcium phosphoserine (Ca-pSer) complex coating was synthesized and compared to an inorganic coating synthesized using traditional Ca and P precursors. Due to the parameters used within the ECD experiment, a Ca-deficient apatite coating was synthesized as opposed to hydroxyapatite (HAp). This was due to a lack of OH⁻ production (lack of H₂O₂ or current density), for the pulsed ECD experiment. However, this limitation was limited to the synthesis of HAp, so the same parameters were carried out for the remainder of the thesis. The Ca-pSer coatings were successfully synthesized and yielded similar results to previous literature at low deposition time.¹ However, at higher deposition times of 60 minutes or higher, the coating becomes amorphous over time, with its morphology in the form of cuboids. It is suspected that an amorphous Ca-pSer coating had been synthesized, due to the lack of peaks within the XRD. Furthermore, the Ca and P K-edge XANES of the Ca-pSer coatings do not correlate to reference Ca-Ps, indicating that it is not amorphous calcium phosphate.

In Chapter 4, adenosine triphosphate (ATP) was used to create an ACP coating. The use of ATP provided two functions: the hydrolysis of ATP provides PO₄³⁻ for ACP synthesis, and the presence of residual ATP stabilizes the ACP phase. The ACP coatings were successfully synthesized, and elemental analysis confirmed the presence of nitrogen, presumably from ATP. The coatings then underwent a stability test and biocompatibility test. Without some method of stabilization, metastable ACP readily converts into HAp. Therefore, the samples were submerged in water for up to 7 days to test the efficiency of stabilization provided by ATP. The coatings seemed to remain amorphous, however, the coating gradually detaches from the Ti substrate at higher submersion time. In the biocompatibility test, the ACP coating initially showed low cell growth (relative to blank), when exposed to an osteoblast precursor, MC3T3. However, at higher co-culture time, the ACP coatings had the higher absorbance of the supernatant, indicating high cell proliferation and cell adhesion. Finally, the calcein images further indicate that the cells on the substrate are healthy and elongated.

In chapter 5, Zn was introduced to the Ca-pSer system at 5 and 10 mol% and compared to Ca-pSer without Zn. Without the use of Zn, flower-like Ca-pSer and cuboid morphologies were observed at 30 and 3-hour deposition times respectively. However, with the inclusion of 5 mol% Zn, microspheres, microstructures, and plates were formed. EDX and FT-IR revealed that the spheres

are likely to be $Zn_3(PO_4)_2$ microspheres. With the inclusion of 10 mol% Zn, Zn inhibited the growth of the cubic structures. It is hypothesized that the inhibition is due to Zn replacing Ca, due to similar chemical properties such as charge and ionic radii. Lastly, XRD revealed that the inclusion of 10 mol% Zn increased the crystallinity of the coating, while 5 mol% Zn did not affect the crystallinity of the coating.

6.2 Future Work

In Chapter 3, the use of higher current density or the inclusion of more H_2O_2 when synthesizing the inorganic coating would be beneficial for a HAp coating. For the pSer samples, synchrotron-related analysis may aid in the determination of the synthesized coating. It is hypothesized that the self-assembled flower-like shapes are a result of the calcium pSer complex growing in different directions, through linkages between pSer molecules and Ca^{2+} ions. Specifically, the Ca^{2+} ions form bonds with oxygen in 3 different environments: the carboxylic and phosphate groups from pSer, and water.¹ The use of O K-edge XANES can confirm the connectivity between Ca and O, while Ca K-Edge extended x-ray absorption fine structure (EXAFS) can estimate the bonding distances between the two atoms. This could be performed at the 20A1 beamline at Taiwan Light Source and Soft X-Ray Microcharacterization Beamline (SXRMB), respectively. Theoretically, three different bond lengths should be obtained, which would suggest the formation of amorphous calcium pSer coating. Finally, its osteogenetic potential relative to calcium pSer crystals could also be evaluated and compared.

Future work regarding Chapter 4 involves further synchrotron analysis, specifically the Ca and P K-edge XANES of the submerged samples, which could be done at the SXRMB at CLS. This could help reveal any changes in the ACP buds or ATP stabilizers respectively, throughout the submersion period. Furthermore, EDX analysis has shown that there is poor attachment between the coating and substrate when submerged in water. A method of improving attachment at the coating-substrate interface could be highly promising for future biological applications. Lastly, a 96-hour (or higher) MTS assay could be conducted to measure the cell proliferation potential for the ACP coatings.

Lastly, the future work in Chapter 5 also includes further synchrotron characterization. The Zn and Ca K-edge XANES of the coatings would reveal whether Zn is replacing Ca in the Ca-pSer complex. The use of 5 mol% and 10 mol% Zn showed different results in terms of morphology, and the electronic structure of these samples should differ as well. The Zn K-edge can be performed at the BioXAS at the Advanced Photon Source, while the Ca K-edge can be performed at the SXRMB at CLS. Finally, an antibacterial efficiency evaluation could also be performed, as Zn is a known antimicrobial agent.

6.3 References

- [1] Zhou, H.; Jiang, Y.-Y.; Tan, S.; Liu, L.-J.; Yao, Q.-T.; Xia, Y.-J.; Fan, Y.-S.; Hu, J.-P.; Zhou, Z.-F.; Lu, B.-Q.; He, S.-S.; Chen, F. *Ceram. Int.* **2020**, *46* (13), 20914–20922.

Curriculum Vitae

Name: Clement Lee

Post-secondary Education and Degrees: Western University, London, Ontario, Canada
2016-2020 B.Sc.

Western University, London, Ontario, Canada
2022 – Present M.Sc Student

Honours and Awards: Dean's Honour's List
2020

Centre for Advanced Materials and Biomaterials
Research Oral Presentation, Awarded: \$250
2021

CLS Graduate Student Travel Award
2021

Related Work Experience Teaching Assistant
Chem 1301A: Discovering Chemical Structure
Chem 2213A: Organic Chemistry for Life Sciences
Chem 3372G: Instrumental Analytical Chemistry
Western University
2020-2022